Multidimensional Vibrational Dynamics of Hydrogen Bonded Systems

INAUGURAL - DISSERTATION

zur Erlangung des Doktorgrades
der Freien Universität Berlin
Fachbereich Biologie, Chemie, Pharmazie

vorgelegt von
Yonggang Yang
aus Hubei, China

2008

Diese Arbeit wurde in der Zeit von Juli 2005 bis Juni 2008 unter der Betreuung durch Herrn Priv.-Doz. Dr. Oliver Kühn am Fachbereich Chemie, Biologie, Pharmazie der Freien Universität Berlin in der Arbeitsgruppe von Herrn Prof. Dr. Jörn Manz durchgeführt.

Erstgutachter:	Prof. Dr. Oliver Kühn
Zweitgutachter:	Prof. Dr. Jörn Manz
Tag der Disputation:	15.12.2008

Abstract

This work focuses on vibrational dynamics of hydrogen bonded complexes. The first task for a molecular reaction dynamics simulation is to generate the molecular Hamiltonian in terms of suitable coordinates. To minimize the numerical simulation efforts, the best choice is to adopt the natural motions of the molecule as coordinates, namely, the bond lengths and angles. The method for generating this kind of Hamiltonian has been introduced as a starting point for further numerical applications. In particular we have developed a concise theory to establish the kinetic energy operator in terms of arbitrary coordinates for this purpose.

Concerning applications we first perform a reduced dimensional simulation for the protonated ammonia dimer $[H_3N\cdots H\cdots NH_3]^+$. The $N_2H_7^+$ cation is a strongly hydrogen-bonded low-barrier system with symmetrical structure caused by zero-point vibration of the central proton. The fundamental transition for the shared proton stretching mode by our calculation is significantly red shifted compared with the harmonic prediction due to the strong hydrogen bond. The combinations between the shared proton stretching and the terminal NH_3–NH_3 stretching are found to contribute significantly to the vibrational bands below 1100 cm^{-1}. The larger clusters $NH_4^+(NH_3)_n$ ($n = 2-4$) are investigated with harmonic approximation which gives reasonable results indicating that the hydrogen bonds are much weaker than that of $N_2H_7^+$. Consequently each larger cluster has the solvated ammonium structure and no vibrational bands caused by hydrogen bond stretching dynamics below 1100 cm^{-1}.

A full dimensional simulation is performed for the mono-hydrated hydroxide anion $[HO\cdots H\cdots OH]^-$. This is the same type of strong hydrogen bonded system as the $N_2H_7^+$ with the hydrogen located in the center. In detail the energetic and geometric isotope effects are investigated. Among the isotopomers, the hydrogen bond is energetically more stable than the deuterium bond by about 80 cm^{-1} irrespective of the deuteration status of the free terminal OH groups. In general the conclusion that a hydrogen bond is more stable than a deuteron bond is valid for many hydrogen bonds but the bond energy difference may differ. Concerning the secondary geometric isotope effects, for each isotopomer, the $O\cdots O$ distance decreases upon deuteration due to the fact that the deuteron distribution is more localized than the proton distribution.

Apart from gas phase studies, our investigations also cover condensed phase hydrogen bonds. A general theory for generating reaction surface Hamiltonian and the numerical implementation for reaction rate constant calculations are developed. With this method we have generated a reaction path Hamiltonian based on 6-Aminofulvene-1-aldimine and performed some preliminary calculations for the rate constant of hydrogen/deuterium transfer reaction. The temperature dependence of the reaction rate constant shows Arrhenius rate behavior at high temperature region. The deuterium transfer needs higher activation energy and has lower rate due to its heavier mass. When decreasing the temperature the coherent tunneling effects begin to contribute more and more to the hydrogen/deuterium transfer reaction which flattens the temperature dependence.

Zusammenfassung

Diese Arbeit behandelt die Schwingungsdynamik von Komplexen, die Wasserstoffbrückenbindungen erhalten. Zur Beschreibung molekularer Reaktionsdynamik muss zunächst ein Hamilton-Operator in geeigneten Koordinaten entwickelt werden. Um den Rechenaufwand zu minimieren, empfehlen sich die natürlichen Bewegungen des Moleküls als Koordinaten, d.h. Bindungslängen und -winkel. Das Problem ist hierbei die Bestimmung des Operators der kinetischen Energie. Zur Lösung wurde in dieser Arbeit ein kompakter und intuitiver Zugang entwickelt, um den Operator der kinetischen Energie in Abhängigkeit von beliebigen Koordinaten aufzustellen. Dieser Operator geht dann zusammen mit den berechneten Potentialenergieflächen in die numerischen Simulation ein.

Die erste Anwendung konzentriert sich auf das protonierte Ammoniakdimer $[H_3N\cdots H\cdots NH_3]^+$, das in reduzierter Dimensionalität behandelt wurde. Das $N_2H_7^+$-Ion ist ein System mit niedriger Barriere und starker Wasserstoffbrückenbindung. Das Kation hat symmetrische Struktur, die durch die Nullpunkt-Schwingungen des zentralen Protons verursacht wird. Verglichen mit der harmonischen Näherung, zeigt die von uns berechnete Frequenzfür die asymmetrische Streckschwingung des zentralen Protones wegen der starken Wasserstoffbrückenbindung eine dramatische Rotverschiebung. Die Kombinationsübergänge zwischen der Protonschwingung und der Stretckschwingung der terminalen NH_3–NH_3 Gruppen leisten einen weiteren Beitrag zu den Schwingungsbanden unterhalb von 1100 cm^{-1}. Zur Untersuchung der größeren Cluster $NH_4^+(NH_3)_n$ ($n = 2-4$) kann auf die harmonische Näherung zurückgegriffen werden, da die Wasserstoffbindungen hier viel schwächer ausgeprägt sind. Diese Cluster ähneln in ihrer Struktur mehr einem solvatisierten Ammoniumion und es gibt keine Protonstreckschwingungsbanden unterhalb von 1000 cm^{-1} .

Eine weitere Anwendung betrifft das monohydrierte Hydroxidion, $[HO\cdots H\cdots OH]^-$, das in voller Dimensionalität behandelt wurde. Auch hier gibt es eine starke Wasserstoffbindungen, bei der das Wasserstoffatom symmetrisch zwischen den Sauerstoffatomen positioniert ist. Für dieses System wurden die energetischen und geometrischen Isotopeffekte ausführlich untersucht. Die Bindungsenergie für den Fall des Wasserstoffs liegt immer 80 cm^{-1} höher als für das Deuterium, unabhängig davon, ob die terminalen OH-Gruppen deuteriert sind oder nicht. Das Resultat, dass die Wasserstoffbrücke stabiler als die Deuteriumbrücke ist, hat allgemeineren Charakter für starke Wasserstoffbrückenbindungen dieser Art. Im Bezug auf den sekundären geometrischen Isotopeeffekt nimmt der $[O\cdots O]$-Abstand bei Deuterierung für jedes Isotopmer ab. Die Ursache dafür kann damit erklärt werden, dass die quantenmechanische Deuteron-Verteilung lokalisierter ist als die des Protons.

Neben diesem Gasphasenuntersuchungen wurde auch die Wasserstoffbrückendynamik in der kondensierten Phase untersucht. Eine allgemeine Theorie basierend auf einem Reaktionsfächen-Hamitonian und eine neue Methode für die numerische Implementation von Wegintegral-Rechnungen zu den Reaktionsraten wurde entwickelt und auf den Protontrans-

fer im 6-Aminofulvene-1-aldimine angewandt. Die Temperaturabhängigkeit der Reaktionsrate zeigt Arrhenius-Verhalten im Hochtemperatur-Bereich, wobei die Aktivierungsenergie für den Deuterium-Transfer größer ist und aufgrund der unterschiedlichen Massen auch ein kinetischer Isotopieeffekt beobachtet wird. Mit abnehmender Temperatur werden die Signaturen von quantenmechanischem Tunneln gefunden.

List of Abbreviations and Notations

1D, 2D ...	one dimensional ..., 19
DOF	degree of freedom, 21
DVR	discrete variable representation, 27
GIE	geometric isotope effect, 9
HB	hydrogen bond, 1
HCMO	Hermitian conjugate of momentum operator, 14
IR	infrared, 1
IRMPD	infrared multiple-photon dissociation, 5
IRVPD	infrared vibrational predissociation, 5
KEO	kinetic energy operator, 12
KIE	kinetic isotope effects, 9
LRF	laboratory reference frame, 20
MCTDH	multi configuration time dependent Hartree, 6
MRF	molecular reference frame, 20
PES	potential energy surface, 6
SPF	single particle function, 27
ZPE	zero point energy, 32
†	Hermitian conjugate, 13
$()^{\circ}$	termination of derivative operators, 15
^{T}	transpose, 77

Contents

Chapter 1

Motivation and Introduction

1.1 Why Hydrogen Bonds

Hydrogen bonding and transfer are of fundamental importance for tremendously diverse processes ranging from biomolecular functions, enzymatic reactions to simple acid–base reactions. The scope of hydrogen bond research is really cross-disciplinary involving physics, chemistry, and biology [1-8]. The first publication on the hydrogen bond as a new type of weak bond goes back to 1920 [9, 10] and ten years later the name hydrogen bond (HB) was first introduced by Pauling [11, 12].

In the 1930s the signatures of the formation of HBs in stationary infrared (IR) absorption spectra had been realized [13] and IR spectroscopy continued to be a standard tool to unravel vibrational bands of HBs especially in biomolecules or condensed phases. On the other hand, very recent progress in IR spectroscopy of isolated protonated clusters has provided unprecedented insight into the properties of prototypical HBs [16, 17]. In contrast to condensed phase measurements, these spectra usually appear to be less entangled and therefore should be amenable to theoretical simulations. However, situations involving strong HBs turned out to provide serious challenges for the theory even in gas phase.

Apart from the frequency domain point of view of HB dynamics, which can be obtained from stationary IR spectra, we may further want to understand some fundamental questions like “What does a proton/hydroxide look like and how does it translocation in solution [18, 19, 20]?” This became possible with the development of ultrafast time-resolved spectroscopies developed in the 1980s. With a time-resolution in the femtosecond scale we may eventually capture the *real time* dynamics of HBs which lead to broad and sometimes structured stationary absorption spectra [21, 22]. Achievements in this area are impressive [23-26] yet more extensive investigations are necessary.

Theory is challenged by the quantum nature and multidimensionality, two specific features of HBs which are already quite intricate even in the gas phase. The small mass of the proton in a HB makes it the primary quantum nucleus and the phenomena one expects to encounter in a particular clear way are, for instance, zero-point energy effects, quantum tunneling, or coherent wave packet dynamics. While this is well established in the limit of one-dimensional models, the details of the multidimensional aspects of the dynamics of HBs are just accessible to experiments and numerical simulations. As for the condensed phase, the situation is more complicated. To include quantum effects into a simulation which is based on classical dynamics will be the ultimate goal for hydrogen bonded systems in condensed phase. In general a successful theoretical simulation concerning HB is highly challenging yet many fundamental questions can be distinctly elucidated with it.

1.2 General Description of Hydrogen Bonds

Let us first grasp some general aspects of HBs which is well established according to previous investigations. The traditional hydrogen bond A–H$\cdots$B is an attractive interaction between a proton donor A–H and a proton acceptor B, where A and B can be the same or different atoms. The most prominent effect due to this interaction/bonding is that the A–H bond length slightly increases which softens the potential energy curve and leads to a redshift of the frequency of the A–H bond stretching mode. As the HB strength increases the dynamics of the central proton becomes much more complicated than a free covalently bonded one described by a simple potential well. Actually the shape of the potential energy curve along the proton transfer reaction coordinate is qualitatively determined by the bond strength. As has been pointed out by Huggins [27], the (empirical) potential energy curves of the proton transfer between two oxygen atoms change from double minimum to single minimum when the O-O distance decreases. Most properties related to the HB vary according to the bond strength. Consequently the HBs can be classified into weak, moderate and strong ones by the bond energy.

Generally a weak HB is characterized by the bond energy less than 4 kcal/mol [14]. The weak bond may lead to a double minimum potential energy curve along the hydrogen transfer reaction coordinate with a rather high potential barrier but significantly lower than the free A–H covalent bond dissociation energy. The A$\cdots$B distance may vary from 3.1 Å to 4.3 Å. Fig. 1.1 shows a schematic view of such a potential curve for a symmetric double well case together with the low lying wave functions. The quantum tunneling effect is clearly demonstrated where the proton wave function penetrates to the central classically forbidden region. There is a tunneling splitting energy Δ defined by the energy difference

of the two nearly degenerate states. It is caused by the bonding interaction therefore it will increase when the bond strength increases like the case of two weakly coupled harmonic oscillators. The splitting energy Δ is proportional to the hydrogen tunneling rate and it increases for higher energy wave function pairs. The apparent consequence of the tunneling splitting is that the IR spectrum has a doublet structure since the initial state can be either one of the lowest pair of eigenstates. Fig. 1.1 shows the slight difference between excitations starting from opposite parities which in principal can be observed by high resolution IR spectroscopy experiments. Due to the weak bond strength, harmonic calculations based on a minimum configuration can provide reasonable results.

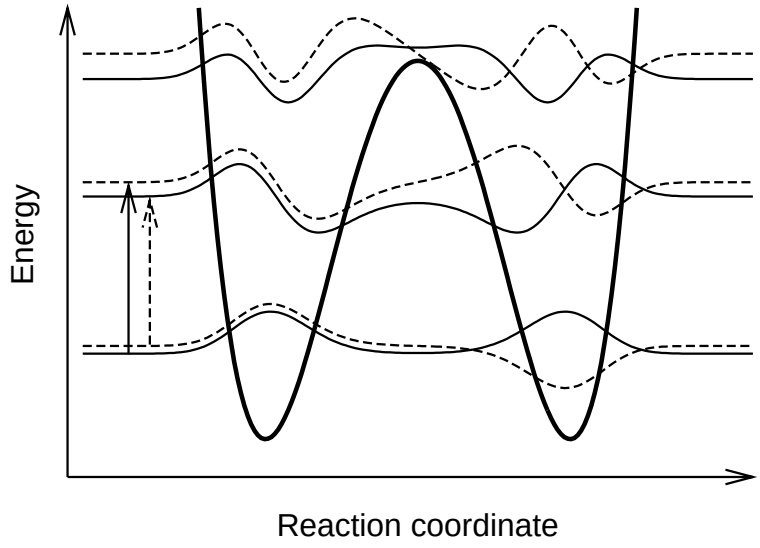

Figure 1.1: Schematic plot of potential energy curve and vibrational wave functions of weak hydrogen bonded system. The solid (dashed) curves are wave functions of even (odd) parity. The solid (dashed) arrow characterizes transition from even (odd) parity to odd (even) parity. See the text for more details.

The increase of the bond strength will decrease the potential barrier leading to a rather anharmonic potential energy curve along the hydrogen transfer reaction coordinate. In general the increase of bond strength leads to the increase of anharmonicity therefore increase of dimensionality of large amplitude motions. A medium strong HB is characterized by the bond energy varying from 4 to 14 kcal/mol. The A$\cdots$B distance is shortened and generally may vary from 2.4 Å to 3.3 Å. This kind of HBs can be found in many biological systems.

A strong HB is characterized by the bond energy larger than 14 kcal/mol. The strong bonding significantly decreases or even annihilate the potential barrier and leads to a quite flat potential energy curve to ensure high mobility of the bridging proton. Fig. 1.2 shows a

schematic view of such a potential curve for a symmetric double well case with vanishing barrier as well as the ground state wave function. As has been pointed out, the potential energy curve can also be single minimum for even stronger bonding. Even for the double potential well case the ground state will be found to be energetically above the barrier. Consequently the wave function has a single maximum exactly in the center with widely delocalized distribution which makes the proton motion strongly coupled to many other coordinates. The A$\cdots$B distance is further shortened to less than 2.7 Å. This kind of HBs can be found in some simple but quite important clusters which we will investigate in the next few chapters. Multidimensional or even full dimensional quantum investigations based on anharmonic potential energy surfaces are necessary for strong hydrogen bonded systems. This kind of HBs are also very important for some biological processes [15].

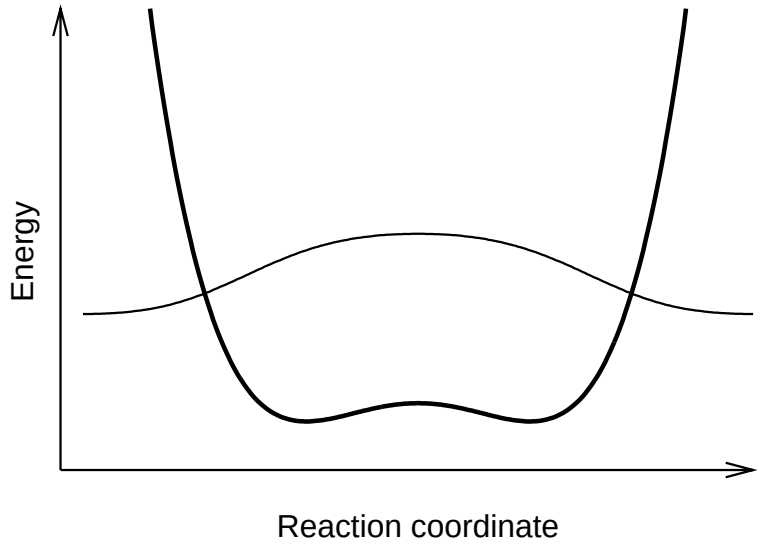

Figure 1.2: Schematic plot of potential energy curve and vibrational ground state wave function of strong hydrogen bonded system.

1.3 Recent Advances and Challenges

Having in mind the general picture of HBs let us now briefly review some recent advances. Charged clusters with strong hydrogen-bonds have attracted considerable interest recently due to the progress of IR spectroscopy and multidimensional quantum dynamical modeling [16, 17, 28, 29]. In particular the hydrated proton and its negative analogue, the hydrated hydroxide anion, have been investigated in quite some detail. They are believed to play key role for proton/hydroxide diffusion in aqueous media. The nature of the excess proton diffusion in water may throw light on the charge migration in biological systems

as well as many other commonly encountered reactions. The proton diffusion in water is not a real particle diffusion but a global structure deformation with charge migration [30, 31]. This process actually involves the breaking and reforming of several HBs as show in Fig. 1.3 for the mechanism of proton transfer along a water wire. In reality the water solvent is constructed by three dimensional hydrogen bonded networks.

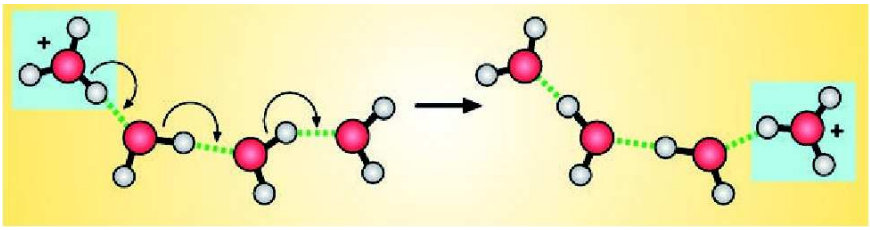

Figure 1.3: The Grotthuss shuttling process for the excess proton transfer along a water wire adapted from Ref. [31]. In this schematic view three HBs are involved.

Among varies protonated water clusters the Eigen cation $H_3O^+ \cdot (H_2O)_3$ and the Zundel cation $[H_2O \cdots H \cdots OH_2]^+$ are found to have significant importance for the proton conduction in solution. The former has the solvation hydronium structure with C_{3v} symmetry and the latter has the equally shared proton structure. A molecular dynamics investigation [32] shows the fluctuation between $H_3O^+ \cdot (H_2O)_3$ and $H^+ \cdot (H_2O)_2$ is the driven force for proton conduction. As shown in Fig. 1.4 the limiting $H^+ \cdot (H_2O)_2$ structure is the transition state for proton transfer in water and for the counterpart of hydroxide transfer the $[HO \cdots H \cdots OH]^-$ structure serves as transition state. Though it is not feasible to find isolated limiting structures mentioned above in solution, it is still of fundamental importance to extensively study this kind of charged clusters in gas phase to provide instructions for unraveling the complexity of solution.

The IR signatures of the motion of the proton shared by the two water molecules in $H^+ \cdot (H_2O)_2$ are found around 1000 cm^{-1}, signifying the exceptional strength of this HB. From the experimental point of view the first IR spectrum of the shared proton region has been reported in Ref. [28] using the infrared multiple-photon dissociation (IRMDP) technique triggered by free electron laser radiation. The interpretation, however, was hampered by the multiphoton nature of the measurement which prevented unambiguous assignment of intensities for the fundamental and low-order combination transitions. Subsequently, Johnson et al. reported an infrared vibrational predissociation (IRVPD) spectrum of the rare gas-tagged species. Since this yields intensity information for one-photon transitions the spectrum is much simpler showing in particular a prominent double peak at about 1000 cm^{-1} [33], See Fig. 1.5.

From the theoretical point of view, $H^+ \cdot (H_2O)_2$, is a prototype bringing together al-

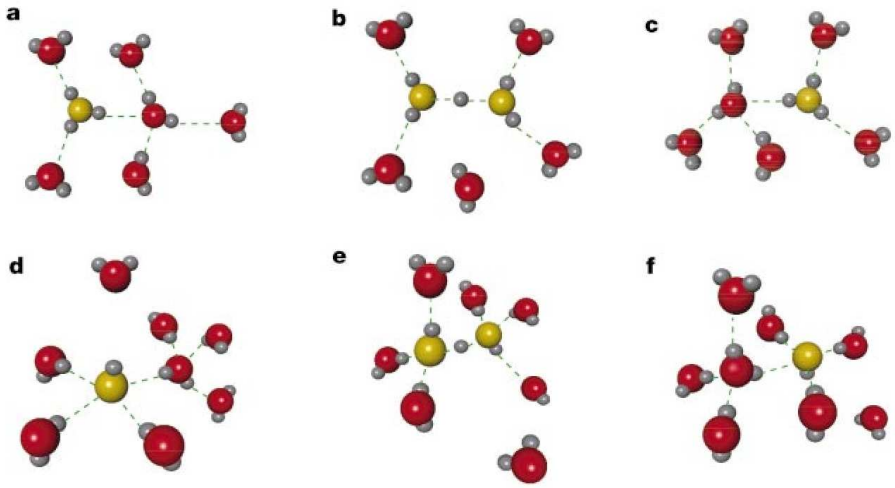

Figure 1.4: The schematic view of the proton transfer (panels a-c) and the hydroxide transfer (panels d-f) mechanisms in solution adapted from Ref. [31].

most all complications of HB research [34], i.e., a high-level quantum chemical potential energy surface (PES) is required for a multidimensional quantum dynamical problem. In fact there have been several reports on the spectrum including a reduced dimensional model [35], classical ab initio molecular dynamics simulations [36], and full-dimensional diffusion Monte Carlo and vibrational configuration interaction calculations [33]. But, only recently a full-dimensional quantum dynamical calculation based on multi configuration time dependent Hartree (MCTDH) approach [29] has been able to assign the double peak structure to a combination of the shared proton motion and wagging torsions of the water molecules [37, 38, 39]. The nearly perfect agreement between experiment and full dimensional quantum calculations is shown in Fig. 1.5 which demonstrates the capabilities of full dimensional quantum dynamics for gas phase phenomena.

Similar to the Zundel cation, the IR signatures of the monohydrated hydroxide anion $[HO\cdots H\cdots OH]^-$ is also as challenging due to the strong coupling of the shared proton and the other degrees of freedom. The first IR spectrum was measured by Johnson and coworkers using argon predissociation spectroscopy. In the range above 3000 cm^{-1} a sharp doublet was detected [40, 41] at about 3650 cm^{-1} which was subsequently assigned to the fundamental of the asymmetric stretching of the “free” OH groups doubled by the $HO\cdots OH$ torsional tunneling splitting [42]. As mentioned in Section 1.2 the tunneling splitting can cause a doublet of vibrational bands. The potential curve along the $HO\cdots OH$ torsion contains a double minimum with a barrier leading to tunneling splitting of several wavenumbers. The spectral range from 1000-1900 cm^{-1} is dominated by a peak at 1090 cm^{-1} which was attributed to a combination of the shared proton stretch, wag, and

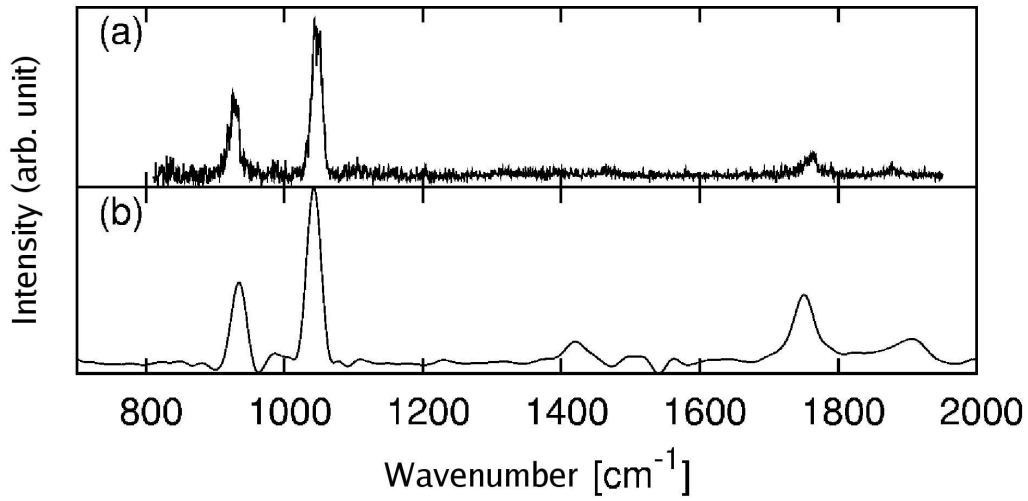

Figure 1.5: The measured and calculated IR spectra for the Zundel cation $H^+\cdot(H_2O)_2$ taken from Ref. [37]. The upper panel is the predissociation spectrum of $H^+\cdot(H_2O)_2\cdot$Ne complex and the lower panel is full dimensional quantum dynamics with MCTDH.

rock motions of the whole complex [43]. Effectively, this corresponds to a displacement of the shared proton away from the O$\cdots$O axis. The region below 1000 cm^{-1} was finally addressed in Ref. [44]. The spectrum is dominated by an intense and rather narrow peak at 697 cm^{-1} which has been assigned to the shared proton motion along the O$\cdots$O axis. In addition a small peak at 995 cm^{-1} with much weaker intensity was attributed to the other perpendicular bending of the shared proton, compared to the previously observed one at 1090 cm^{-1} . They have also observed one minor band at 940 cm^{-1} which might be the combinations of the shared proton stretching and O$\cdots$O stretching. Full dimensional quantum calculations [45, 46] based on diffusion Monte Carlo, vibrational configuration interaction approaches and exact diagonalization have qualitatively interpreted the observed bands detailed above.

Compared with the extensive investigations on charged water clusters, the protonated ammonia cluster ions $NH_4^+(NH_3)_n$ have received much less attention. However, they do play important roles in our everyday life such as nitrogen metabolism. The recent structural determination of an ammonia channel in an ammonia transporter protein [47] shows the ammonia transport process is accomplished by breaking and reforming of HBs due to different diffusion channels of protons and ammonia molecules. On the other hand, the study of proton conduction along ammonia wires has been motivated by the experimental work of Leutwyler et al. [48] on excited state hydrogen atom transfer along ammonia wire –O–H$\cdots$NH$_3\cdots$NH$_3\cdots$NH$_3\cdots$N. These authors demonstrated unidirectional H-atom transfer in the electronically excited state along the three-unit ammonia wire attached to

an aromatic molecule [48]. In spite of its significant importance the mechanism of proton transfer in this series of cations is still elusive due to insufficient investigations.

Early IR experimental investigations for $n = 1 - 10$ have been restricted to the 2600-4000 cm^{-1} range [49]. This study in particular suggested that in the smallest cluster, $H^+ \cdot (NH_3)_2$, the proton is equally shared between the two ammonia molecules, i.e., midway between the two N atoms. Clusters with $n = 5 - 8$ have been considered in the 1045-1091 cm^{-1} region with emphasis on the size dependence of the symmetric bend (ν_2) vibration of NH_3 reflecting the solvation shell structure [50]. The issue of spectral signatures of solvation shell structures has also been addressed by an free electron laser IR study of the spectral region from 1020-1210 cm^{-1} for $n = 5-8$ [51] and from 1070-1680 cm^{-1} for $n = 3, 4$ [52].

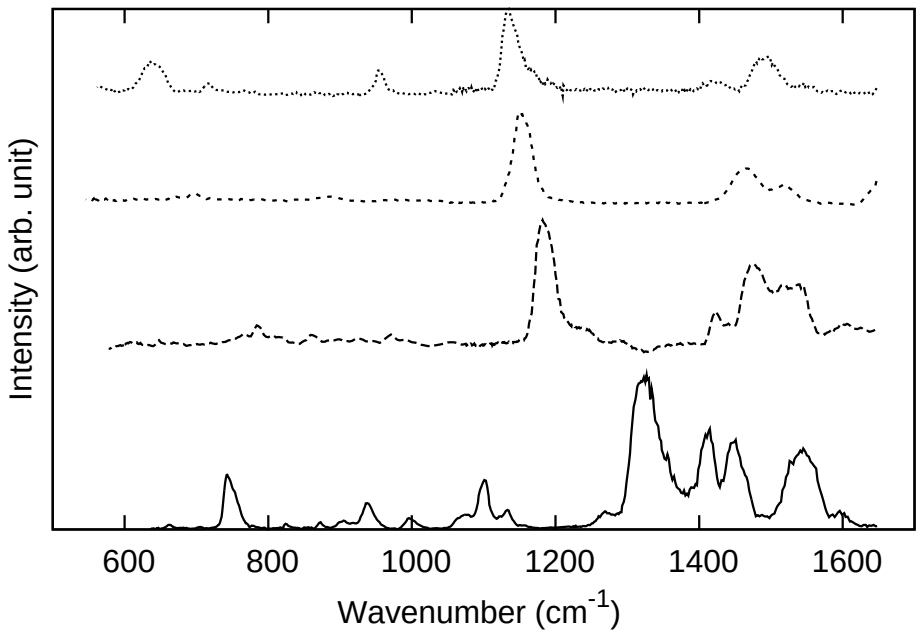

Figure 1.6: The IR spectra for $NH_4^+(NH_3)_n$ (n=1,4) clusters measured by the IRMPD method. From bottom to top the size increases from $n = 1$ to $n = 4$. The IRMPD experimental data are provided by Asmis group.

It is only very recently that a systematic investigation on IR spectra of these cations has been accomplished by Asmis group with IRMPD technique. The measured spectra region is from 600 cm^{-1} to 1700 cm^{-1} as shown in Fig. 1.6. Systematic redshifts of the most intensive bands with increasing cluster size have been observed. For $n = 1$ the spectrum of $H^+ \cdot (NH_3)_2 \cdot Ar$ has also been measured by Johnson group with IRVPD technique and the two experiments agree well with each other for major bands. The IRMPD spectrum involves absorption of many photons which makes it more likely to find all the IR active

bands in the given region, however, may also artificially increase the intensities of multi-photon bands. The IRVPD spectrum is more straightforward to interpret since only one photon is absorbed before the dissociation of $H^+\cdot(NH_3)_2\cdot Ar$ but the absorption bands structure may be perturbed by Ar messenger atom. To assign the measured IR bands we should perform high level theoretical simulations.

From theoretical point of view there are several investigations of protonated ammonia clusters by Meuwly et al. [53, 54, 55] using classical molecular dynamics together with DFT or self-consistent charge density functional tight-binding derived forces. The focus has been on proton conduction in free [53] and environmentally restricted [54] clusters, as well as on the stability and isomerization of clusters [55]. In terms of IR spectroscopy the predictions of Refs [53, 55] are based either on the harmonic approximation or on the assumption of classical nuclei. For instance, Fourier transformation of the dipole-dipole autocorrelation function along trajectories at 50 K for $H^+\cdot(NH_3)_2$ gave shared proton stretching vibration at 1610 cm^{-1}, the NH_3 umbrella vibration at 1000 cm^{-1}, and the $N\cdots N$ vibration at 465 cm^{-1} [55]. For $n > 1$ only spectra in the region $> 2000\,cm^{-1}$ have been reported in Ref. [55].

Apart from the IR spectra, some other experimental and theoretical techniques can also provide valuable informations concerning HBs. For example, isotope effects [7] are of substantial importance and utility. Experimental techniques such as NMR can directly probe the geometric isotope effects (GIEs) [56] and the kinetic isotope effects (KIEs) [57]. From the theoretical point of view, the gas phase GIEs can be clearly elucidated by the wavefunction and the condensed phase requires help of molecular dynamics. The KIEs are ratios of the reaction rate constants involving different isotopomers. The rate constants for high barrier reactions can be effectively predicted by classical transition state theory [58] while more reliable description should be based on quantum mechanics [59, 60] for the cases when tunneling is significant.

1.4 Goals and Structure of the Thesis

In this thesis we mainly focus on some prototypical hydrogen bonded clusters as reviewed in the previous section. Different from previous calculations, most of which rely on harmonic predictions and semi-classical simulations, we will do multidimensional quantum dynamics. For this purpose we will develop a general theory for generating vibrational Hamiltonian which can be straightforwardly applied to both free and constrained systems. Then we will establish a reasonable reduced dimensional model to study the IR spectrum of $H^+\cdot(NH_3)_2$ quantum mechanically and assign the very recent experimental spectrum

shown in Fig. 1.6, which can not be well explained by previous theoretical investigations. We will also rationalize and apply harmonic predictions to assign IR spectra of larger protonated ammonia clusters. Concerning the $[HO\cdots H\cdots OH]^-$ anion, there are six isotopomers of which only two have been investigated with full dimensional quantum dynamics. We will do full dimensional study for all the six isotopomers to get general characteristics as well as to confirm or improve the previous results of geometric and energetic isotope effects. Finally our investigations will go to the condensed phase. We will develop a new numerical realization of reaction rate constant calculations and illustrate its applicability and predictability by preliminary calculations.

The subsequent chapters will be arranged in the following way. Chapter 2 provides a general method for constructing the vibrational Hamiltonian and solving multidimensional Schrödinger equation under the Born-Oppenheimer approximation as a theoretical basis for the other chapters. In Chapter 3 multidimensional quantum calculations on geometry and IR spectrum of $H^+\cdot(NH_3)_2$ are performed with comparison to experiments. Chapter 3 also presents the corresponding results for $NH_4^+(NH_3)_n$ (n=2-4), for which the harmonic approximation gives reasonable results. In Chapter 4 the full dimensional quantum calculations of $[HO\cdots H\cdots OH]^-$ and all its different isotopomers are performed focusing on the energetic and geometric isotope effects. In Chapter 5 the major topic is about the condensed phase. A general theory of reaction path/surface Hamiltonian and a numerical method to calculate reaction rate constants are introduced. Then we generate a model Hamiltonian based on 6-Aminofulvene-1-aldimine molecule and perform some preliminary calculations. Chapter 6 summarizes the work presented in this thesis and makes some brief remarks about ongoing and future work.

Chapter 2

Vibrational Hamiltonian Theory and Method for Application

2.1 Introduction

In the last few decades detailed investigations on chemical reactions at the molecular level have been accomplished both experimentally and theoretically. Concerning any theoretical simulations the first task is to generate an appropriate system Hamiltonian. The full system Hamiltonian contains the molecular part, the environmental part and their interaction part. In general the molecular Hamiltonian can be generated on the $ab\ initio$ level while the latter two parts have to be treated by parametrization, other semi-classical or classical methods up to now. However, the molecular Hamiltonian is sufficient to describe the gas phase phenomena since the coupling between a molecule and the environment is ignorable. As for the condensed phase, the kernel part is still the molecular Hamiltonian.

The molecular Hamiltonian describes the Coulomb interaction between many electrons and nuclei. Due to the significant difference in mass between an electron ($m_e < 10^{-30}$ kg) and a nucleus ($m_{nuc} > 10^{-27}$ kg), one can consider the nuclei to be stationary on the time scale of electronic motion and the electrons relaxed to the ground state before the next motion of nuclei. This approximation of separating electronic and nuclear motion is known as the Born-Oppenheimer approximation [61] and holds in general if $(m_e/m_{nuc})^{1/4} \ll 1$. The expression for electronic Hamiltonian is trivial and in most cases it will be directly solved by quantum chemistry programs like Gaussian [62] to provide PES for the vibration of the nuclei. In this chapter we only focus on the vibrational Hamiltonian of the nuclei including the kinetic and potential energy operators which need to be expressed in terms of appropriate variables to simplify the numerical calculations.

Most of the existing theoretical investigations mainly deal with reaction path/surface

Hamiltonians which involve one or two large amplitude reaction coordinates while the rest are approximated as small vibrations orthogonal to the reaction coordinates [63-67]. This kind of Hamiltonians have simple forms and make quite good approximations for rigid systems. However it is inconvenient to describe floppy systems like strong hydrogen bonded systems with such Hamiltonians. As mentioned in the previous chapter the strong hydrogen bonded systems contains correlated motion of many degrees of freedom. In the following we introduce a concise method to generate $ab\ initio$ level vibrational Hamiltonian in terms of arbitrary coordinates as well as the solution to the corresponding multidimensional Schrödinger Equation.

2.2 Kinetic Energy Quantization

Let us first consider the kinetic energy quantization. The kinetic energy operator (KEO) in terms of arbitrary coordinates has been discussed by Podlosky with intricate tensor analysis [68] right after the foundation of the Schrödinger equation. Later studies are to some extent based on the same mathematical techniques [69, 70, 71]. Approximate KEOs using normal mode coordinates are widely adopted which go back to contributions by Eckart [72], Wilson [73], and Watson [74]. In particular, the Eckart equations [72] enable one to determine an orientation of molecule fixed axes suitable for using normal modes. The details of the derivation of a rovibrational Hamiltonian can be found in Ref. [73]. A significant simplification of this rovibrational Hamiltonian in terms of normal coordinates has been achieved by Watson [74, 75]. In fact the Watson Hamiltonian served as a starting point for many later investigations and is implemented, e.g., in the MULTIMODE program of Bowman, Carter, and coworkers [76]. In principle normal mode coordinates provide a very compact representation of the PES which is taylored, however, to the stationary point for which they have been defined. For large amplitude motions away from this stationary point the above mentioned reaction surface approach or the use of general curvilinear coordinates such as valance coordinates [71] are more suitable. A detailed discussion of advantages and disadvantages of various coordinates for rovibrational Hamiltonians has been presented, e.g., in Ref. [77].

In recent years Gatti and coworkers have developed a general scheme for deriving a KEO with vector parametrization, i.e., the non-trivial coordinates are expressed with $N-1$ real vectors for a system of N atoms [78, 79, 80]. This scheme is quite successful and convenient for a full dimensional description [81]. However, often one needs a reduced dimensional description for a constrained system [82, 83]. In general it is not possible, or not convenient, to express the coordinates as components of real vectors for

constrained systems. Numerical alternatives to the analytical determination of the KEO have also been suggested in Ref. [84, 85]. Here we introduce a rather straightforward physical method of kinetic energy quantization scheme which directly quantizes the classical Lagrange/Hamilton mechanics [86]. The method can be directly applied to both free systems and constrained systems by following the same procedure summarized in Section 2.2.1.

2.2.1 General Theory for Kinetic Energy Quantization

In the present method we only consider the most common cases where the kinetic energy includes purely quadratic terms and potential energy does not depend on the velocity, though the generalization would be straightforward. The classical Lagrangian/Hamiltonian in terms of arbitrary variables can be written as

$$\begin{aligned} L(\boldsymbol{Q},\dot{\boldsymbol{Q}},t) &= T(\dot{\boldsymbol{Q}}) - V(\boldsymbol{Q}) = \frac{1}{2}\dot{\boldsymbol{Q}}^{\dagger}\mathbf{M}\dot{\boldsymbol{Q}} - V(\boldsymbol{Q}) \\ H(\boldsymbol{Q},\boldsymbol{P}) &= T(\boldsymbol{P}) + V(\boldsymbol{Q}) = \frac{1}{2}\boldsymbol{P}^{\dagger}\mathbf{M}^{-1}\boldsymbol{P} + V(\boldsymbol{Q}), \end{aligned} \tag{2.1}$$

where $\boldsymbol{Q}$ and $\boldsymbol{P}$ are single column vectors of the generalized coordinates and corresponding conjugate momenta, respectively. The generalized momentum vector is defined as $\boldsymbol{P} = \frac{\partial L}{\partial \dot{\boldsymbol{Q}}} = \mathbf{M}\dot{\boldsymbol{Q}}$. The generalized mass matrix $\mathbf{M}$, normally a function of coordinates, is defined to be Hermitian and "†" means Hermitian conjugate which is equivalent to the transpose in classical mechanics. Classical trajectories can be obtained by this Lagrangian/Hamiltonian provided initial conditions are known. To obtain the quantum Hamiltonian operator, the major task is to obtain the quantum KEO in coordinate representation.

Since the choice of coordinates is quite arbitrary in Eq. (2.1), we start with Cartesian ones $\{\boldsymbol{X},\boldsymbol{P_X}\}$. In this section all the subscripts $_X$ are associated with Cartesian coordinates. The operator for each component of the momentum vector is Hermitian

$$(\hat{\boldsymbol{P}_{\boldsymbol{X}}}^{\dagger})_j = (\hat{\boldsymbol{P}_{\boldsymbol{X}}})_j = -i\hbar\frac{\partial}{\partial X_j}. \tag{2.2}$$

For non-Cartesian coordinates we define the momentum operators in the same way as the first order derivative operators

$$\hat{\boldsymbol{P}} = -i\hbar\frac{\partial}{\partial \boldsymbol{Q}}. \tag{2.3}$$

To obtain the quantum KEO in terms of non-Cartesian coordinates, the coordinate transformation between the Cartesian and non-Cartesian ones should be performed. Suppose we know the relation between two sets of coordinates, which is just the way how we

define the coordinates, as an invertible mapping $\boldsymbol{Q} = \boldsymbol{Q}(\boldsymbol{X})$. The following relations can be derived easily by exploiting the general rules of derivative of composite functions

$$\begin{aligned}
\dot{\boldsymbol{Q}} &= \frac{\partial \boldsymbol{Q}}{\partial \boldsymbol{X}} \dot{\boldsymbol{X}} \\
\hat{\boldsymbol{P}} &= \left(\frac{\partial \boldsymbol{X}}{\partial \boldsymbol{Q}}\right)^{\dagger} \hat{\boldsymbol{P}_{\boldsymbol{X}}} \\
\frac{\partial \boldsymbol{Q}}{\partial \boldsymbol{X}} &= \left(\frac{\partial \boldsymbol{X}}{\partial \boldsymbol{Q}}\right)^{-1},
\end{aligned} \tag{2.4}$$

where the matrix elements of the transformation matrices are defined as

$$\left(\frac{\partial \boldsymbol{Q}}{\partial \boldsymbol{X}}\right)_{ij} = \frac{\partial Q_i}{\partial X_j} \qquad \left(\frac{\partial \boldsymbol{X}}{\partial \boldsymbol{Q}}\right)_{ij} = \frac{\partial X_i}{\partial Q_j}. \tag{2.5}$$

The above criteria to define elements of this kind of matrices is adopted in the whole thesis, which means $\frac{\partial \boldsymbol{Q}}{\partial X_j}$ is a single column vector while $\frac{\partial X_i}{\partial \boldsymbol{Q}}$ is a single row vector. Note an operator $\frac{\partial}{\partial \boldsymbol{Q}}$ is defined to be a single column vector. The quantum KEO in terms of non-Cartesian coordinates can be obtained by this coordinate transformation

$$\begin{aligned}
\hat{T} &= \frac{1}{2} \hat{\boldsymbol{P}_{\boldsymbol{X}}}^{\dagger} \mathbf{M}_{\mathbf{X}}^{-1} \hat{\boldsymbol{P}_{\boldsymbol{X}}} \\
&= \frac{1}{2} \hat{\boldsymbol{P}}^{\dagger} \frac{\partial \boldsymbol{Q}}{\partial \boldsymbol{X}} \mathbf{M}_{\mathbf{X}}^{-1} (\frac{\partial \boldsymbol{Q}}{\partial \boldsymbol{X}})^{\dagger} \hat{\boldsymbol{P}},
\end{aligned} \tag{2.6}$$

where $\mathbf{M}_{\mathbf{X}}$ is the diagonal Cartesian mass matrix consisting of real mass associated with each Cartesian coordinate.

The momentum operator vector $\hat{\boldsymbol{P}}$ can be replaced by the derivative operator according to previous definition, i.e., $\hat{\boldsymbol{P}} = -i\hbar \frac{\partial}{\partial \boldsymbol{Q}}$. However we should find out the expression for the Hermitian conjugate of momentum operator (HCMO) vector $\hat{\boldsymbol{P}}^{\dagger}$. Since one has the relation between $\hat{\boldsymbol{P}}$ and the Cartesian one $\hat{\boldsymbol{P}_{\boldsymbol{X}}}$ it is not difficult to directly apply the definition of Hermitian conjugate to Eq. (2.4)

$$\begin{aligned}
\left(\hat{\boldsymbol{P}}^{\dagger}\right)_i &= \left(\left(\left(\frac{\partial \boldsymbol{X}}{\partial \boldsymbol{Q}}\right)^{\dagger} \hat{\boldsymbol{P}_{\boldsymbol{X}}}\right)^{\dagger}\right)_i \\
&= \left(\hat{\boldsymbol{P}_{\boldsymbol{X}}}^{\dagger} \frac{\partial \boldsymbol{X}}{\partial \boldsymbol{Q}}\right)_i \\
&= \sum_j \left(\hat{\boldsymbol{P}_{\boldsymbol{X}}}\right)_j \left(\frac{\partial \boldsymbol{X}}{\partial \boldsymbol{Q}}\right)_{ji} \\
&= \sum_j \left(\frac{\partial \boldsymbol{X}}{\partial \boldsymbol{Q}}\right)_{ji} \left(\hat{\boldsymbol{P}_{\boldsymbol{X}}}\right)_j + \sum_j \left[\left(\hat{\boldsymbol{P}_{\boldsymbol{X}}}\right)_j, \left(\frac{\partial \boldsymbol{X}}{\partial \boldsymbol{Q}}\right)_{ji}\right] \\
&= \left(\hat{\boldsymbol{P}}\right)_i + \sum_j \left[\left(\hat{\boldsymbol{P}_{\boldsymbol{X}}}\right)_j, \left(\frac{\partial \boldsymbol{X}}{\partial \boldsymbol{Q}}\right)_{ji}\right],
\end{aligned} \tag{2.7}$$

where the notation $[\hat{A}, \hat{B}]$ means the commutator of two operators.

Eq. (2.7) shows the non-Hermiticity of generalized momenta associated with the non-Cartesian coordinates. Additional terms appear due to the non-commutability of the Cartesian momenta and the transformation matrix. In some cases the new momenta are still Hermitian provided we only perform a coordinate independent transformation, e.g., the rotation in three dimensional space or the normal modes transformation. Using the basic commutator $[\hat{X}_j, (\hat{P_X})_k] = i\hbar\delta_{jk}$, Eq. (2.7) can be simplified as (see also Ref. [87])

$$(\hat{\boldsymbol{P}}^{\dagger})_k = (\hat{\boldsymbol{P}})_k - i\hbar \sum_j \left(\frac{\partial}{\partial X_j} \frac{\partial X_j}{\partial Q_k} \right)^{\circ}. \tag{2.8}$$

Here the superscript $^{\circ}$ means a differential operator inside the bracket can not operate on functions outside, namely the result is just a normal function of coordinates.

Eq. (2.8) clearly shows the relation between a momentum operator and its Hermitian conjugate. It should be mentioned that any functions of coordinates $\{f_j(Q_j)\}$ can be multiplied from the left to the derivative operator in Eq. (2.3) for different schemes of momenta quantization, i.e., $(\hat{\boldsymbol{P}})_j = -i\hbar \cdot f_j(Q_j) \cdot \frac{\partial}{\partial Q_j}$ is also an acceptable scheme. Since this kind of momentum operators are generally non-Hermitian we actually have no priority to set $f_j(Q_j) = 1$. For different schemes of momenta quantization, the HCMOs will vary correspondingly to keep the KEO invariant. This enable us to optimize momenta quantization schemes conveniently if necessary. In other words, with proper prepositioned functions one can obtain desired forms of momentum operators, e.g., symmetric forms.

With Eq. (2.6) and Eq. (2.7) we get the general scheme of constructing KEOs in terms of arbitrary coordinates. However, the final structure seems to be complicated and actually it can be simplified. Now we compare Eq. (2.6) and Eq. (2.1) by considering the invariance of the classical kinetic energy

$$\begin{aligned} T &= \frac{1}{2}\dot{\boldsymbol{Q}}^{\dagger}\mathbf{M}\dot{\boldsymbol{Q}} \\ &= \frac{1}{2}\dot{\boldsymbol{X}}^{\dagger}\mathbf{M}_{\mathbf{X}}\dot{\boldsymbol{X}} \\ &= \frac{1}{2}\dot{\boldsymbol{Q}}^{\dagger}\left(\frac{\partial \boldsymbol{X}}{\partial \boldsymbol{Q}}\right)^{\dagger}\mathbf{M}_{\mathbf{X}}\frac{\partial \boldsymbol{X}}{\partial \boldsymbol{Q}}\dot{\boldsymbol{Q}}. \end{aligned} \tag{2.9}$$

Since $\dot{\boldsymbol{Q}}$ can be any vector we must have the relation $\mathbf{M} = \left(\frac{\partial \boldsymbol{X}}{\partial \boldsymbol{Q}}\right)^{\dagger}\mathbf{M}_{\mathbf{X}}\frac{\partial \boldsymbol{X}}{\partial \boldsymbol{Q}}$. Calculate the inverse of both sides we immediately see that the complicated central part $\frac{\partial \boldsymbol{Q}}{\partial \boldsymbol{X}}\mathbf{M}_{\mathbf{X}}^{-1}\left(\frac{\partial \boldsymbol{Q}}{\partial \boldsymbol{X}}\right)^{\dagger}$ in Eq. (2.6) is exactly $\mathbf{M}^{-1}$ in Eq. (2.1). The final KEO is therefore simplified as

$$\hat{T} = \frac{1}{2}\hat{\boldsymbol{P}}^{\dagger}\mathbf{M}^{-1}\hat{\boldsymbol{P}}. \tag{2.10}$$

This means we can directly exploit the result of Eq. (2.1) and quantize the generalized momenta without the knowledge of the Cartesian kinetic energy. All we need are the generalized mass matrix **M** and the definition of coordinates which both appear in Eq. (2.1).

Therefore we can identify a concise and physically transparent scheme to construct the KEO:

1. Get the classical kinetic energy and make sure the mass matrix is symmetric, namely the same structure as Eq. (2.1), $T(\dot{\boldsymbol{Q}}) = \frac{1}{2}\dot{\boldsymbol{Q}}^{\dagger}\mathbf{M}\dot{\boldsymbol{Q}}$.

2. Exploit Eq. (2.7) or Eq. (2.8) to express HCMOs $\hat{\boldsymbol{P}}^{\dagger}$ in terms of $\hat{\boldsymbol{P}}$ and some functions of $\boldsymbol{Q}$.

3. Calculate the inverse matrix of **M** hence the formal quantum KEO reads $\hat{T} = \frac{1}{2}\hat{\boldsymbol{P}}^{\dagger}\mathbf{M}^{-1}\hat{\boldsymbol{P}}$.

4. Replace $\hat{\boldsymbol{P}}$ by $-i\hbar\frac{\partial}{\partial \boldsymbol{Q}}$ for coordinate representation.

The first step is quite familiar to everyone and one can choose arbitrary coordinates to get the classical kinetic energy. Actually we will introduce a useful partition method in Section 2.2.3 which will significantly simplify this issue. The remaining three steps are quite straightforward to follow. We can see the major derivation effort is the second step concerning the HCMOs according to Eq. (2.7) or Eq. (2.8). However, if the coordinates are spherical coordinates the HCMOs are familiar to us. In Section 2.2.4 we will provide a detailed study on the HCMOs in spherical coordinates.

After obtaining the KEO, we should also mention the volume element for integration. Since we start from Cartesian coordinates and all that we have done is a coordinate transformation. That is to say, the Euclidean normalization remains correct

$$d\tau = d\tau_X = \prod_i dX_i = |\mathrm{Det}\left(\frac{\partial \boldsymbol{X}}{\partial \boldsymbol{Q}}\right)| \prod_i dQ_i. \tag{2.11}$$

2.2.2 KEOs for Systems with Constraints

Reduced dimensional descriptions are always necessary for large systems. In the following we will give the general description for systems with constraints. Consider a system with some active coordinates $\boldsymbol{Q}_1$ and some frozen coordinates $\boldsymbol{Q}_0$. The full dimensional coordinates and corresponding conjugate momenta read

$$\boldsymbol{Q} = \begin{pmatrix} \boldsymbol{Q}_1 \\ \boldsymbol{Q}_0 \end{pmatrix} \qquad \boldsymbol{P} = \begin{pmatrix} \boldsymbol{P}_1 \\ \boldsymbol{P}_0 \end{pmatrix} . \tag{2.12}$$

The constraint conditions are given by $\dot{\boldsymbol{Q}}_0 = 0$. Thus we can obtain the constrained classical kinetic energy

$$\begin{aligned} T &= \frac{1}{2}\dot{\boldsymbol{Q}}^\dagger \mathbf{M} \dot{\boldsymbol{Q}} \\ &= \frac{1}{2}\begin{pmatrix} \dot{\boldsymbol{Q}}_1^\dagger & \dot{\boldsymbol{Q}}_0^\dagger \end{pmatrix} \begin{pmatrix} \mathbf{M}_{11} & \mathbf{M}_{10} \\ \mathbf{M}_{01} & \mathbf{M}_{00} \end{pmatrix} \begin{pmatrix} \dot{\boldsymbol{Q}}_1 \\ \dot{\boldsymbol{Q}}_0 \end{pmatrix} \\ &= \frac{1}{2}\dot{\boldsymbol{Q}}_1^\dagger \mathbf{M}_{11} \dot{\boldsymbol{Q}}_1, \end{aligned} \tag{2.13}$$

where $\mathbf{M}_{ij}$ are corresponding sub-matrices.

To get the quantum KEO we have to rewrite the constraint conditions in terms of momenta. According to the definition of momenta it is not difficult to find the following relation

$$\begin{aligned} \begin{pmatrix} \dot{\boldsymbol{Q}}_1 \\ \dot{\boldsymbol{Q}}_0 \end{pmatrix} &= \begin{pmatrix} \mathbf{M}_{11} & \mathbf{M}_{10} \\ \mathbf{M}_{01} & \mathbf{M}_{00} \end{pmatrix}^{-1} \begin{pmatrix} \boldsymbol{P}_1 \\ \boldsymbol{P}_0 \end{pmatrix} \\ &= \begin{pmatrix} \mathbf{A} & \mathbf{B} \\ \mathbf{C} & \mathbf{D} \end{pmatrix} \begin{pmatrix} \boldsymbol{P}_1 \\ \boldsymbol{P}_0 \end{pmatrix}, \end{aligned} \tag{2.14}$$

where $\begin{pmatrix} \mathbf{A} & \mathbf{B} \\ \mathbf{C} & \mathbf{D} \end{pmatrix}$ is the inverse of matrix $\mathbf{M}$. Thus it is not difficult to rewrite the constraint conditions as $\mathbf{C}\boldsymbol{P}_1 + \mathbf{D}\boldsymbol{P}_0 = 0$ or $\boldsymbol{P}_0 = -\mathbf{D}^{-1}\mathbf{C}\boldsymbol{P}_1$. After quantization we get the constraint relation for the corresponding quantum operators, i.e., $\hat{\boldsymbol{P}}_0 = -\mathbf{D}^{-1}\mathbf{C}\hat{\boldsymbol{P}}_1$. Based on this point we can obtain the quantum KEO

$$\begin{aligned} \hat{T} &= \frac{1}{2}\hat{\boldsymbol{P}}^\dagger \mathbf{M}^{-1} \hat{\boldsymbol{P}} \\ &= \frac{1}{2}\begin{pmatrix} \hat{\boldsymbol{P}}_1^\dagger & \hat{\boldsymbol{P}}_0^\dagger \end{pmatrix} \begin{pmatrix} \mathbf{M}_{11} & \mathbf{M}_{10} \\ \mathbf{M}_{01} & \mathbf{M}_{00} \end{pmatrix}^{-1} \begin{pmatrix} \hat{\boldsymbol{P}}_1 \\ \hat{\boldsymbol{P}}_0 \end{pmatrix} \\ &= \frac{1}{2}\begin{pmatrix} \hat{\boldsymbol{P}}_1^\dagger & (-\mathbf{D}^{-1}\mathbf{C}\hat{\boldsymbol{P}}_1)^\dagger \end{pmatrix} \begin{pmatrix} \mathbf{A} & \mathbf{B} \\ \mathbf{C} & \mathbf{D} \end{pmatrix} \begin{pmatrix} \hat{\boldsymbol{P}}_1 \\ -\mathbf{D}^{-1}\mathbf{C}\hat{\boldsymbol{P}}_1 \end{pmatrix} \\ &= \frac{1}{2}\hat{\boldsymbol{P}}_1^\dagger \left(\mathbf{A} - \mathbf{B}\mathbf{D}^{-1}\mathbf{C}\right) \hat{\boldsymbol{P}}_1 \\ &= \frac{1}{2}\hat{\boldsymbol{P}}_1^\dagger \mathbf{M}_{11}^{-1} \hat{\boldsymbol{P}}_1. \end{aligned} \tag{2.15}$$

The final result is quite compact. Compare Eq. (2.13) with Eq. (2.15) we find that the *same procedure* mentioned in the full dimensional case can be followed provided we only consider the active coordinates and completely ignore the frozen ones from the very beginning when we generate the classical Lagrangian. This is an attractive point since the present scheme only requires the classical Lagrangian for a constrained system which can be obtained by traditional methods.

2.2.3 A General Method on the Partition of Classical Kinetic Energy

By now we have explained the general theory of kinetic energy quantization starting from the classical Lagrangian. In the following we will introduce a method for obtaining the classical kinetic energy with a partition technique which will greatly simplify the problem in most cases. It is quite convenient to divide a large system into small subsystems especially when a subsystems has certain symmetry. If we divide a system into N parts, the division can be quite arbitrary, the kinetic energy is a sum of the N subsystems. According to the König theorem [88] we have the following relation

$$T = \sum_{i=1}^{N} T_i^0 = T_C^0 + \sum_{i=1}^{N} T_i^C, \tag{2.16}$$

where T_A^B is the kinetic energy of the part A with respect to the reference frame defined by B. Here 0 is the laboratory reference frame and C is the center of mass reference frame.

In the special case when $N = 2$ the kinetic energy can be written as

$$\begin{aligned} T &= T_C^0 + T_1^C + T_2^C, \\ T &= T_1^0 + T_2^0 = T_{C_1}^0 + T_1^{C_1} + T_{C_2}^0 + T_2^{C_2}. \end{aligned} \tag{2.17}$$

With the help of the two-body relation $T_{C_1}^0 + T_{C_2}^0 = T_C^0 + T_{C_1}^{C_2}$ we finally have

$$T_1^C + T_2^C = T_1^{C_1} + T_2^{C_2} + T_{C_1}^{C_2}, \tag{2.18}$$

where C_i is the center of mass of the ith part and $T_{C_1}^{C_2}$ is the kinetic energy of the center of mass of the first part with respect to the center of mass of the second part. It is quite transparent that $T_{C_1}^{C_2} = T_{C_2}^{C_1}$ since only two mass points are considered. In particular, if the two parts are both single atoms we have $T_1^{C_1} = T_2^{C_2} = 0$. Then Eq. (2.18) can be simplified as $T_1^C + T_2^C = T_{C_1}^{C_2} = T_{C_2}^{C_1}$, which is quite familiar from two-body mechanics. By exploiting Eq. (2.18) repeatedly we can easily express the total kinetic energy in terms of kinetic energies of subsystems which are much easier to obtain. We will see this point in the following chapters, e.g., Eq. (3.1). In the special case when all the N subsystems are single atoms this procedure will leads to the kinetic energy in terms of $N - 1$ Jacobi vectors (also called mobile coordinates).

2.2.4 Hermitian Conjugates of Momentum Operators

As mentioned in Section 2.2.1, the most tedious task for generating a KEO is to find out the expressions for the HCMOs. As an example let us consider the two dimensional (2D) polar coordinates $\{R, \theta\}$. The classical kinetic energy and the coordinate transformation between 2D Cartesian coordinates $\{x, y\}$ are quite familiar to us

$$\begin{aligned} T &= \frac{1}{2}m\dot{R}^2 + \frac{1}{2}mR^2\dot{\theta}^2 \\ x &= R\cos\theta \\ y &= R\sin\theta. \end{aligned} \tag{2.19}$$

To derive the HCMOs we simply follow Eq. (2.8). The required derivatives are listed out as follows

$$\begin{aligned} \frac{\partial x}{\partial R} &= \cos\theta = \frac{x}{R} \\ \frac{\partial y}{\partial R} &= \sin\theta = \frac{y}{R} \\ \frac{\partial x}{\partial \theta} &= R\sin\theta = y \\ \frac{\partial y}{\partial \theta} &= R\cos\theta = x. \end{aligned} \tag{2.20}$$

Based on above equations it is straightforward to obtain the final results

$$\begin{aligned} \hat{P}_R^\dagger &= \hat{P}_R - i\hbar\left(\frac{\partial}{\partial x}\frac{x}{R} + \frac{\partial}{\partial y}\frac{y}{R}\right)^\circ \\ &= \hat{P}_R - i\hbar\left(\frac{\partial}{\partial x}\frac{x}{\sqrt{x^2+y^2}} + \frac{\partial}{\partial y}\frac{y}{\sqrt{x^2+y^2}}\right)^\circ \\ &= \hat{P}_R - \frac{i\hbar}{R} \\ \hat{P}_\theta^\dagger &= \hat{P}_\theta - i\hbar\left(\frac{\partial}{\partial x}y + \frac{\partial}{\partial y}x\right)^\circ \\ &= \hat{P}_\theta. \end{aligned} \tag{2.21}$$

Then we can write out the 2D polar coordinates KEO expression which can be found in many textbooks but they may not tell you why.

$$\begin{aligned} \hat{T} &= \frac{1}{2m}\hat{P}_R^\dagger\hat{P}_R + \frac{1}{2mR^2}\hat{P}_\theta^\dagger\hat{P}_\theta \\ &= -\frac{\hbar^2}{2m}\left(\frac{\partial}{\partial R} + \frac{1}{R}\right)\frac{\partial}{\partial R} - \frac{\hbar^2}{2mR^2}\frac{\partial}{\partial\theta}\frac{\partial}{\partial\theta} \\ &= -\frac{\hbar^2}{2m}\frac{1}{R}\frac{\partial}{\partial R}R\frac{\partial}{\partial R} - \frac{\hbar^2}{2mR^2}\frac{\partial^2}{\partial\theta^2}. \end{aligned} \tag{2.22}$$

Similarly, the KEO in terms of 3D spherical coordinates $\{R, \theta, \varphi\}$ can be obtained. The coordinate transformation between 3D spherical coordinates and 3D Cartesian ones $\{x, y, z\}$ is defined as

$$\begin{aligned} x &= R\sin\theta\cos\varphi \\ y &= R\sin\theta\sin\varphi \\ z &= R\cos\theta. \end{aligned} \tag{2.23}$$

Here we simply list out the corresponding HCMOs leading to the well known KEO for 3D spherical coordinates

$$\begin{aligned} \hat{P}_R^\dagger &= \hat{P}_R - \frac{2i\hbar}{R^2} = -i\hbar\frac{1}{R^2}\frac{\partial}{\partial R}R^2 \\ \hat{P}_\theta^\dagger &= \hat{P}_\theta - i\hbar\cot\theta = -i\hbar\frac{1}{\sin\theta}\frac{\partial}{\partial\theta}\sin\theta \\ \hat{P}_\varphi^\dagger &= \hat{P}_\varphi = -i\hbar\frac{\partial}{\partial\varphi} \\ \hat{T} &= -\frac{\hbar^2}{2m}\frac{1}{R^2}\frac{\partial}{\partial R}R^2\frac{\partial}{\partial R} - \frac{\hbar^2}{2mR^2}\frac{1}{\sin\theta}\frac{\partial}{\partial\theta}\sin\theta\frac{\partial}{\partial\theta} - \frac{\hbar^2}{2mR^2\sin^2\theta}\frac{\partial^2}{\partial\varphi^2}. \end{aligned} \tag{2.24}$$

For more details please see Appendix A.

So far we mentioned everything in laboratory reference frame (LRF). In most cases we may need one or more molecular reference frames (MRFs) to describe a molecule in terms of its natural motions, e.g., bond lengths and bond angles. Please note that we introduce MRF only to define coordinates. All the operators and equations in the thesis are written in LRF unless with special comments. In the following we will study the HCMOs associated with MRF spherical coordinates. Consider the LRF and a MRF defined by sets of unit vectors $\{\boldsymbol{e}_x, \boldsymbol{e}_y, \boldsymbol{e}_z\}$ and $\{\boldsymbol{e}_{x'}, \boldsymbol{e}_{y'}, \boldsymbol{e}_{z'}\}$, respectively. The relation between LRF and MRF is just an orthogonal transformation characterized by the three Euler angles $\{\vartheta, \phi, \chi\}$

$$\boldsymbol{e}_{\alpha'} = \mathbf{U}_z(\phi)\mathbf{U}_y(\vartheta)\mathbf{U}_z(\chi)\boldsymbol{e}_\alpha, \tag{2.25}$$

where $\alpha = x, y, z$ and $\mathbf{U}_\alpha$ is a rotation around $\boldsymbol{e}_\alpha$. The MRF can be obtained by applying three excessive rotations $\mathbf{U}_z(\chi)$, $\mathbf{U}_y(\vartheta)$ and $\mathbf{U}_z(\phi)$ to the LRF. The expression for the rotational transformation matrix $\mathbf{U}_\alpha$ and more details can be found in Appendix A.

Now let us consider a vector $\boldsymbol{R}_j$ characterized by three spherical coordinates $\{R_j, \theta_j, \varphi_j\}$ in the MRF. According to Appendix A we can express $\boldsymbol{R}_j$ as

$$\boldsymbol{R}_j = R_j\mathbf{U}_z(\phi)\mathbf{U}_y(\vartheta)\mathbf{U}_z(\chi)\mathbf{U}_z(\varphi_j)\mathbf{U}_y(\theta_j)\boldsymbol{e}_z. \tag{2.26}$$

This is a vector equation and we can obtain the Cartesian coordinates of $\boldsymbol{R}_j$ in the LRF by projecting the equation onto each LRF axis. Based on Eq. (2.26) we can exploit Eq. (2.8) to derive the expressions for HCMOs associated with MRF coordinates. The details are shown in Appendix A. The final results are quite concise and they actually have the same expression as those associated with LRF spherical coordinates. That is to say, for the momentum operators associated with $\boldsymbol{R}_j$ (R_j, θ_j, φ_j) the following relations are still valid

$$\begin{aligned}
\hat{P}^{\dagger}_{R_j} &= \hat{P}_{R_j} - \frac{2i\hbar}{R_j^2} = -i\hbar\frac{1}{R_j^2}\frac{\partial}{\partial R_j}R_j^2 \\
\hat{P}^{\dagger}_{\theta_j} &= \hat{P}_{\theta_j} - i\hbar\cot\theta_j = -i\hbar\frac{1}{\sin\theta_j}\frac{\partial}{\partial\theta_j}\sin\theta_j \\
\hat{P}^{\dagger}_{\varphi_j} &= \hat{P}_{\varphi_j} = -i\hbar\frac{\partial}{\partial\varphi_j}.
\end{aligned} \tag{2.27}$$

Appendix A also confirms that the momentum operators associated with MRF Cartesian coordinates are Hermitian. One no longer need to take effort to derive the expressions for HCMOs provided one uses spherical coordinates, Cartesian coordinates or combinations of both, no matter they are defined in the LRF or MRFs.

2.2.5 Angular Momentum and Rotation

For a system with N atoms we have $3N$ degrees of freedom (DOFs). Not all the $3N$ DOFs are important for certain topics. They are normally divided into three translational DOFs, three rotational and $3N-6$ vibrational ones. The three translational DOFs can be separated while the rest $3N-3$ DOFs are coupled. In general the rotational excitation energies are quite small compared with the vibrational ones therefore the two parts are approximately separated in many cases. It is better to express KEO as sum of the two parts and their coupling. As a consequence we need to introduce the angular momentum $\boldsymbol{J}$ which describes the rotational DOFs.

We can use three angles and $3N-6$ other coordinates to describe the coupled rotational and vibrational motions of the system. Specifically, we exploit 3D vector $\boldsymbol{Q}_{rot}$ defined as

$$\boldsymbol{Q}^{\dagger}_{rot} = (\ \vartheta \quad \phi \quad \chi\ )$$

containing the three Euler angles which connects the LRF and MRF according to Eq. (2.25). In this Section the subscript $_{rot}$ is related to rotation. The kinetic energy

and total angular momentum are defined as

$$\begin{aligned} 2T &= \sum_{i=1}^{N} m_i \dot{\boldsymbol{R}}_i^{\dagger} \dot{\boldsymbol{R}}_i \\ \boldsymbol{J} &= \sum_{i=1}^{N} m_i \boldsymbol{R}_i \times \dot{\boldsymbol{R}}_i, \end{aligned} \tag{2.28}$$

where $\times$ means vector product. The matrix product of a single row matrix and a single column one is equivalent to scalar product of two vectors. Note that $\dot{\boldsymbol{Q}}_{rot}$ is the angular velocity of MRF. Therefore the velocities can be re-expressed as

$$\dot{\boldsymbol{R}}_i = \dot{\boldsymbol{Q}}_{rot} \times \boldsymbol{R}_i + \dot{\boldsymbol{R}}'_i, \tag{2.29}$$

where $\dot{\boldsymbol{R}}'_i$ is the velocity of $\boldsymbol{R}_i$ measured in the MRF. With the help of Eq. (2.29) and the following vector algebra relations

$$\begin{aligned} \boldsymbol{R}_1 \times (\boldsymbol{R}_2 \times \boldsymbol{R}_3) &= (\boldsymbol{R}_1^{\dagger}\boldsymbol{R}_3)\boldsymbol{R}_2 - (\boldsymbol{R}_1^{\dagger}\boldsymbol{R}_2)\boldsymbol{R}_3 \\ \boldsymbol{R}_1^{\dagger}(\boldsymbol{R}_2 \times \boldsymbol{R}_3) &= \boldsymbol{R}_2^{\dagger}(\boldsymbol{R}_3 \times \boldsymbol{R}_1) = \boldsymbol{R}_3^{\dagger}(\boldsymbol{R}_1 \times \boldsymbol{R}_2) \\ (\boldsymbol{R}_1 \times \boldsymbol{R}_2)^{\dagger}(\boldsymbol{R}_1 \times \boldsymbol{R}_2) &= R_1^2 R_2^2 - (\boldsymbol{R}_1^{\dagger}\boldsymbol{R}_2)^2 \end{aligned}$$

we can rewrite the kinetic energy and angular momentum

$$\begin{aligned} 2T &= \sum_{i=1}^{N} m_i \left(R_i^2 \dot{\boldsymbol{Q}}_{rot}^{\dagger} \dot{\boldsymbol{Q}}_{rot} - (\dot{\boldsymbol{Q}}_{rot}^{\dagger}\boldsymbol{R}_i)^2 + \dot{\boldsymbol{R}}_i'^{\dagger} \dot{\boldsymbol{R}}'_i + 2\dot{\boldsymbol{Q}}_{rot}^{\dagger}(\boldsymbol{R}_i \times \dot{\boldsymbol{R}}'_i) \right) \\ \boldsymbol{J} &= \sum_{i=1}^{N} m_i \left(R_i^2 \dot{\boldsymbol{Q}}_{rot} - (\dot{\boldsymbol{Q}}_{rot}^{\dagger}\boldsymbol{R}_i)\boldsymbol{R}_i + (\boldsymbol{R}_i \times \dot{\boldsymbol{R}}'_i) \right). \end{aligned} \tag{2.30}$$

Using Eqs. (2.30) it is straightforward to derive the following relation

$$\boldsymbol{J} = \frac{\partial T}{\partial \dot{\boldsymbol{Q}}_{rot}}. \tag{2.31}$$

This is exactly the definition of the generalized momentum vector $\boldsymbol{P}_{rot}$ associated with the three Euler angles.

Now we can draw the following important conclusion. If the set of coordinates contains the three Euler angles $\{\vartheta, \phi, \chi\}$ which characterize the transformation between the LRF and a MRF, the total angular momentum vector is just the generalized momentum vector associated with the three Euler angles

$$\begin{aligned} J_{\vartheta} &= P_{\vartheta} = \frac{\partial T}{\partial \dot{\vartheta}} \\ J_{\phi} &= P_{\phi} = \frac{\partial T}{\partial \dot{\phi}} \\ J_{\chi} &= P_{\chi} = \frac{\partial T}{\partial \dot{\chi}} \\ \boldsymbol{J} &= \boldsymbol{e}_{\dot{\vartheta}} P_{\vartheta} + \boldsymbol{e}_{\dot{\phi}} P_{\phi} + \boldsymbol{e}_{\dot{\chi}} P_{\chi}. \end{aligned} \tag{2.32}$$

Since we may not have much idea about the directions of the angular velocities $\{\boldsymbol{e}_{\dot{\vartheta}}, \boldsymbol{e}_{\dot{\phi}}, \boldsymbol{e}_{\dot{\chi}}\}$, it is better to transform the expressions to the Cartesian components [73] in the LRF

$$\begin{aligned} J_x &= \sin\chi P_\vartheta - \csc\vartheta\cos\chi P_\phi + \cot\vartheta\cos\chi P_\chi \\ J_y &= \cos\chi P_\vartheta + \csc\vartheta\sin\chi P_\phi - \cot\vartheta\sin\chi P_\chi \\ J_z &= P_\chi. \end{aligned} \tag{2.33}$$

With the help of Eq. (2.33) it is straightforward to express the KEO in terms of total angular momentum and generalized momenta associated with vibrational DOFs. In other words, starting from Eq. (2.30) the KEO can be readily expressed as contributions of rotational part, vibrational part and their coupling. A detailed example can be found in Appendix B.

In reality when we study rotational motions we can assume all the generalized momenta associated with the vibrational DOFs are equal to zero since the vibrational excitations need much higher energy. On the other hand when we study the vibrational dynamics the rotational states may change simultaneously. However since the rotational excitation energies are much smaller we can normally ignore their influence on the position of each vibrational band of the spectrum. In addition, experiments can not distinguish rotational excitations. They only observed broadening for each vibrational band which is due to the combination with rotational excitations. Consequently we can set $\hat{\boldsymbol{J}} = 0$, namely $\hat{P}_\vartheta = \hat{P}_\phi = \hat{P}_\chi = 0$ for investigations on vibrational DOFs.

2.3 Generating Multidimensional Potential Energy Surface

Compared to the KEO, the potential energy operator in coordinate representation is relatively easy to obtain since it is just a normal function. The most simple way to generate the PES is to calculate point by point for the required configurations. However, the direct scanning of all required configurations may be quite time demanding. Even if we only scan 10 points for each degree of freedom, which will not give results of high accuracy, we still need 10^{N_D} data points for N_D-dimensional system. It is only possible for molecules with no more than three atoms provided we need sufficiently accurate PES. Thus we have to resort to other methods to reduce the calculation effort while maintaining the accuracy. Correlation expansion [89] of high dimensional PES is a quite good choice for large molecules since it only needs several low dimensional PESs instead of one high dimensional one. In the following we will reproduce correlation expansions of multidimensional functions in terms of different correlation orders in a concise way.

2.3.1 PES Expansion with Correlation Orders

Considering any multidimensional function $V(\boldsymbol{Q})$, we can write the Taylor expansion of this function as

$$\begin{aligned} V(\boldsymbol{Q}) &= [\hat{O}(\boldsymbol{Q})V(\boldsymbol{Q}=0)] \\ \hat{O}(\boldsymbol{Q}) &= 1+\sum_i Q_i\frac{\partial}{\partial Q_i}+\frac{1}{2!}\sum_{ij} Q_iQ_j\frac{\partial^2}{\partial Q_i\partial Q_j}+\cdots, \end{aligned} \tag{2.34}$$

where the vector $\boldsymbol{Q}$ contains all the variables. We show some simple case of $\hat{O}(\boldsymbol{Q})$ for reduced dimensional situations in the following equations

$$\begin{aligned} \hat{O}(Q_i) &= \sum_n \frac{Q_i^n}{n!}\frac{\partial^n}{\partial Q_i^n} = 1+Q_i\frac{\partial}{\partial Q_i}+\frac{1}{2!}Q_i^2\frac{\partial^2}{\partial Q_i^2}+\cdots \\ \hat{O}(Q_iQ_j) &= \sum_{mn}\frac{Q_i^mQ_j^n}{(m+n)!}(\frac{\partial}{\partial Q_i})^m(\frac{\partial}{\partial Q_j})^n \\ &= 1+Q_i\frac{\partial}{\partial Q_i}+Q_j\frac{\partial}{\partial Q_j} \\ &\quad +\frac{1}{2!}\left(Q_i^2\frac{\partial^2}{\partial Q_i^2}+Q_j^2\frac{\partial^2}{\partial Q_j^2}+2Q_iQ_j\frac{\partial^2}{\partial Q_i\partial Q_j}\right)+\cdots, \end{aligned} \tag{2.35}$$

where $\hat{O}(Q_iQ_j)$ means all the other components of $\boldsymbol{Q}$ are zero except Q_i and Q_j.

Provided we can tolerate the error of neglecting third and higher correlation orders we can rewrite the operator $\hat{O}(\boldsymbol{Q})$ as a combination of low-dimensional operators

$$\begin{aligned} \hat{O}(\boldsymbol{Q}) &= 1+\sum_i Q_i\frac{\partial}{\partial Q_i}+\frac{1}{2!}\sum_{ij}Q_iQ_j\frac{\partial^2}{\partial Q_i\partial Q_j}+\cdots \\ &= 1+\sum_i[\hat{O}(Q_i)-1]+\frac{1}{2!}\sum_{i\neq j}[\hat{O}(Q_iQ_j)-\hat{O}(Q_i)-\hat{O}(Q_j)+1]+\cdots \\ &= \frac{1}{2}(N_D-1)(N_D-2)-(N_D-2)\sum_i\hat{O}(Q_i)+\sum_{i<j}\hat{O}(Q_iQ_j)+\cdots, \end{aligned} \tag{2.36}$$

where N_D is the dimension of $\boldsymbol{Q}$. The final expansion of multi-dimensional function in terms of low-dimensional functions (Accurate up to the second correlation order) reads

$$V(\boldsymbol{Q})=\frac{1}{2}(N_D-1)(N_D-2)V(0)-(N_D-2)\sum_i V(Q_i)+\sum_{i<j}V(Q_iQ_j)+\cdots. \tag{2.37}$$

From Eq. (2.37) we can see only some two-dimensional PESs are needed to expand the high dimensional PES provided the accuracy up to second correlation order is sufficient.

In general, this kind of correlation expansion for PES in terms of bond lengths and bond angles converges faster than the normal Taylor expansion since the correlation expansion includes some high order contributions of the normal Taylor expansion. With the help of Eq. (2.37) the total number of data points required is only $\frac{1}{2}N_D(N_D-1)N_s^2$, where N_s is data points needed for each single dimension (assuming they are equal). The numerical simulation in the next chapters are based on the expansion of Eq. (2.37).

To gain the physical meaning of Eq. (2.37), we would like to introduce another equivalent form. Reset the energy reference such that $V^{(1)}(Q_i) = V(Q_i) - V(0)$ and define the correlation part of two dimensional function $V^{(2)}_{cor}(Q_iQ_j) = V(Q_iQ_j) - V^{(1)}(Q_i) - V^{(1)}(Q_j) - V(0)$. We can rewrite Eq. (2.37) as

$$V(\boldsymbol{Q}) = V(0) + \sum_i V^{(1)}(Q_i) + \sum_{i<j} V^{(2)}_{cor}(Q_iQ_j) + \cdots . \tag{2.38}$$

The expansion form of Eq. (2.38) is the same with that reported in Ref. [89]. The meaning of each term in Eq. (2.38) is quite transparent and can be easily generalized to including higher orders of correlations. In general any function can be divided into uncorrelated parts and different orders of correlated parts.

2.3.2 Fitting of PES within Predefined Symmetry

In some cases the PES $V(\boldsymbol{Q})$ should be fitted to an analytical function for efficient numerical simulation. PES fitting also provides the opportunity to decrease the quantum chemistry calculation effort by scanning densely around important configurations and sparsely for trivial area. However the fitting should conserve the symmetry of the PES to give convincing results. The most simple way is to linearly combine predefined basis functions $\{\phi^S_n(\boldsymbol{Q})\}$ which have the same symmetry as $V(\boldsymbol{Q})$

$$V(\boldsymbol{Q}) = \sum_n c_n \phi^S_n(\boldsymbol{Q}). \tag{2.39}$$

Various effective fitting methods can be found from previous studies [92, 93]. Here we briefly recall the most simple and common one, the least square method, which minimize the sum of squared residuals. Suppose we have a set of data $\{\boldsymbol{Q}_i, V_i\}$ and the fitting form shown in Eq. (2.39). The sum of squared residuals Δ is defined by

$$\begin{aligned}
\Delta &= \sum_i \left(V_i - V\left(\boldsymbol{Q}_i\right)\right)^2 \\
&= \sum_i \left(V_i - \sum_n c_n \phi^S_n(\boldsymbol{Q}_i)\right)\left(V_i - \sum_n c_n \phi^S_n(\boldsymbol{Q}_i)\right) \\
&\equiv (\boldsymbol{V} - \mathbf{F}\boldsymbol{c})^\dagger(\boldsymbol{V} - \mathbf{F}\boldsymbol{c}) \\
&= \boldsymbol{V}^\dagger\boldsymbol{V} + \boldsymbol{c}^\dagger(\mathbf{F}^\dagger\mathbf{F}\boldsymbol{c} - 2\mathbf{F}^\dagger\boldsymbol{V}),
\end{aligned} \tag{2.40}$$

where the vector $\boldsymbol{V}$ and $\boldsymbol{c}$ contain the data points $\{V_i\}$ and coefficients $\{c_n\}$, respectively. And the matrix $\mathbf{F}$ is defined by $F_{in} = \phi_n^S(\boldsymbol{Q}_i)$. Note that in the third line of the above equation we change the explicit summation to matrix product to simplify the notation and derivation. The optimized coefficients can be obtained by solving the linear equations $\{\frac{\partial \Delta}{\partial c_n} = 0\}$ which in matrix notation is simply

$$\begin{aligned} \frac{\partial \Delta}{\partial \boldsymbol{c}} &= \mathbf{F}^\dagger \mathbf{F}\boldsymbol{c} - \mathbf{F}^\dagger \boldsymbol{V} = 0 \\ \boldsymbol{c} &= (\mathbf{F}^\dagger \mathbf{F})^{-1} \mathbf{F}^\dagger \boldsymbol{V}. \end{aligned} \tag{2.41}$$

We only need to calculate the inverse of a real symmetric matrix $\mathbf{F}^\dagger\mathbf{F}$ which is numerically straightforward. If we add an additional weight $0 < w_i < 1$ to each point $\{\boldsymbol{Q}_i, V_i\}$ the final result becomes $\boldsymbol{c} = (\mathbf{F}^\dagger \mathbf{W} \mathbf{F})^{-1} \mathbf{F}^\dagger \mathbf{W} \boldsymbol{V}$ with $W_{ij} = w_i \delta_{ij}$.

2.4 Solving Multidimensional Schrödinger Equation

Having the vibrational Hamiltonian at hand we can directly solve the Schrödinger equation to interpret the phenomena we are interested in. Any observables can be obtained with the help of the time dependent wave function which is the solution of the time dependent Schrödinger equation

$$i\hbar \frac{\partial}{\partial t} \Psi(\boldsymbol{Q}, t) = H \Psi(\boldsymbol{Q}, t), \tag{2.42}$$

where $\boldsymbol{Q}$ denotes a set of general coordinates. For stationary phenomena we can alternatively solve the time independent Schrödinger equation

$$H \Psi_n(\boldsymbol{Q}) = E_n \Psi_n(\boldsymbol{Q}), \tag{2.43}$$

where E_n and $\Psi_n(\boldsymbol{Q})$ are the nth eigen energy and eigenstate, respectively. Once we have the solution of the time independent Schrödinger equation we can easily write the solution of the time dependent one as

$$\Psi(\boldsymbol{Q}, t) = \sum_n c_n e^{-iE_n t/\hbar} \Psi_n(\boldsymbol{Q}), \tag{2.44}$$

where c_n is the overlap integral between the initial state $\Psi(\boldsymbol{Q}, t = 0)$ and $\Psi_n(\boldsymbol{Q})$. The solution of the time dependent Schrödinger equation tends to be less time consuming as compared with the time independent one. However, the calculation effort for both cases increases exponentially with the dimension which strongly hampers any attempt of treating multidimensional systems with numerically exact methods. Among several schemes of speeding up the calculations, the MCTDH method [29, 90] as implemented

in the Heidelberg program package [91] developed by Meyer and coworkers provides a quite good approximation with only slight loss of accuracy, which makes fairly accurate solution of multidimensional Schrödinger equations possible. In the following Sections 2.4.1 - 2.4.2 we briefly review the essence of MCTDH for propagation of wave packets and calculation of stationary eigenstates [90].

2.4.1 Propagation of Wave Packets

The idea is borrowed from the MCSCF method in the many-electron theory. The multidimensional wave packet is expanded as a sum of Hartree products

$$\Psi(\boldsymbol{Q},t) = \sum_{\nu_1=1}^{n_1} \cdots \sum_{\nu_N=1}^{n_N} A_{\nu_1,\cdots,\nu_N} \varphi_{\nu_1}^{(1)}(Q_1,t) \cdots \varphi_{\nu_N}^{(N)}(Q_N,t), \tag{2.45}$$

where $\{A_{\nu_1,\cdots,\nu_N}\}$ are time-dependent coefficients and $\{\varphi_{\nu_j}^{(j)}(Q_j,t)\}$ are time dependent single particle functions (SPFs) which can be expanded as a superposition of time independent primitive basis functions in the traditional way. The discrete variable representation (DVR) is adopted to represent each SPF [90]. Different from the direct expansion in terms of time independent basis functions, the MCDTH method needs a much smaller number of optimized SPFs since they only cover necessary grid points for each specified moment of time. Fig. 2.1 clearly tell us how the SPFs adapt their shapes according to the time evolution of the wave packet.

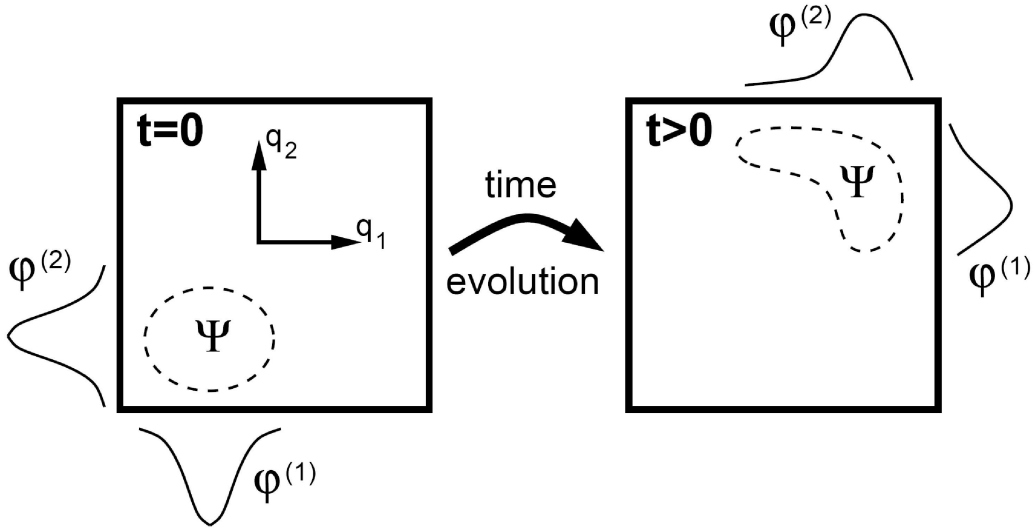

Figure 2.1: Schematic view of the SPFs $\{\varphi^{(j)}\}$ following the motion of the time dependent wave packet Ψ. Figure adapted from Ref. [34]

The equations of motion of the time-dependent coefficients $\{A_{\nu_1,\cdots,\nu_N}\}$ and SPFs $\{\varphi_{\nu_j}^{(j)}(Q_j,t)\}$ can be derived by replacing the wave function $\Psi(\boldsymbol{Q},t)$ in the time dependent

Schrödinger equation by the expression in Eq. (2.45). The MCTDH working equations are coupled time derivative equations of $\{A_{\nu_1,\cdots,\nu_N}\}$ and $\{\varphi^{(j)}_{\nu_j}(Q_j,t)\}$ which can be solved by varies numerical integration methods.

The propagation of a MCTDH type of wave packet is quite efficient provided the Hamiltonian is a sum of products of single particle operators. The kinetic energy part of the Hamiltonian is automatically a sum of products as can be seen in Section 2.2. To efficiently exploit MCTDH we have to fit the PES into a sum of products. Concerning available PES with sufficient accuracy, up to now the highest dimensional one is 15D as reported by Bowman group [92] for the Zundel cation $H^+\cdot(H_2O)_2$. They have used least square fitting with 7962 basis functions. This seven atom case reaches the limits of both the fitting and the quantum chemistry capability of present computers. Apart from the most simple least square fitting, a more applicable fitting scheme especially for medium high dimension has been proposed in Ref. [93]. Combining the expansion technique introduced in Section 2.3.1 and a proper fitting method one can generate high dimensional PES with sufficient accuracy.

2.4.2 Calculation of Stationary Eigenstates

The relaxation method [94] is a quite general method to generate especially the ground state wave function. The basic idea is to propagate in imaginary time domain $t = -i\tau$ to decrease the energy of an initial guess wave packet to approach the ground state energy. In this case the solution in Eq. (2.44) becomes

$$\Psi(\boldsymbol{Q},t) = \sum_n c_n e^{-E_n\tau/\hbar}\Psi_n(\boldsymbol{Q}). \tag{2.46}$$

The above equation shows that the components of each eigenstate decay exponentially at a rate proportional to the corresponding eigenvalue, i.e., all the other eigenstates decay faster than the ground state. If we simply normalize the wave function after each propagation time step we can get the ground state wave function when the propagation is sufficiently long, i.e., the components of all the other eigenstates decay to zero.

Basically following the same idea we can get the first excited state provided we first project out the ground state from the Hilbert space, i.e., $\Psi(\boldsymbol{Q},t=0)$ replaced by $(1-\hat{P}_0)\Psi(\boldsymbol{Q},t=0)$ and H replaced by $(1-\hat{P}_0)H(1-\hat{P}_0)$ with $\hat{P}_0 = |\Psi_0\rangle\langle\Psi_0|$. However to obtain the n-th excited states we have to calculate all the $n-1$ lower energy excited states. In MCTDH the ground state is obtained by relaxation while the excited states are obtained by so called improved relaxation [95].

The improved relaxation starts from an initial state close to the desired excited state and the iteration procedure is described as follows:

1. Initial guess of SPFs $\{\varphi_{\nu_j}^{(j)}(Q_j, t=0)\}$
2. Use the basis set of $\{\Phi_J = \varphi_{\nu_1}^{(1)}(Q_1, t=0)\cdots\varphi_{\nu_N}^{(N)}(Q_N, t=0)\}$ to generate the Hamiltonian matrix $H_{JK} = \langle\Phi_J|H|\Phi_K\rangle$
3. Diagonalize the Hamiltonian matrix, get the eigenvector $\{A_J\}$ which corresponds to the desired excited state
4. The approximated wave function is $\Psi = \sum_J A_J\Phi_J$ which determines the equation of motion of SPFs $\{\varphi_{\nu_j}^{(j)}(Q_j, t)\}$
5. Propagate $\{\varphi_{\nu_j}^{(j)}(Q_j, t=0)\}$ in imaginary time to generate new single particle function $\{\varphi_{\nu_j}^{(j)}(Q_j, t=\Delta t)\}$
6. Go to step 2 until convergence

Different from a MCTDH wave packet propagation, where both $\{\Phi_J\}$ and $\{A_J\}$ are obtained by integrating corresponding time derivative equations, improved relaxation obtains $\{A_J\}$ by diagonalizing the Hamiltonian matrix under the basis set of $\{\Phi_J\}$. It has been shown that this method converges to the eigenstates that correspond to the variational principle applied to the MCTDH ansatz for the wave function [95].

2.5 Summary

In this chapter a concise method for generating vibrational Hamiltonian is described in detail which is the fundamental starting point for numerical simulations of the coming chapters. In addition we have also briefly reviewed the efficient MCTDH package [91] for solving multidimensional Schrödinger equations. The Hamiltonian can be constructed in terms of arbitrary coordinates which enables us to use coordinates most suitable for the natural motions of a molecule. In particular, it is a quite appropriate level of theory for strong hydrogen bonded systems since multidimensional large amplitude coordinates are treated efficiently. In Chapter 3 and 4 the applications of the method mentioned above to strong hydrogen bonded systems for multi- or full- dimensional quantum simulations will be performed.

Chapter 3

Models of Hydrogen Bonds in Protonated Ammonia Clusters

3.1 Introduction

Recent experiment of ammonia transporter proteins [47] implies that hydrogen bonding and transfer in protonated ammonia cluster cations, $NH_4^+(NH_3)_n$ as shown in Fig. 3.1, may play an important role in nitrogen metabolism. Direct hydrogen atom transfer along ammonia wires [48] has also been observed which in turn triggers the study of direct proton conduction. To fully interpret the fundamental processes involving these cations requires extensive investigations at the molecular level. However, the previous investigations, no matter experimental or theoretical ones, capture little essence concerning the HB dynamics. As outlined in the introduction, IR spectroscopy can give valuable information on the properties of HBs.

In the following Section 3.2 we provide a multidimensional quantum simulation for $N_2H_7^+$ focusing on the IR characteristics of the HB. A reduced 6D Hamiltonian is generated and solved by the method introduced in Chapter 2. We further compare our theoretical results of the geometry and IR spectrum with some previous investigations as well as a very recent IR spectrum below 2000 cm^{-1} measured by Asmis and coworkers [96, 97]. In Section 3.3 the larger clusters ($n = 2 - 4$) are investigated. We have studied the potential curves along the proton transfer coordinate to rationalize the validity of harmonic predictions and compared the harmonic IR spectra with experiment.

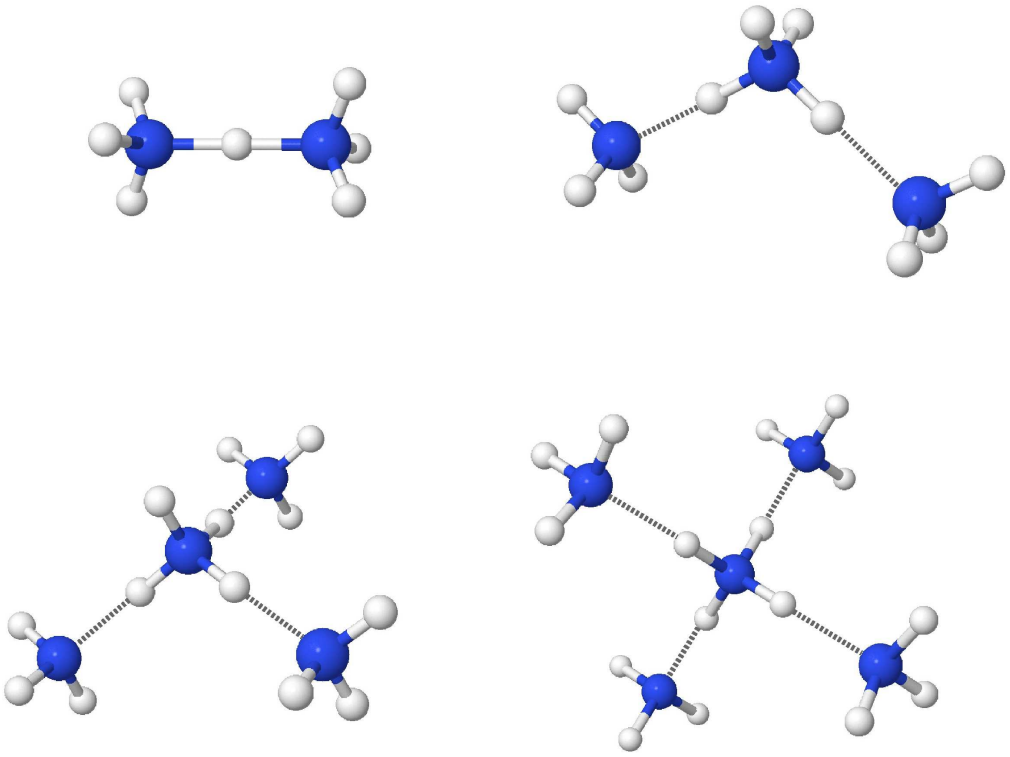

Figure 3.1: Equilibrium configurations of the protonated ammonia clusters $NH_4^+(NH_3)_n$ as obtained using MP2/aug-cc-pVTZ* ($n = 1$) and MP2/6-311+G(d,p) ($n = 2 - 4$) optimization. In this chapter when we say MP2/aug-cc-pVTZ it actually means the MP2 level of theory with the aug-cc-pVTZ and cc-pVTZ basis set for N and H, respectively.

3.2 Geometry and IR Spectrum of $N_2H_7^+$

We first focus on the protonated ammonia dimer $N_2H_7^+$. Using quantum chemistry optimization, which treats all the nuclei classically, the two most important equilibrium configurations shown in Fig. 3.2 are obtained with Gaussian03 [62] program. The minimum configuration has C_{3v} symmetry with the proton located asymmetrically with respect to the two terminal ammonia groups while the transition state has D_{3d} symmetry with the proton exactly in the center. The central proton can transfer between two equivalent minimum configurations via a transition state by overcoming the potential barrier which is characterized by the energy difference of the minimum and transition state configurations if one ignore the zero point energy (ZPE) correction. The barrier height at the MP2/aug-cc-pVTZ level of theory is 267 cm^{-1} and increases to 353 cm^{-1} if we apply the CCSD(T)/aug-cc-pVTZ method to the MP2 geometries. The barrier is quite shallow due to strong hydrogen bonding no matter which level of quantum chemistry method is concerned. Such a low barrier means a rapid proton translocation between two equivalent

minima.

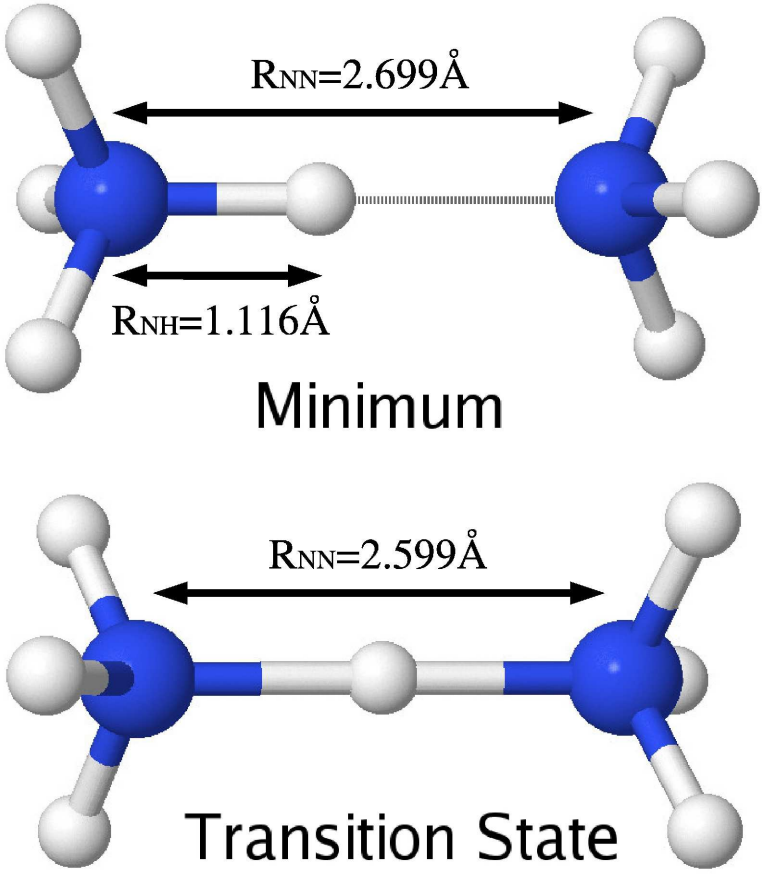

Figure 3.2: Minimum and transition state configurations of $N_2H_7^+$ obtained by MP2/aug-cc-pVTZ level of theory.

However, conflicting with the classical minimum, the IR spectroscopy experiment in the 2600-4000 cm^{-1} range by Lee and coworkers [49] leads to the conclusion that $N_2H_7^+$ should have D_{3h} symmetry. This point is also studied quantum mechanically by a one-dimensional model in Ref. [98]. Concerning the IR spectrum, recent experiments find rich vibrational bands while the harmonic approximation predicts nothing in the region from 500 cm^{-1} to 1100 cm^{-1} irrespective of the reference geometry, i.e., minimum or transition state configuration. Therefore only a theoretical investigation beyond the harmonic approximation is expected to provide reasonable assignments. As has been pointed out in Chapter 1, multidimensional quantum simulation is the most appropriate level of theory to investigate this kind of strong hydrogen bonded systems especially concerning the dynamics of HBs.

3.2.1 Reduced Dimensional Hamiltonian Operator for $N_2H_7^+$

In the following we will provide a reduced dimensional model Hamiltonian for the $N_2H_7^+$ cation which is based on internal coordinates. Consisting of 9 atoms, $N_2H_7^+$ in principle has 21 internal coordinates to compose the full dimensional Hamiltonian for the total angular momentum $J^2 = 0$. Focusing on that part of the spectrum which is influenced by the shared proton motion, one can adopt a reduction by taking into account the following two conditions: (i) experimental data suggest that the relevant energy range is presumably below 1000 cm^{-1}, but might extend into the < 1500 cm^{-1} range due to combination bands and (ii) symmetry selection rules dominate the anharmonic couplings especially in this low-energy range.

We first assume that the C_3 symmetry of the N_2H_6 fragment, i.e., excluding the central proton, will not be broken. Second, the length of the N-H covalent bonds shall be fixed. These constraints leave seven internal coordinates to describe the system as shown in Fig. 3.3, i.e., the shared proton stretching and bending with respect to the center of mass of the rest N_2H_6 fragment, z, x, and y, the relative motion of the centers of mass of the two ammonia, R, the umbrella type motion of the two ammonia, θ_1 and θ_2, and the rotation (torsion) of the NH_3 fragments with respect to each other, φ. Note θ_1 or θ_2 characterizes the simultaneous equal-amplitude-wags of the three NH bonds which always keep the C_3 symmetry of the N_2H_6 fragment. The details are visualized in Fig. 3.4.

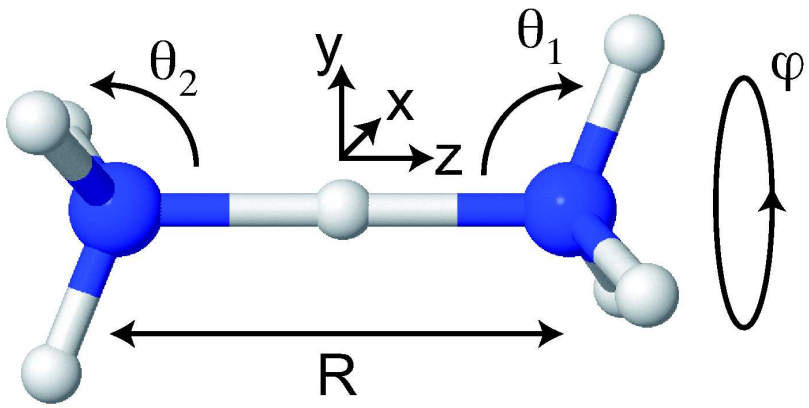

Figure 3.3: Definition of the seven active coordinates of the reduced $N_2H_7^+$ model. The origin of the MRF is the center of mass and the z axis is along the N$\cdots$N line.

To setup the Hamiltonian for this 7D model we first generate the KEO exploiting the approach detailed in Chapter 2. For the seven active coordinates in Fig. 3.3 the classical kinetic energy with all other internal coordinates frozen can be obtained by exploiting

Eq. (2.18) repeatedly

$$
\begin{aligned}
T &= T_H^{(H)} + T_{N_2H_6}^{(N_2H_6)} + T_{(H)}^{(N_2H_6)} = T_{N_2H_6}^{(N_2H_6)} + T_{(H)}^{(N_2H_6)} \\
T_{N_2H_6}^{(N_2H_6)} &= T_{NH_3}^{(NH_3)} + T_{N'H_3'}^{(N'H_3')} + T_{(NH_3)}^{(N'H_3')} \\
T_{NH_3}^{(NH_3)} &= T_{H_3}^{(H_3)} + T_N^{(N)} + T_{(N)}^{(H_3)} = T_{H_3}^{(H_3)} + T_{(N)}^{(H_3)},
\end{aligned}
$$

where (AB) is the center of mass of AB and the equivalent atoms are simply distinguished by the prime symbol. Combining the above three equations we finally get the classical kinetic energy in terms of sub-systems

$$
T = T_{(H)}^{(N_2H_6)} + T_{(NH_3)}^{(N'H_3')} + \left(T_{H_3}^{(H_3)} + T_{(N)}^{(H_3)}\right) + \left(T_{H_3'}^{(H_3')} + T_{(N')}^{(H_3')}\right) \tag{3.1}
$$

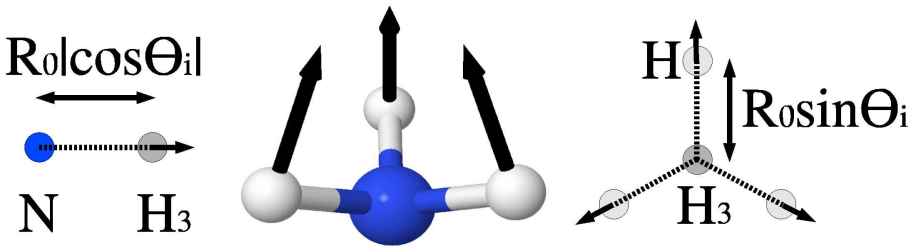

Figure 3.4: Schematic view to construct the classical kinetic energy of NH_3 fragment. The notation H_3 means the center of mass of the three H atoms. Left: direction of C_3 axis (z axis). Center: Motion of NH_3 fragment (rotation is not shown). Right: Plane of the three H atoms.

Consider the three Euler angles which connect the LRF and the MRF $\{\vartheta, \phi, \chi\}$ according to Appendix A, where ϑ and ϕ are defined as the two direction angles of the MRF z axis in the LRF. We will obtain each term in Eq. (3.1) in the following. The kinetic energy of the central proton with respect to the center of mass of the N_2H_6 fragment reads (note x, y, and z are MRF coordinates)

$$
T_{(H)}^{(N_2H_6)} = \frac{1}{2}\mu_p \dot{z}^2 + \frac{1}{2}\mu_p \dot{x}^2 + \frac{1}{2}\mu_p \dot{y}^2 + T_p(\dot{\vartheta}, \dot{\phi}, \dot{\chi}),
$$

where $\mu_p = \frac{2m_H(3m_H+m_N)}{7m_H+2m_N}$. According to Eq. (2.30) $T_{(H)}^{(N_2H_6)}$ should includes four parts, of which three involve the MRF rotational velocities and the other one is the kinetic energy measured in the MRF. The three rotation related parts include the Coriolis type couplings and rotational energy. These terms are simply denoted by $T_p(\dot{\vartheta}, \dot{\phi}, \dot{\chi})$ here and they are very small in the case when the total angular momentum is zero. The two relative motions $NH_3 \cdots NH_3$ and $N \cdots H_3$ are along the z axis of the MRF which can be described by spherical coordinates in the LRF according to the definition of the MRF in Appendix A.

According to Fig. 3.3 and Fig. 3.4 we have the following kinetic energy

$$T_{(NH_3)}^{(NH_3)} = \frac{1}{2}\mu_R\dot{R}^2 + \frac{1}{2}\mu_R R^2\left(\dot{\vartheta}^2 + \dot{\phi}^2\sin^2\vartheta\right)$$
$$T_{(N)}^{(H_3)} = \frac{1}{2}\mu_{(N-3H)}\left(\frac{d(R_0\cos\theta_i)}{dt}\right)^2 + \frac{1}{2}\mu_{(N-3H)}(R_0\cos\theta_i)^2\left(\dot{\vartheta}^2 + \dot{\phi}^2\sin^2\vartheta\right),$$

where $\mu_R = \frac{1}{2}(3m_H + m_N)$, $\mu_{(N-3H)} = 3m_H m_N/(3m_H + m_N)$, and $R_0 = 1.017\mathring{A}$ is the free N-H covalent bond length calculated at the MP2/aug-cc-pVTZ level of theory. The term $T_{H_3}^{(H_3)}$ characterizes the three hydrogen atoms motion in their center of mass reference frame. According to the right panel of Fig. 3.4 we have

$$T_{H_3}^{(H_3)} = 3\cdot\frac{1}{2}m_H\left(\frac{d(R_0\sin\theta_i)}{dt}\right)^2 + 3\cdot\frac{1}{2}m_H(R_0\sin\theta_i)^2\dot{\varphi}_i^2 + \frac{1}{2}I_\vartheta\dot{\vartheta}^2 + \frac{1}{2}I_\phi\dot{\phi}^2,$$

where the last two terms characterize the rotational energy which are unnecessary to be written in detail as will be seen in the following. Due to the C_{3v} symmetry the Coriolis type couplings are canceled with each other. The orientation angle of each individual ammonia is denoted by $\varphi_{1,2}$ and only the difference between them is the torsion shown in Fig. 3.3. Their linear combination which characterize the rotation of the N_2H_6 fragment will be defined as the third Euler angle χ in the following.

For an isolated system, apart from the translation of the center of mass which can be separated, the global rotation can be characterized by pure numbers since $[\hat{J}^2, \hat{H}] = 0$ and their common eigenstates can be classified by the eigenvalues of $\hat{J}^2$. As discussed in Section 2.2.5, we will only study the vibrations for the total angular momentum $\boldsymbol{J} = 0$. In the following we assume $T_p(\dot{\vartheta}, \dot{\phi}, \dot{\chi}) = 0$ for $\boldsymbol{J} = 0$. This approximation is equivalent to neglecting the coupling of the angular momenta of the central proton and the N_2H_6 fragment for $\boldsymbol{J} = 0$. According to Section 2.2.5 we have $\boldsymbol{J} = \frac{\partial T}{\partial \dot{\boldsymbol{Q}}_{rot}}$, where $\boldsymbol{Q}_{rot}^T = (\ \vartheta \quad \phi \quad \chi\ )$. With the help of this relation we can immediately see that $\boldsymbol{J} = 0$ is equivalent to $\dot{\vartheta} = \dot{\phi} = \dot{\chi} = 0$ for $T_p(\dot{\vartheta}, \dot{\phi}, \dot{\chi}) = 0$.

After applying the condition $\dot{\vartheta} = \dot{\phi} = 0$ we simplify the kinetic energy as

$$\begin{aligned} T &= \frac{1}{2}\mu_p\dot{z}^2 + \frac{1}{2}\mu_p\dot{x}^2 + \frac{1}{2}\mu_p\dot{y}^2 + \mu_R\dot{R}^2 + \frac{3m_H m_N}{2(3m_H + m_N)}R_0^2\left(\dot{\theta}_1^2\sin^2\theta_1 + \dot{\theta}_2^2\sin^2\theta_2\right) \\ &\quad + \frac{3}{2}m_H R_0^2\sum_{i=1,2}(\dot{\theta}_i^2\cos^2\theta_i + \dot{\varphi}_i^2\sin^2\theta_i) \\ &= \frac{1}{2}\mu_p\dot{z}^2 + \frac{1}{2}\mu_p\dot{x}^2 + \frac{1}{2}\mu_p\dot{y}^2 + \frac{1}{2}\mu_R\dot{R}^2 + \frac{1}{2}I_{vib}(\theta_1)\dot{\theta}_1^2 + \frac{1}{2}I_{vib}(\theta_2)\dot{\theta}_2^2 \\ &\quad + \frac{1}{2}I_{rot}(\theta_1)\dot{\varphi}_1^2 + \frac{1}{2}I_{rot}(\theta_2)\dot{\varphi}_2^2, \end{aligned} \tag{3.2}$$

where $I_{vib}(\theta) = I_0(\cos^2\theta + \frac{m_N}{3m_H+m_N}\sin^2\theta)$, $I_{rot}(\theta) = I_0\sin^2\theta$, and $I_0 = 3m_H R_0^2$. Exploiting the relative rotation (torsion) $\varphi = \varphi_2 - \varphi_1$ and the global rotation $\chi =$

$(I_{rot}(\theta_1)\varphi_1 + I_{rot}(\theta_2)\varphi_2) \,/\, (I_{rot}(\theta_1) + I_{rot}(\theta_2))$ as new variables we can rewrite the kinetic energy. Apply the condition $\dot{\chi} = 0$ and we finally get the kinetic energy for $\boldsymbol{J} = 0$

$$\begin{aligned} T &= \frac{1}{2}\mu_p \dot{z}^2 + \frac{1}{2}\mu_p \dot{x}^2 + \frac{1}{2}\mu_p \dot{y}^2 + \frac{1}{2}\mu_R \dot{R}^2 \\ &\quad + \frac{1}{2} I_{vib}(\theta_1) \dot{\theta_1}^2 + \frac{1}{2} I_{vib}(\theta_2) \dot{\theta_2}^2 + \frac{1}{2} I_{tor}(\theta_1, \theta_2) \dot{\varphi}^2, \end{aligned} \tag{3.3}$$

where the reduced moment of inertia for the torsion is $I_{tor}(\theta_1, \theta_2) = I_{rot}(\theta_1) * I_{rot}(\theta_2)/(I_{rot}(\theta_1) + I_{rot}(\theta_2))$. According to the general procedure detailed in Section 2.2.1 we can obtain the following quantum KEO

$$\begin{aligned} \hat{T} &= \frac{1}{2\mu_p} \hat{P_z}^\dagger \hat{P_z} + \frac{1}{2\mu_p} \hat{P_x}^\dagger \hat{P_x} + \frac{1}{2\mu_p} \hat{P_y}^\dagger \hat{P_y} + \frac{1}{2\mu_R} \hat{P_R}^\dagger \hat{P_R} \\ &\quad + \frac{1}{2} \hat{P_{\theta_1}}^\dagger I_{vib}(\theta_1)^{-1} \hat{P_{\theta_1}} + \frac{1}{2} \hat{P_{\theta_2}}^\dagger I_{vib}(\theta_2)^{-1} \hat{P_{\theta_2}} + \frac{\hat{P_\varphi}^\dagger \hat{P_\varphi}}{2 I_{tor}(\theta_1, \theta_2)}. \end{aligned} \tag{3.4}$$

Now check the seven coordinates we adopted. Three of them are Cartesian and the rest four are spherical coordinates defined in the MRF. According to Section 2.2.4 we can write out the HCMOs

$$\begin{aligned} \hat{P_\alpha}^\dagger &= \hat{P_\alpha}, \alpha = x, y, z \\ \hat{P_R}^\dagger &= \hat{P_R} - \frac{2i\hbar}{R} \\ \hat{P_{\theta_j}}^\dagger &= \hat{P_{\theta_j}} - i\hbar \mathrm{cot}\theta_j, j = 1, 2 \\ \hat{P_\varphi}^\dagger &= \hat{P_\varphi}. \end{aligned} \tag{3.5}$$

The final KEO together with the Euclidean normalization condition are given as follows

$$\begin{aligned} T &= -\frac{\hbar^2}{2\mu_p}\left(\frac{\partial^2}{\partial x^2} + \frac{\partial^2}{\partial y^2} + \frac{\partial^2}{\partial z^2}\right) - \frac{\hbar^2}{2\mu_R} \frac{1}{R^2} \frac{\partial}{\partial R} R^2 \frac{\partial}{\partial R} \\ &\quad - \frac{\hbar^2}{2 I_{tor}(\theta_1, \theta_2)} \frac{\partial^2}{\partial \varphi^2} - \frac{\hbar^2}{2} \sum_{i=1,2} \frac{1}{\sin\theta_i} \frac{\partial}{\partial \theta_i} \frac{\sin\theta_i}{I_{vib}(\theta_i)} \frac{\partial}{\partial \theta_i} \\ d\tau &= R^2 \sin\theta_1 \sin\theta_2 dx dy dz dR d\theta_1 d\theta_2 d\varphi. \end{aligned} \tag{3.6}$$

The torsion angle φ of the two NH_3 fragments can be separated from the other six variables if the potential energy does not depend on it. We have confirmed that the ab initio potential energy surface depends only very weakly on this angle (the barrier is as low as 12 cm^{-1} based on an MP2/aug-cc-pVTZ level of investigation). Moreover, there is a clear separation between the rotational and vibrational excitation energies. The former is only several cm^{-1} while the latter is several hundred cm^{-1} . Thus, we can separate this torsion and replace the operator $-\frac{\partial^2}{\partial \varphi^2}$ by its expectation value, say, K^2.

For the numerical implementation below it is more convenient to use another set of coordinates and a new gauge of wave function which simplify both the kinetic energy operator and the normalization volume element. Assuming $K^2 = 0$ we will use the following six-dimensional (6D) kinetic energy operator

$$T = -\frac{\hbar^2}{2\mu_p}\left(\frac{\partial^2}{\partial x^2}+\frac{\partial^2}{\partial y^2}+\frac{\partial^2}{\partial z^2}\right) - \frac{\hbar^2}{2\mu_R}\frac{\partial^2}{\partial R^2} - \frac{\hbar^2}{2I_0}\sum_{i=1,2}\frac{\partial}{\partial u_i}g(u_i)\frac{\partial}{\partial u_i}, \tag{3.7a}$$

$$d\tau = dxdydzdRdu_1du_2,, \tag{3.7b}$$

where $u_i = \cos\theta_i$ and $g(u) = (1-u^2)(3m_H+m_N)/(3m_Hu^2+m_N)$. The relation between the new and old wavefunctions is $\Phi = R\Psi$, i.e., in terms of the new wavefunction and coordinates the 1D reduced densities are simply $\rho(R) = |\Phi(R)|^2$ and $\rho(u_i) = |\Phi(u_i)|^2$, while in terms of the old ones they are $\rho(R) = |R\Psi(R)|^2$ and $\rho(\theta_i) = \sin\theta_i|\Psi(\theta_i)|^2$. This criteria, density is just absolute square of wavefunction, can be generalized to other kind of coordinate or gauge transformations for simplification.

According to Eq. (2.38) the corresponding 6D PES can be constructed by cumulative expansion in terms of different correlation orders

$$\begin{aligned} V(\boldsymbol{Q}) &= V(\boldsymbol{Q}_0) + \sum_i V^{(1)}(Q_i) + \sum_{i<j} V^{(2)}(Q_i,Q_j) \\ &\quad + \sum_{i<j<k} V^{(3)}(Q_i,Q_j,Q_k) + \ldots, \end{aligned} \tag{3.8}$$

where $\boldsymbol{Q}$ is a vector comprising the six model coordinates appearing in Eq. (3.7a) and $V^{(n)}$ is the n-mode correlation potential energy. The reference configuration $\boldsymbol{Q}_0$ for expansion is the transition state as shown in Fig. 3.2. Our final expansion includes all the two-mode correlations as well as those three-mode correlations concerning the z coordinate except $V^{(3)}(z,u_1,u_2)$ and $V^{(3)}(z,R,u_{1,2})$ which are assumed to be negligible as compared with the those involving two proton coordinates like $V^{(3)}(z,x,R)$.

3.2.2 Numerical Implementation

The required PESs are calculated using the MP2/aug-cc-pVTZ level of theory [62] to generate the 6D PES. According to Eq. (3.8) the numbers of 1D, 2D and 3D PESs are $\binom{6}{1} = 6$, $\binom{6}{2} = 15$ and $\binom{6}{3} = 20$, respectively. We can make use of the symmetry operations to decrease the calculation effort. The first symmetry is system inversion $V(-z,R,\theta_1,\theta_2,-x,-y) = V(z,R,\theta_2,\theta_1,x,y)$ which ensure us to generate low dimensional PESs of θ_1/θ_2 from θ_2/θ_1. The second symmetry is that the permutation of the two bending modes x and y, i.e., the two modes are equivalent since the slight difference

caused by torsion has been ignored. By considering the symmetry the corresponding numbers of PESs which we need to scan are $\left(\begin{array}{c}4\\1\end{array}\right)=4$, $\left(\begin{array}{c}4\\2\end{array}\right)+\left(\begin{array}{c}2\\2\end{array}\right)+\left(\begin{array}{c}2\\2\end{array}\right)=8$ and $\left(\begin{array}{c}4\\3\end{array}\right)+\left(\begin{array}{c}2\\2\end{array}\right)\left(\begin{array}{c}3\\1\end{array}\right)+\left(\begin{array}{c}2\\2\end{array}\right)\left(\begin{array}{c}3\\1\end{array}\right)=10$. As mentioned above concerning three-mode correlations we are only interested in those involving z with relatively strong couplings. The actual numbers of 1D, 2D and 3D PESs we finally scanned are 4, 8 and 3 which produce 6, 15 and 7 ones after applying symmetry. The selected 3D PESs for scanning are $V(z,x,y)$, $V(z,x,R)$, and $V(z,x,\theta_1)$ which can generate $V(z,y,R)$, $V(z,x,\theta_2)$, $V(z,y,\theta_1)$, and $V(z,y,\theta_2)$. For each PES scan we use the bond lengths and bond angles as variables. In total about 10000 points have been calculated and applying symmetry we obtain more than 90000 points spanning the energy range up to 10000 cm^{-1}. These PESs has been subsequently fitted to a polynomial of up to 10th order by the fitting method introduced in Section 2.3.2 with fitting error less than one percent.

For the solution of the nuclear Schrödinger equation we use the MCTDH approach as detailed in Chapter 2. The wave function is represented on the primitive grid using a harmonic oscillator DVR. The details about the basis set for MCTDH are shown in Table 3.1. The MCTDH equations of motion have been solved using the Adams-Bashforth-

Table 3.1: MCTDH parameters for solving Schrödinger equation (lengths in Å). N_{DVR}: number of DVR points; N_{SPF}: number of SPFs.

mode	z	R	u_1	u_2	x	y
min. grid	-0.58	2.20	-0.61	-0.61	-0.53	-0.53
max. grid	0.58	3.26	0.13	0.13	0.53	0.53
N_{DVR}	59	39	39	39	39	39
N_{SPF}	9	8	9		3	

Moulton predictor-corrector integrator of 6th order [90]. We have calculated low lying excited state by diagonalizing the Hamiltonian with the Lanczos iteration algorithm as implemented in the MCTDH program package. The wave functions which serve for the assignment of the spectrum have been obtained using the improved relaxation method [95] introduced in Section 2.4.2. The assignment below will be based on variables quite close to certain normal modes, i.e.,

$$\langle zR\theta_s\theta_a xy|mnklij\rangle = \Psi_{mnklij}(z,R,\theta_s,\theta_a,x,y) \tag{3.9}$$

where m, n,k,l,i and j are quantum numbers associated with z,R, $\theta_s = \frac{\theta_1+\theta_2}{2}$,$\theta_a = \frac{\theta_1-\theta_2}{2}$,$x$, and y respectively.

3.2.3 Geometry and Eigenstates

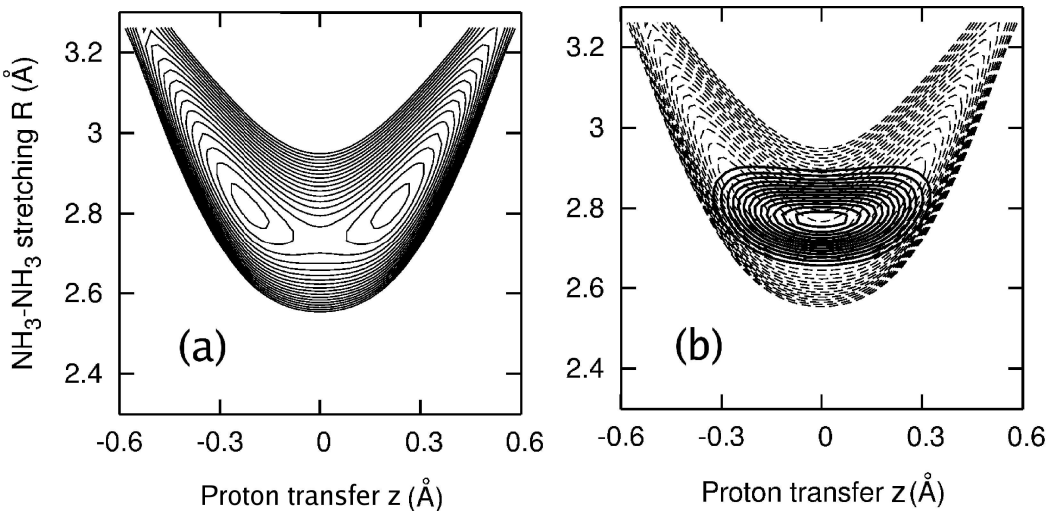

Figure 3.5: (a) 2D cut of the 6D PES, contour levels from -150 to 1550 cm^{-1} in steps of 100 cm^{-1} . (b) 2D reduced probability density (solid line) of the ground state.

In Fig. 3.5(a) we show a two-dimensional cut of the 6D PES along the proton transfer coordinate z and the NH_3-NH_3 stretching coordinate R with other coordinates fixed at transition state, i.e., $\theta_1 = \theta_2 = 111.7°$ and $x = y = 0$ at the current level of quantum chemistry. The shape of the PES resembles what one would expect for symmetric medium to weak HBs, i.e., a double minimum with a transition state at a compressed NH_3-NH_3 distance [34]. The minima and transition state correspond to ($z = \pm 0.24$Å, $R = 2.833$Å) and ($z = 0$,$R = 2.733$Å), respectively, similar to what has been reported for a 6-311++G(d,p) basis set in Ref. [98].

Calculating the 6D vibrational ground state yields the probability density. The 2D reduced probability density concerning the proton transfer and the NH_3-NH_3 stretching coordinates is shown in Fig. 3.5(b). The most notable feature is that this function has a single maximum at the symmetric configuration. In other words, as compared to the barrier height, the quantum mechanical ZPE related to the proton transfer mode is large enough to *symmetrize* the hydrogen bond. This feature agrees well with the experiment in the context of IR spectroscopy in the 2600-4000 cm^{-1} range in Ref. [49].

An interesting case may occur upon deuteration when the ZPE locates below the reaction barrier and the central deuteron distribution becomes bimodal. Taking the transition state energy as reference, the total ZPE of $N_2H_7^+$ and $N_2D_7^+$ are 3355 cm^{-1} and 2323

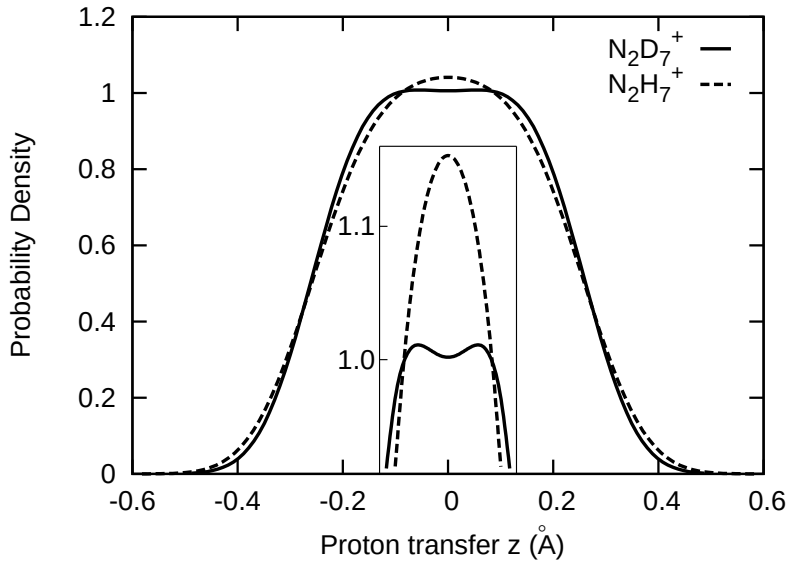

Figure 3.6: The 1D reduced probability density along the shared proton/deuteron transfer coordinate z for the $N_2H_7^+/N_2D_7^+$. The central inset shows the details of the bimodal characteristics with the vertical axis in a different scale.

cm^{-1}, respectively. We have also investigated the fully deuterated isotopomer $N_2D_7^+$, and the ground state distribution along the deuteron transfer coordinate z is shown in Fig. 3.6 with comparison to the $N_2H_7^+$ case. From the slightly bimodal deuteron distribution of the $N_2D_7^+$ we can imagine the ZPE associated to the deuteron transfer mode slightly goes below the reaction barrier leading to an essential difference from the $N_2H_7^+$ case. To clearly show this point we provide an enlarged view in the central inset for the related area distribution. The bimodal deuteron distribution agrees well with a very recent work based on path integral molecular dynamics simulation [99].

Table 3.2: Ground state mean values and variances of each coordinates for $N_2H_7^+$ with lengths in Å and angles in degree. For comparison we report the variance of $u_i = \cos\theta_i$ instead of θ_i.

coordinates	z	R	θ_1	θ_2	x	y
mean value	0	2.796	111.576	111.576	0	0
variance	0.174	0.067	0.066	0.066	0.106	0.106

To get an even better picture of the ground state geometry we can study the mean value and variance of each coordinate as shown in Table 3.2. The quantum ground state

has the same D_{3d} symmetry as the classical transition state. From the variances we can see the proton stretching motion has the largest amplitude and the bending follows. The strong hydrogen bond makes the proton distribution highly delocalized. Due to the large amplitude zero point vibration of the central proton the NH_3-NH_3 distance increases as compared to the transition state. This is typical for strong hydrogen bonded systems [45, 100].

Usually the N$\cdots$N distance is investigated to reflect the hydrogen bonding strength as well as some other geometrical effects. It has been pointed out that in the A–H$\cdots$B type HB there exists an empirical correlation between the A–H and H$\cdots$B distances irrespective of the A–H$\cdots$B angle [57, 101, 102, 103]. This correlation may provide us with some rough picture of the geometric changes of the real time hydrogen transfer dynamics. On the other hand, we may use just one variable to describe stationary HB geometry, which actually reflects the bond strength. A typical geometric correlation for N–H$\cdots$N type hydrogen bonded systems established by Limbach and coworkers is shown in Fig. 3.7. In this figure the proton displacement from the bonding center is characterized by q_1 and the N$\cdots$N distance is q_2. Experimentally the proton displacement q_1 can be obtained based on NMR measurement of the chemical shift. Combined with low temperature neutron diffraction data one can establish the empirical correlation curve for the N–H$\cdots$N type HBs.

In our case z and R_{NN} are just q_1 and q_2 in the figure since the mean values of x and y are both zero. The variable R we adopted in the numerical simulation is not equal to R_{NN}, therefore we have generated the corresponding operator for R_{NN} in terms of the model coordinates

$$\hat{R}_{\mathrm{N-N}} = R + \eta R_0(u_1 + u_2), \tag{3.10}$$

where $\eta = 3m_H/(3m_H + m_N)$. It is straightforward to calculate the mean value of the N$\cdots$N distance at ground state with the operator $\hat{R}_{\mathrm{N-N}}$ and the ground state wavefunction. This mean value is found to be $R_{NN} = 2.6631$Å which agrees well with the figure, giving support for the empirical correlation curve by Limbach and coworkers.

Apart from the ground state, some typical excited states are also calculated not only to assign the IR spectrum but also to provide an essential grasp of how the final states for the fundamental and combination transitions look like. The reduced probability densities of these excited states are shown in Fig. 3.8. The fundamental transitions of the proton transfer mode z, NH_3-NH_3 stretching mode R, asymmetric umbrella mode θ_a and proton bending mode x are labeled as $|100000\rangle$, $|010000\rangle$, $|000100\rangle$ and $|000010\rangle$, respectively. For fundamental transitions there is only one nodal plane along to the corresponding mode. The nodal plane is simply defined by the corresponding coordinate

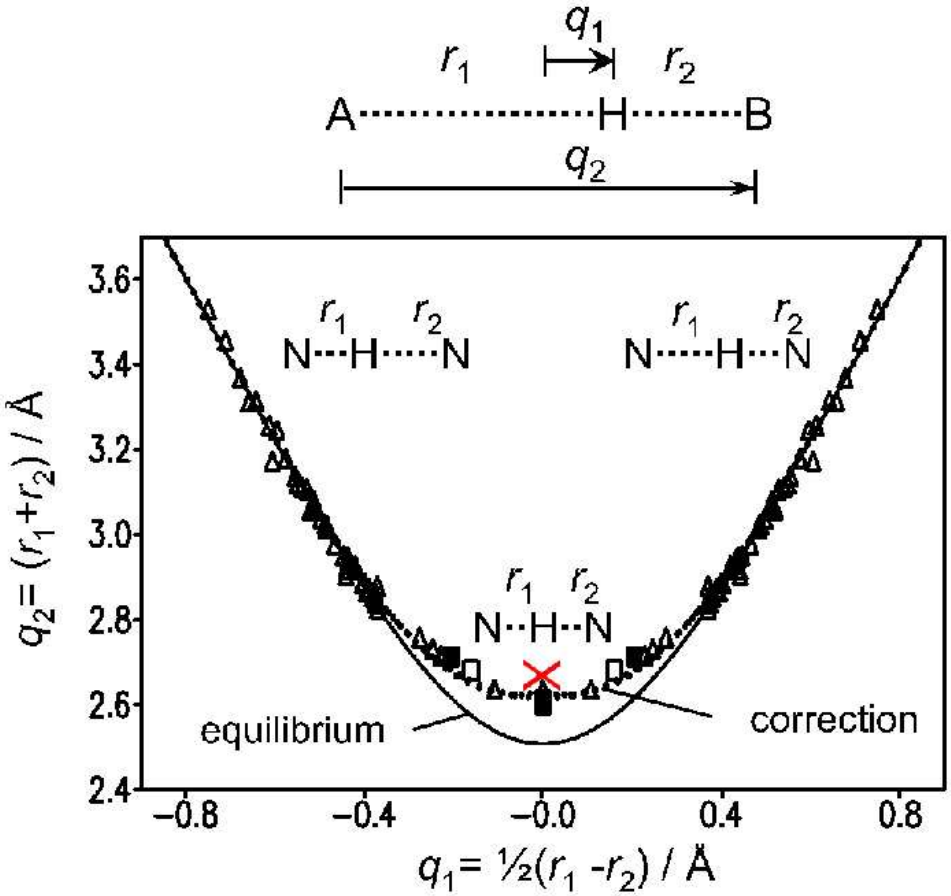

Figure 3.7: Correlation between HB length $q_2 = r_1 + r_2$ and hydrogen transfer coordinate $q_1 = (r_1 - r_2)/2$ adapted from Ref. [57]. The solid line is calculated by a classical relation on valence bond orders pointed out by Pauling and the dotted line is an empirical correlation based on experimental HB geometries established by low temperature neutron diffraction and NMR data. In the empirical curve Limbach and coworkers have taken into account the correction caused by zero point vibration. The red cross is the calculated value by 6D quantum simulation.

equal to zero (e.g., $z = 0$, $\theta_a = 0$ and $x = 0$) or its equilibrium value (e.g. $R = R_{eq}$). The fundamental transitions of the symmetric umbrella mode θ_s and proton bending y, which are not shown in the figure, are similar to that of θ_a and x except for the nodal plane is defined by $\theta_s = \theta_{eq} = 111.6°$ and $y = 0$, respectively. In other words, the corresponding reduced densities can be obtained by a simple rotation of 90 degrees from those of θ_a and x shown in Fig. 3.8 since we have ignored the slight difference caused by torsion. Some combinations of z and R are also listed in Fig. 3.8 as $|110000\rangle$ and $|120000\rangle$ which clearly shows the characters of this kind of combinations $|mn0000\rangle$. Combinations between other modes have much higher excitation energies than those we are interested

in, therefore they are not covered by our investigation. The excited state wave functions provide us a quite clear picture of assignment of each vibrational band as obtained by IR spectroscopy. We can see more details in the next section.

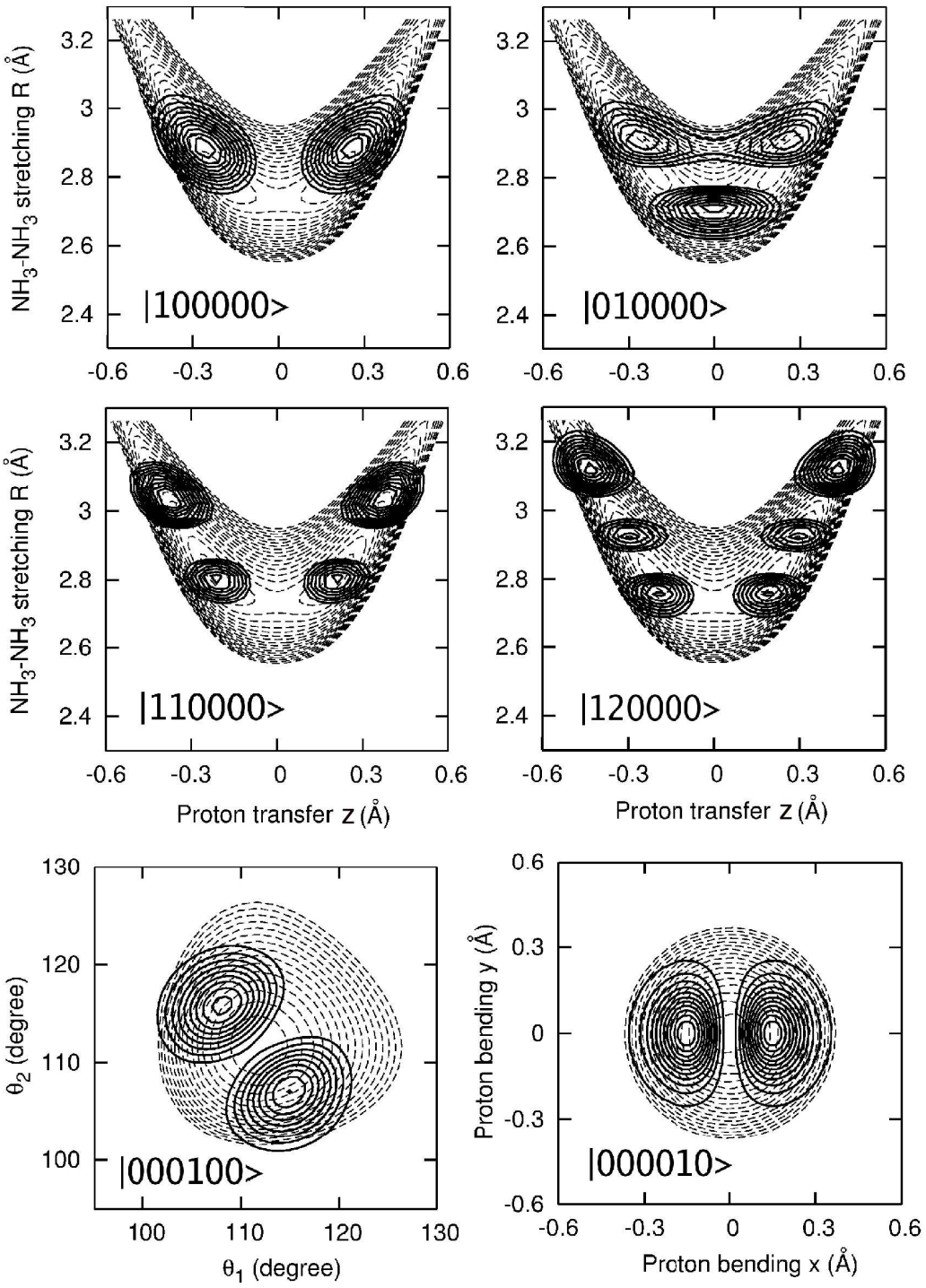

Figure 3.8: Two-dimensional reduced densities of typical excited states. See the text for details.

3.2.4 IR Spectrum

Before discussing the IR spectrum, it is instructive to recall the selection rules for dipole-allowed transitions as determined by the cation's symmetry. The Hamiltonian, Eqs. (3.8) and (3.7), and the dipole moment obey the following symmetry relations under the operation of inversion

$$H(-z, R, -\theta_a, \theta_s, -x, -y) = H(z, R, \theta_a, \theta_s, x, y)\,, \tag{3.11a}$$

$$\boldsymbol{\mu}(-z, R, -\theta_a, \theta_s, -x, -y) = -\boldsymbol{\mu}(z, R, \theta_a, \theta_s, x, y)\,. \tag{3.11b}$$

The Hamiltonian (or dipole moment) is an symmetric (or antisymmetric) under inversion. Thus we can derive an selection rule for the dipole transition. Due to symmetry all the non-degenerate eigenstates of the system have a definite parity

$$\psi_{mnklij}(-z, R, -\theta_a, \theta_s, -x, -y) = (-1)^{m+k+i+j}\psi_{mnklij}(z, R, \theta_a, \theta_s, x, y). \tag{3.12}$$

The final absorption intensity is proportional to the square of the matrix element of the dipole moment $\langle mnklij|\boldsymbol{\mu}|000000\rangle$ (See Appendix D for the details) at zero temperature. Therefore, $\psi_{mnklij}(-z, R, -\theta_a, \theta_s, -x, -y)$ must be antisymmetric to make the matrix element nonzero, i.e., the absorption intensity is nonzero only if the sum of related quantum numbers of the transition final state $m + k + i + j$ is odd.

The IR spectrum can be calculated by Fourier transform of dipole-dipole autocorrelation function or by matrix elements of dipole moment as mentioned above. The related theory adapted from Ref. [120] is detailed in Appendix D. Most quantum chemistry programs can calculate IR spectrum based on so called double harmonic approximation, i.e., harmonic potential energy and linear dipole moment function for each mode. Either the anharmonicity of PES or nonlinearity of dipole moment surface will leads to a failure of this kind of harmonic approximation. That is the reason why the harmonic predictions fails to interpret the experimental spectrum as we mentioned in the beginning. However, it can give right position of the fundamental of certain mode if the potential energy curve along the mode is not significantly anharmonic. In our 6D simulation we first obtained the eigenfunctions of the IR active transition final states. The IR spectrum is consequently calculated by matrix elements of dipole moment. The experimental and theoretical IR spectra are compared in Fig. 3.9.

The first IR active fundamental obtained by 6D theoretical calculation is located at 409 cm^{-1} due to the shared proton stretching (z) fundamental excitation. This agrees nicely with the IRMPD band **a** located at 374 cm^{-1} . Though the observed band **a′** may be energetically more close to the calculated value, the z fundamental excitation is expected to

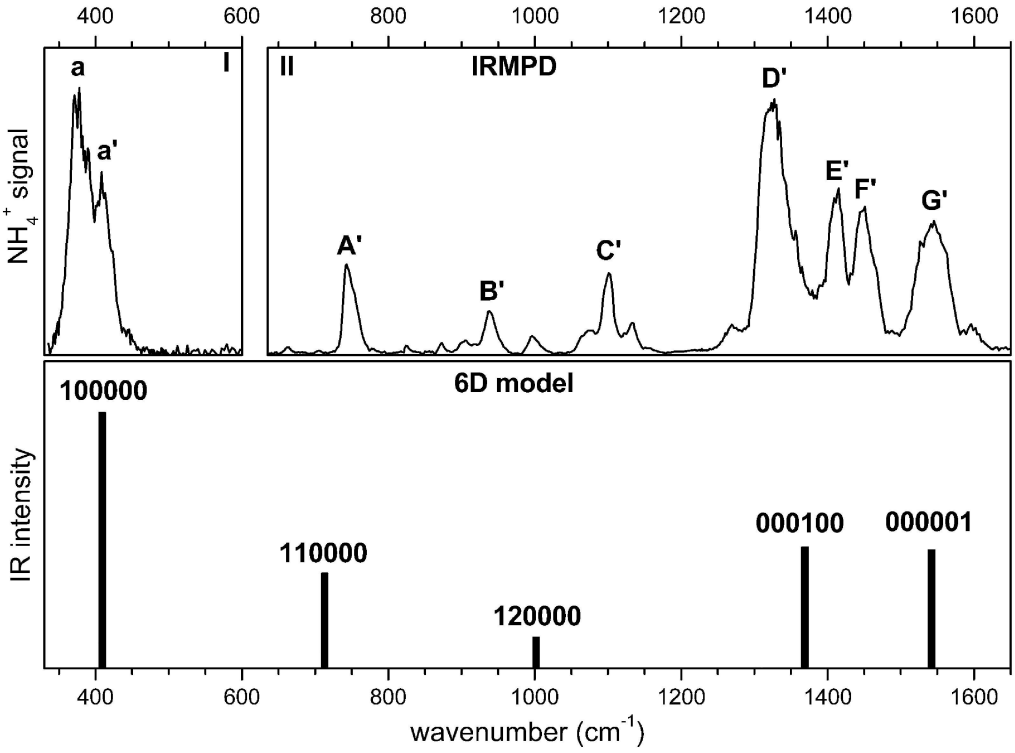

Figure 3.9: Experimental vs. theoretical IR spectrum. The upper two panels are experimental spectra obtained with different instruments by IRMPD technique by the Asmis group [96, 97]. The lower panel is the 6D simulation. See the text for details.

be the most intense feature in this region because the displacement of the shared proton along the N-N atom axis produces a large dipole oscillation. The other IR active mode in this frequency range could be the doubly degenerate wagging vibration which is not covered by our 6D model. The frequency of this mode is calculated at 418 cm^{-1} within the harmonic approximation which may be assigned to the second band $\mathbf{a}'$. The respective reduced probability of the shared proton stretching fundamental excitation is shown in Fig. 3.8 ($|100000\rangle$). It is interesting to note that the probability density for this state is more localized in the two well regions than the ground state distribution since the wave packets almost locate at the two potential minima. Notice that as compared to the harmonic prediction of this fundamental transition the frequency is significantly red-shifted by about 1500 cm^{-1}. The details can be found in the summary of assignments compiled in Table 3.3. The overtone of this mode is much larger than twice the fundamental transition which also reflects the considerable anharmonicity. In passing we note that an effective one-dimensional calculation in Ref. [98] captures part of this anharmonicity by predicting the transition at 707 cm^{-1}, however, this number is still too large.

The second IR active fundamental transition, calculated at 1369 cm^{-1}, is due to the

antisymmetric umbrella like motions of the two terminal NH_3 groups and it agrees very well with the experimental band **D′** at 1325 cm^{-1}. The antisymmmetric combination character is obvious from the reduced density in Fig. 3.8 ($|000100\rangle$). The third IR active fundamental transition, which is doubly degenerate due to the two equivalent bending modes perpendicular to the N-N line, is located at 1542 cm^{-1} which agrees perfectly with the experiment **G′** at 1545cm^{-1}. One reduced density of the degenerate states is shown in Fig. 3.8 ($|000010\rangle$).

Apart from these fundamental, combination transitions are also found to contribute significantly to the absorption spectrum. The transition at 713 cm^{-1} agrees nicely with the prominent experimental band **A′** at 743 cm^{-1} which therefore can be assigned to the combined excitation of the proton transfer and NH_3-NH_3 stretching modes $|110000\rangle$. In fact we find two more transitions in this progression which are IR active according to the symmetry selection rule, namely $|120000\rangle$ at 1002 cm^{-1} and $|130000\rangle$ at 1306 cm^{-1}. This exemplifies the strong correlation between the shared proton motion and the HB geometry deformation. The $|120000\rangle$ transition agrees reasonably with the observed band **C′** at 1097 cm^{-1}. Beyond the fundamental of the asymmetric umbrella motion at 1325 cm^{-1}, however, the assignment for the combinations becomes more tentative in part due to the limitations of the 6D model. The observed band **E′** at 1451 cm^{-1} could be due to the $|130000\rangle$ transition. In the Argon tagged IRVPD spectrum reported in Ref. [96] there are in fact only two dominant bands at 743 cm^{-1} and 1325 cm^{-1} corresponding to the $|110000\rangle$ and $|000100\rangle$ transition in the present model.

The comparison of theory and experiment as well as the assignments are summarized in Table 3.3. Apart from the 6D simulations the harmonic calculations and a 4D simulation reported by us previously [96] are also provided. The 4D calculation ignores the proton bending coordinates x and y. The 4D Hamiltonian is generated in the same spirit as the 6D one but the 4D PES expansion contains no three-mode correlations. The 4D dipole moment surface is generated in the same way as the PES expansion up to all the two-mode correlations. Having at hand the 4D Hamiltonian and dipole moment surface we have calculated the dipole-dipole autocorrelation function by exploiting MCTDH to propagate the 4D wave function. The IR spectrum based on 4D simulation is obtained by Fourier transform of dipole-dipole autocorrelation function. The 4D simulation has predicted the proton stretching fundamental to be at 460 cm^{-1} and the subsequent experiment has observed this band at 374 cm^{-1}, as shown in the left upper panel of Fig. 3.9. The 4D model has almost 20% error for this specific mode due to the ignoring of proton bending which has slight coupling with the other modes yet may strongly couple to the proton transfer mode. The 6D simulation which covers the bending x and y as has been

Table 3.3: Experimental and theoretical excitation energies (in cm^{-1}) of $N_2H_7^+$ below 1600 cm^{-1}. The 4D result only relates to the first four quantum numbers hence no bending values. Harmonic predictions are performed with MP2/aug-cc-pVTZ. The modes labeled by stars are not exactly the same as the assignments.

	anharmonic		harmonic			
$\|mnklij\rangle$	4D	6D	TS	Min	experiment	assignment
010000	421	403	565	313*		NH_3-NH_3 stretch ν_R
100000	460	409	$843i$	1944	374	proton stretch ν_z
020000	729	701				$2 \cdot \nu_R$ overtone
110000	766	713			743	$1 \cdot \nu_z + 1 \cdot \nu_R$
030000	1030	981				
120000	1089	1002			1097	$1 \cdot \nu_z + 2 \cdot \nu_R$
001000	1348	1336	1342	1264*		symm. umbrella ν_{θ_s}
000100	1354	1369	1362	1380*	1325	asym. umbrella ν_{θ_a}
130000	1488	1306			1451	$1 \cdot \nu_z + 3 \cdot \nu_R$
000001	-	1542	1777	1779*	1545	proton bending ν_y
000010	-	1542	1777	1779*	1545	proton bending ν_x
200000	1546					$2 \cdot \nu_z$ overtone

mentioned in Section 3.2.1 greatly decreases this error.

We further demonstrate the comparison between our theoretical calculations and the experimental results in Fig. 3.10. As can be seen the multidimensional anharmonic simulations agree well with the experiment. It should be noted that the 4D simulation excludes the bends x and y thus the degenerate bending mode is missing in the 4D result. One may argue that the 4D result fits the experiment even better for the combination bands $|mn00\rangle$. In 4D model we cover all the coordinates which conserve the C_3 symmetry since the couplings between different symmetries are much smaller than those within the same

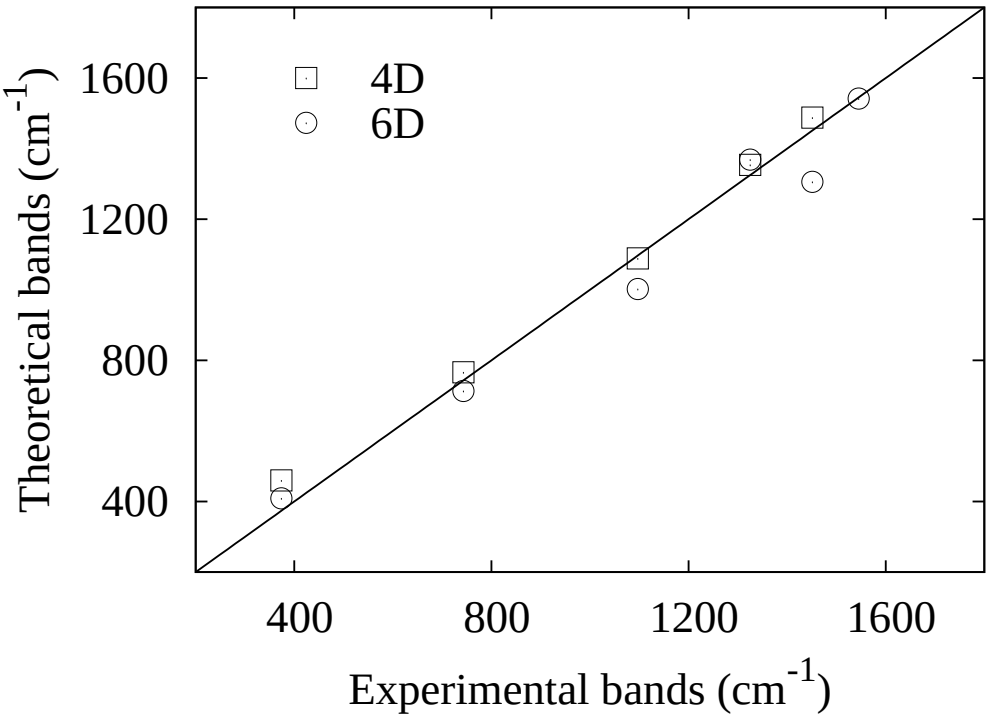

Figure 3.10: Comparison of theoretical and experimental IR active bands. The six bands in increasing order are $|100000\rangle$, $|110000\rangle$, $|120000\rangle$, $|000100\rangle$, $|130000\rangle$ and the degenerate bending mode $|000010\rangle$ or $|000001\rangle$, respectively. See the text for more details.

symmetry. The 4D model is a reasonable truncation with respect to its lower level of accuracy yet the 6D truncation is slightly less reasonable with respect to the corresponding higher level of accuracy. A more reasonable description is to consider the modes which have relatively stronger couplings to the NH_3-NH_3 stretching mode, i.e., the wags of the two terminal ammonias. This is why 6D result needs refinements for the combination bands while the 4D result gives a reasonable explanation at the corresponding lower level of accuracy. However, concerning the proton transfer z fundamental transition, the 4D result agrees with the experiment not as well because this mode does couple relatively strongly to certain modes which break the C_3 symmetry, i.e., the two bending modes x and y. This is why we greatly decrease the error of z fundamental in our 6D simulation by accounting for the bending. The other reason is the accuracy of the PES expansion. Though the 6D PES expansion includes major three-mode correlations it is still slightly less accurate than the 4D expansion concerning the correlation part. We need more correlation terms for the higher dimensional (6D) PES expansion at least all the fourth order correlations which involves the three proton coordinates x, y and z. A better solution for high dimensions is to combine certain strongly coupled coordinates as a group to treat

high dimensional correlations more conveniently, which will be applied to a full dimensional study in the next chapter. In principle the grouping coordinates method can also be applied to the present system but we would need high dimensional $ab\ initio$ PES data which are unfortunately not available up to now.

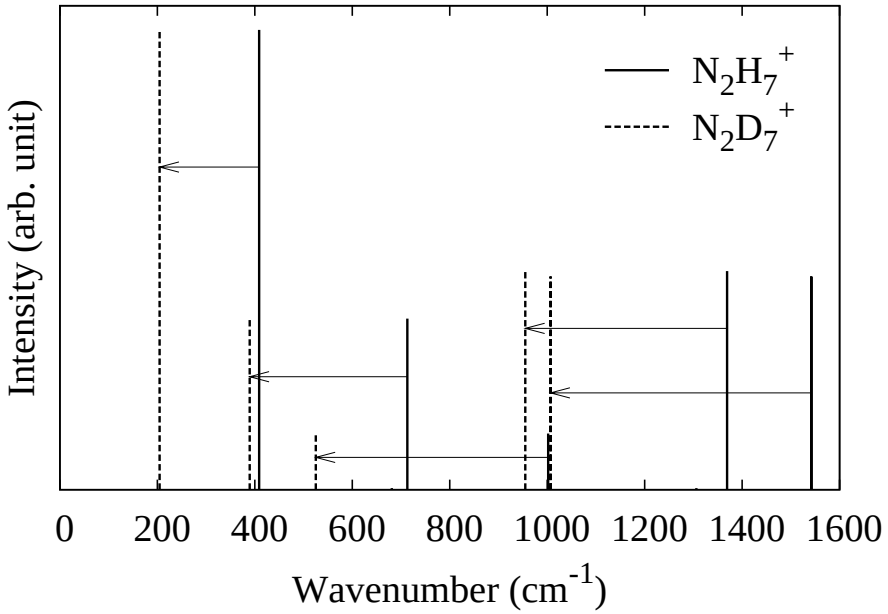

Figure 3.11: Comparison of IR spectra of $N_2H_7^+$ (solid) and $N_2D_7^+$ (dashed) obtained by 6D simulation. See the text for details.

We have also performed a 6D simulation for $N_2D_7^+$. The calculated IR spectra is shown in Fig. 3.11. The five IR active bands for both cations are $|100000\rangle$, $|110000\rangle$, $|120000\rangle$, $|000100\rangle$, and the degenerate bending mode $|000010\rangle$ or $|000001\rangle$ with increasing frequency. For the $|100000\rangle$ state, the red shift due to deuteration is 50% which reflects strong anharmonicity. An interesting effect is that the combination bands $|110000\rangle$ and $|120000\rangle$ also have about 45% redshifts though the deuteration has small effect on the R mode. For the $|000100\rangle$, $|000010\rangle$ and $|000001\rangle$, the redshifts do not deviated significantly from the harmonic ones $(1-1/\sqrt{2})$ which reflects less anharmonicity as compared to the proton transfer mode.

3.3 Geometries and IR Spectra of Larger Clusters

In principle it would be straightforward to apply the method outlined above to larger clusters to perform reasonable reduced dimensional descriptions. It turns out, however, that the HB in $N_2H_7^+$ is exceptional insofar as it is particularly strong compared to $NH_4^+(NH_3)_n$ ($n = 2-4$). Consequently, the PES is considerably less anharmonic for larger clusters

Table 3.4: HBs parameters (lengths in Å) for $NH_4^+(NH_3)_n$ ($n = 2-4$). The same notation q_1 is adopted to characterize the hydrogen displacement as in Fig. 3.7.

size n	N$\cdots$N distance	N–H length	H displacement q_1
2	2.82	1.07	0.34
3	2.90	1.05	0.40
4	2.96	1.04	0.44

which means that simple harmonic predictions may successfully describe them. To confirm whether this is true we first study the anharmonicity of the corresponding PES to check the validity of harmonic predictions.

3.3.1 Geometries and PESs of Larger Clusters

We have calculated the equilibrium geometries of these clusters using the MP2/6-311+G(d,p) level of theory, see Fig. 3.1. The exact configuration of each classical minimum slightly deviates from the expected symmetry, i.e., the C_{2v} symmetry of $NH_4^+(NH_3)_2$, the C_{3v} symmetry of $NH_4^+(NH_3)_3$ and the T_d symmetry of $NH_4^+(NH_3)_4$. This is due to the limitation of the assumption of classical nuclei. In general the configuration with highest symmetry does not correspond to the minimum. However the quantum ground state of each cluster does have the corresponding symmetry mentioned above just like what we have studied in the $N_2H_7^+$ case. In the following we will ignore the symmetry deviations of classical minimum configurations. Each larger cluster has a solvated ammonium structure with a central NH_4^+ unit which turns out to be quite stable hence significantly decreases the HB strength. The details of HBs parameters are compiled in Table 3.4 which further reflects slight decrease of the HB strength with increasing cluster size n for $n = 2 - 4$. The HBs geometries also agrees well with the empirical correlation curves shown in Fig. 3.7.

To address the degree of anharmonicity the potential curve along one of the hydrogen-bonded N-H stretching coordinates, i.e., the proton transfer modes, has been determined with the other coordinates frozen. The results in Fig. 3.12 show that upon increasing the cluster size n the potential becomes less anharmonic. The solid line is calculated by MP2/aug-cc-pVTZ for $n = 2$ and the dashed lines are calculated by MP2/6-311+G(d,p)

for $n = 2 - 4$. For $n = 2$ it still shows some double minimum topology, although a barrier as high as 4000 cm^{-1} is required to overcome to reach the higher proton transfer minimum. A quite deep potential well hampers the proton transfer process, i.e., the proton distribution is well confined around the lower minimum configuration. For $n = 3, 4$ there is no stable proton transfer minimum at all and the depths of potential wells increase with the cluster size. Notice that the actual well depth depends on the level of quantum chemistry. We have performed both MP2/aug-cc-pVTZ and MP2/6-311+G(d,p) level of calculations for $n = 2$ and the difference turns out to be negligible especially around the deep potential well, i.e., the nearly harmonic region. This in turn makes the accuracy of MP2/6-311+G(d,p) PESs reliable around the deep potential well as can be seen clearly in Fig. 3.12.

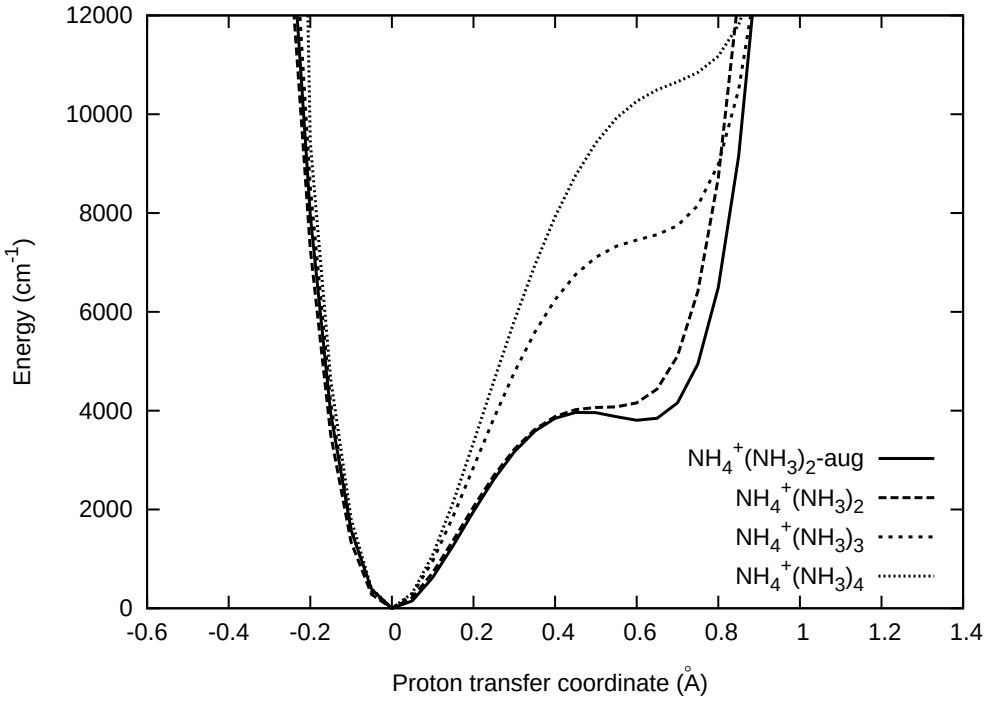

Figure 3.12: One dimensional potential energy curves of $NH_4^+(NH_3)_n$ cations (n=2-4) along an N-H proton transfer coordinate at the MP2/6-311+G(d,p) (dashed) and MP2/aug-cc-pVTZ (solid) level of theories. The asymmetric characteristics can be understood from the structures shown in Fig. 3.2.

Though the classical minimum for $N_2H_7^+$ also contains the NH_4^+ structure it turns out to be symmetrized by quantum zero point vibration since the potential well is sufficiently shallow. Different from the $N_2H_7^+$ case, the PES of each $NH_4^+(NH_3)_n$ ($n > 1$) cation shows a rather deep potential well due to significant weakening of HB. As has been discussed in Chapter 1 the harmonic approximation may catch some essence of this kind of weak HBs. Based on Fig. 3.12 we will restrict our discussion within harmonic approxi-

mation only, but including a scaling factor of 0.95 for the MP2 frequencies. This will turn out to be sufficient for analyzing the size dependence of the experimental spectra.

3.3.2 IR Spectra for $NH_4^+(NH_3)_n$ ($n = 2 - 4$)

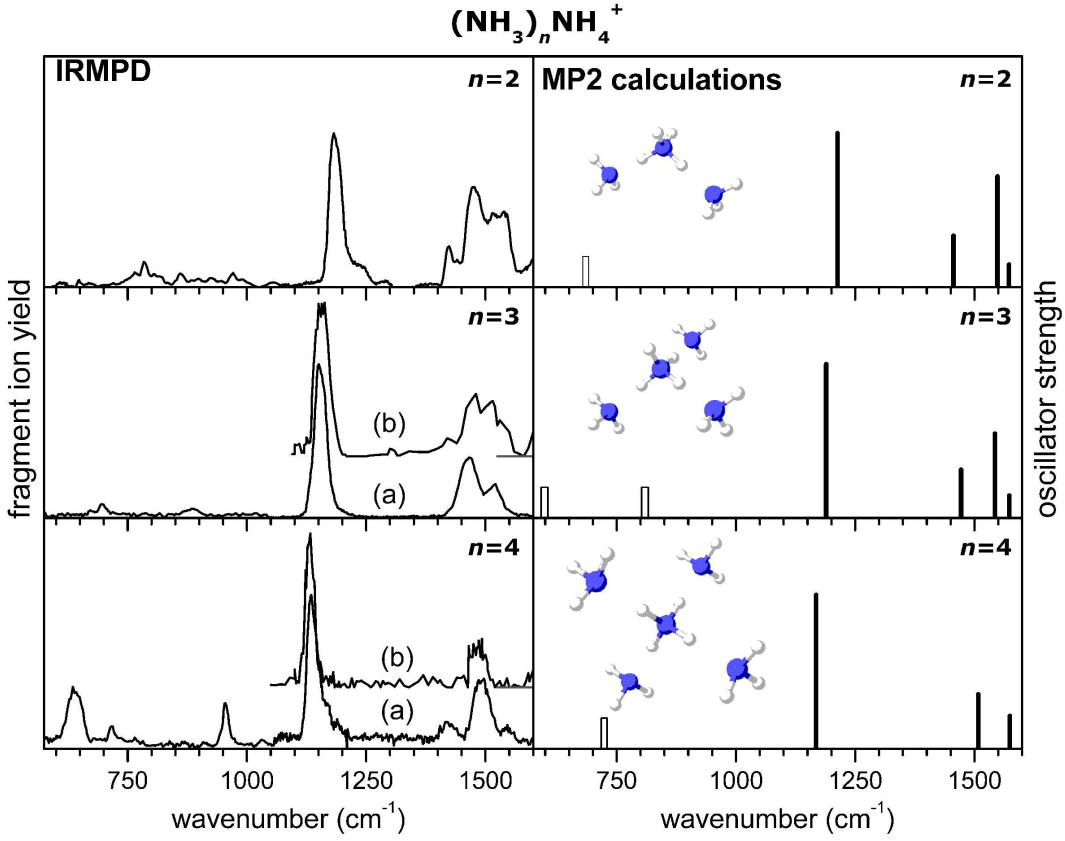

Figure 3.13: Left: Experimental IR spectra of $NH_4^+(NH_3)_n$ ($n = 2-4$) [97]. For $n = 3, 4$ the spectra obtained by Tono et al [52] are also shown (b). Right: For $n = 2 - 4$ the calculated harmonic MP2/6-311+G(d,p) frequencies (scaled by 0.95) are shown as open or solid bars for transitions having no or finite oscillator strength, respectively.

The infrared spectra of the $NH_4^+(NH_3)_n$ clusters ($n = 1 - 4$) measured by the Asmis group with the IRMPD technique as well as harmonic calculations are shown in Fig. 3.13. As discussed above the significant weakening of the HBs decrease the anharmonicity of the PES. Therefore, we can compare the measured spectra with the results of the harmonic approximation. There are systematic redshifts of the most intense absorption peaks with increasing size. The calculated frequencies for relevant transitions at the MP2/6-311+G(d,p) level of theory are compiled in Tab. 3.5. For the most intense absorption band between 1100 and 1200 cm^{-1} this gives an excellent agreement, allowing the assignment of this band to the collective ν_2 bending mode of side NH_3 which corresponds

to the asymmetric umbrella motion in the $N_2H_7^+$ case. To have a clearer picture, the ν_2 bending mode of an ammonia molecule is shown in Fig. 3.14a).

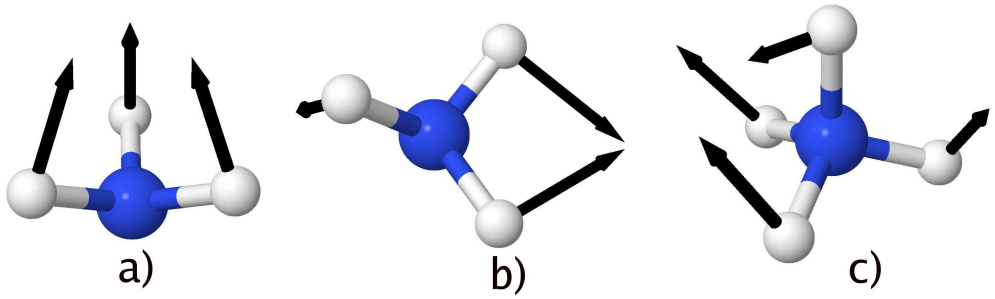

Figure 3.14: Visualization of selected modes of ammonia and ammonium. a) ν_2 type bending mode of ammonia. b) ν_4 type bending mode of ammonia, only one of the 2-fold degenerate modes are shown. c) ν_4 type bending mode of ammonium, only one of the 3-fold degenerate modes are shown.

Notice that the red shift of this band with increasing cluster size, discussed for n=3, 4 in Ref. [52], is also consistent with the data for n=2. Weakening of the HBs, responsible for the red shift of the ammonia ν_2 mode, is reflected also in the increase of the N-N distances calculated by MP2/6-311+G(d,p): 2.82Å in n=2, 2.90Å in n=3, and 2.96Å in n=4, thus softening the NH_3 bending PES. For comparison, the ν_2 mode of an isolated ammonia molecule is 950 cm^{-1} [104] which can be imagined as the limit case where the $N\cdots N$ distance goes to infinity.

The region between 1400 and 1600 cm^{-1} is composed of several collective asymmetric NH_3 bending vibrations (ν_4 type) as well as of NH_4^+ ν_4 type bending fundamentals. One of the degenerate ν_4 type vibrations of NH_3 (NH_4^+) is shown in Fig. 3.14. The collective ν_4 modes of both NH_3 and NH_4^+ have blue shifts with increasing cluster size which agree with the experiments.

The observed bands in the region between 600 cm^{-1} to 1100 cm^{-1} are most likely dominated by the complicated relative motions of central NH_4^+ and terminal NH_3 groups. We can consider the NH_4^+ and NH_3 as rigid fragments to efficiently describe this kind of motions. However, to obtain the corresponding multidimensional PESs are time consuming, though feasible concerning present computer abilities. As for the harmonic approximations, we have found some relevant modes in the region between 600 cm^{-1} to 1100 cm^{-1} without absorption intensity under the linear dipole approximation. These modes are all relative motions of rigid NH_4^+ and NH_3 fragments as mentioned above, more specifically they are the hindered rotations of central NH_4^+ fragment. For $n = 2$, located at 657 cm^{-1}, the hindered rotation is in the plane of three fragments. For $n = 3$ there are two hindered rotations, one perpendicular and one parallel to the plane of three terminal NH_3

Table 3.5: Assignment of IR spectra for $NH_4^+(NH_3)_n$ ($n = 2 - 4$). The calculations have been performed in harmonic approximation using the MP2/6-311+G(d,p) level of theory and a scaling factor of 0.95 has been applied. Energies are expressed in cm^{-1} .

n	experiment	This work	Ref. [52]	assignment
2	1182	1213		$\nu_2(NH_3)$
	1424	1456		$\nu_4(NH_4^+)$
	1475	1548		$\nu_4(NH_4^+)$+$\nu_4(NH_3)$
	1540	1572		$\nu_4(NH_3)$
3	1151	1189	1157	$\nu_2(NH_3)$
	1468	1472	1491	$\nu_4(NH_4^+)$
	1521	1543		umbrella NH_4^+
		1573	1624	$\nu_4(NH_3)$
4	635			
	719			
	955			
	1135	1168	1132	$\nu_2(NH_3)$
	1422			
	1497	1508	1483	$\nu_4(NH_4^+)$
	1546	1574	1599	$\nu_4(NH_3)$

fragments, located at 536 cm^{-1} and 712 cm^{-1} respectively. The $NH_4^+(NH_3)_4$ is similar to the $NH_4^+(NH_3)_3$ except for the two modes are nearly degenerate at 639 cm^{-1} due to its higher symmetry.

3.4 Summary

In this chapter we have studied the geometries and low frequency IR spectra of protonated ammonia clusters and obtained reasonable agreement with experiments. The $N_2H_7^+$ cation is a strongly hydrogen-bonded low-barrier system with symmetrical structure caused by zero-point vibration. Multidimensional quantum dynamics is necessary to pursue reliable interpretations of the IR spectrum. Therefore we select six coordinates which most closely relate to the HB. The quantum dynamics of the reduced 6D model describes the system quite well. By reasonably incorporating the anharmonicity, our results [96, 97] have successfully interpreted the very recent experimental IR spectrum which is very difficult to be explained with previous theoretical work [53, 55, 98]. The fundamental for the shared proton stretching mode at 409 cm^{-1} by our calculation is significantly red shifted compared with the harmonic prediction (by more than 1500 cm^{-1}) due to the strong HB. Though an effective one-dimensional calculation in Ref. [98] captures part of this anharmonicity by predicting the transition at 707 cm^{-1} , it is still too large. The combinations between the shared proton stretching and the terminal NH_3–NH_3 stretching are also found to contribute significantly to the IR bands below 1100 cm^{-1} .

For $NH_4^+(NH_3)_n$ ($n = 2-4$) we apply harmonic approximation since the weakening of HB with the increasing of cluster size significantly reduces the anharmonicity. The calculated IR spectra agree with the recent experiments by the Asmis group and have assigned the most intense band to be the asymmetric collective ν_2 bending motions of the terminal ammonia [97]. The systematic red shift of this band is due to the weakening of the HB strength. As a result of different bond strength, the $N_2H_7^+$ cation has a strong HB which leads to the shared proton structure and rich IR bands below 1100 cm^{-1} . While the large clusters have weak HBs which lead to solvation ammonium structures consequently no vibrational bands caused by HB stretching dynamics below 1100 cm^{-1} . However, from the experimental data for large clusters especially $n = 4$, there may be some complicated relative motions of central NH_4^+ and terminal NH_3 fragments resulting the measured IR bands in the low frequency region which can be unraveled by multidimensional quantum investigation with a reduced model.

The multidimensional quantum dynamics provide us rather convincing results for clear interpretation of fundamental processes as long as our reduced model is reasonable. However if the system we are interested in is quite floppy or the point we intend to elucidate entangles the whole system we have to resort to the full dimensional dynamics. In the next chapter we will perform a full dimensional study on the deprotonated water dimer.

Chapter 4

Full-Dimensional Study of $H_3O_2^-$ and its Isotopomers

4.1 Introduction

The hydrated proton and its negative analogue, the hydrated hydroxide anion, have already been investigated in quite some detail. However it is only very recently that the Zundel cation, $H_5O_2^+$, has been clearly elucidated by $ab\ initio$ quantum dynamical calculations [37, 38, 39], however, the corresponding breakthrough in $H_3O_2^-$ is not available. The principal difficulty in assigning the $H_3O_2^-$ spectrum arises from the fact that similar to the Zundel cation one has to deal with a strong HB in a floppy structure which affects especially the transition frequency of the central hydrogen stretching vibration drastically. In other words, the vibrational dynamics is rather anharmonic and any calculation bound to the harmonic approximation is likely to fail at least for the HB dynamics. This points to the need for a multidimensional treatment of the infrared spectrum as reported by J. Bowman and coworkers who used the multi-mode reaction path along the HO$\cdots$OH torsion coordinate and diffusion Monte Carlo techniques [42, 45]. Their results have qualitatively interpreted the related experiments by Johnson group [40, 43, 44]. For the specific case of the shared hydrogen stretch fundamental, these methods gave 741 cm^{-1} and 644 cm^{-1}, respectively. However combinations will play an important role just like other strong hydrogen bonded systems.

In this chapter we will not focus on the IR spectrum since qualitative interpretations are already available. Instead we focus on the effect of H/D isotopic substitution on the properties of the HB in this complex. One may naturally ask whether deuteration of the hydroxide ([D–O$\cdots$H$\cdots$O–H]$^-$) or the "solvent" water ([H–O$\cdots$D$\cdots$O–H]$^-$ yields an energetically more stable structure. This issue is related to the problem of isotopic ex-

change equilibrium configurations and associated fractionation factors which have been discussed for gas phase reactions of hydrogen-bonded ions [105, 106] as well as in aqueous [107, 108] and other [109, 110] solutions. An extensive account on the stability of various charge and neutral water clusters has been given by Scheiner and coworker employing the MP2 method together with a (small) 6-31+G** basis set [111]. It is important to note that their conclusions for the relative stabilities of different isotopomers have been drawn from harmonic calculations with respect to a nonsymmetric equilibrium structure. The view of the discussion above calls for having a second look at this problem from the perspective of a quantum mechanical treatment in full dimensionality.

The change in strength of the HB upon isotopic substitution is also reflected in GIEs which is yet another manifestation of the multidimensional anharmonic nature of the PES [34, 112]. For weak HBs with a double minimum PES, deuteration leads to a shorter O–D distance as compared to O–H. This in turn weakens the HB consequently increase the O$\cdots$O distance. For strong symmetric HBs where the ZPE is above the barrier and the vibrational distribution has its maximum at the barrier top, deuteration reduces the width of this distribution which pulls the oxygens towards the deuterium, that is, the O$\cdots$O distance decreases. An interesting case occurs when the ZPE in the deuterated case is below the reaction barrier and the vibrational distribution becomes bimodal. This would correspond more to the situation of a weak HB and the O$\cdots$O distance should increase. For the fully deuterated case $D_3O_2^-$, its distribution may be bimodal only after the influence of environment at finite temperature is taken into account as reported in Ref. [113] by $ab\ initio$ path integral simulations. Here we will address the GIEs for all the different isotopomers on the basis of the full-dimensional ground state wave functions.

In the following Section 4.2.1 we will present a nine-dimensional (9D) Hamiltonian which describes the vibrational motion of $H_3O_2^-$ in full-dimensionality for total angular momentum equal to zero. This Hamiltonian is based on the CCSD(T)/aug-cc-pVTZ level of PES developed by Bowman and coworkers [45]. The corresponding operator for the kinetic energy is given in the Appendix C. The vibrational ground state is obtained by imaginary time-propagation using MCTDH method [90, 29]; numerical details of the calculation are given in Section 4.2.2. In Section 4.3 we will present results on the vibrational ground state of the different isotopomers as well as on the GIEs. The torsional tunneling splittings are also investigated in this section.

4.2 Theoretical Model

4.2.1 9 Dimensional Hamiltonian

The choice of coordinates is crucial as it determines the strength of correlations between different degrees of freedom in the potential and kinetic energy operator thus directly affects the accuracy if truncation of correlations are made. For the present case the issue is complicated as there is the possibility of large amplitude torsional motion. This made it necessary to use a reaction path approach in Ref. [45], which combined the torsional reaction coordinate with orthogonal normal mode displacements taken with respect to the C_2 transition structure. Here we will use internal coordinates, which is less restrictive but comes at the expense of a more complicated KEO.

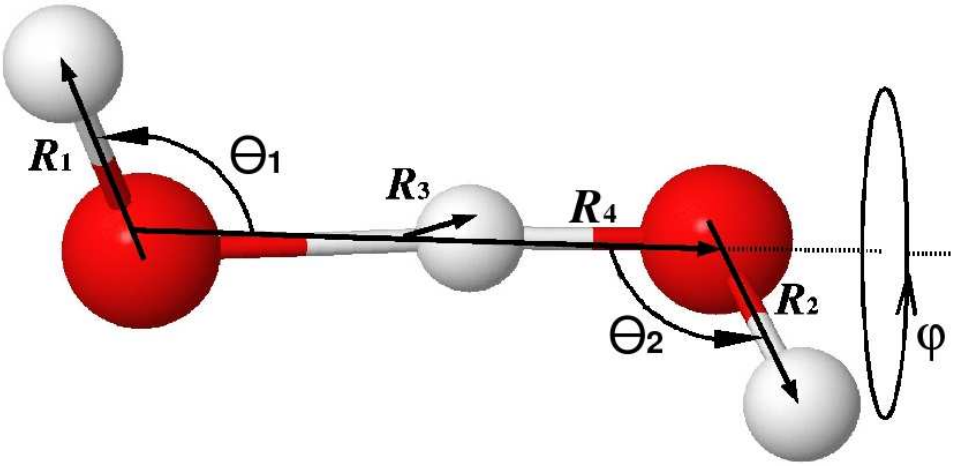

Figure 4.1: The four Jacobi vectors used for defining the nine internal coordinates. See the text for the definition of the nine coordinates.

We first derive the full dimensional KEO in the LRF. After separating the total center of mass motion, the four Jacobi vectors shown in Fig. 4.1 will be used: $\boldsymbol{R}_1$ and $\boldsymbol{R}_2$ each connecting one oxygen and the "free" hydrogen atom, $\boldsymbol{R}_4$ connecting two centers of mass of the OH groups, and $\boldsymbol{R}_3$ connecting the shared hydrogen atom and the center of mass of the O_2H_2 fragment (for the deuterated cases one or more hydrogen atoms are replaced by deuterium atoms). We can use only nine internal coordinates to describe the system for the total angular momentum $\boldsymbol{J} = 0$ according to Section 2.2.5. Based on these Jacobi vectors the following nine internal coordinates are chosen: the lengths R_1, R_2, and R_4, of the vectors $\boldsymbol{R}_1$, $\boldsymbol{R}_2$, and $\boldsymbol{R}_4$, respectively, the angle θ_1 (θ_2) between $\boldsymbol{R}_1$ and $\boldsymbol{R}_4$ ($\boldsymbol{R}_2$ and $\boldsymbol{R}_4$), and the dihedral angle φ between the planes spanned by the vectors ($\boldsymbol{R}_1$, $\boldsymbol{R}_4$) and ($\boldsymbol{R}_2$, $\boldsymbol{R}_4$) which describes the torsional motion. Notice that due to its definition with

respect to the Jacobi vectors, φ is slightly different from the torsional coordinate used in Ref. [45], since our torsional axis is the direction of $\boldsymbol{R}_4$. For $\boldsymbol{R}_3$ we use Cartesian components x, y, and z in certain MRF which contribute negligible Coriolis couplings. The origin of the MRF is the center of mass and z is defined along the direction of $\boldsymbol{R}_4$, i.e. it roughly corresponds to the shared proton stretch mode. The xz plane equally divides the torsional angle φ if the reduced mass associated with $\boldsymbol{R}_1$ is the same with that associated with $\boldsymbol{R}_2$. Otherwise the division ratio is 1:2 or 2:1 depending on whether the mass ratio is 2:1 or 1:2. For the details as well as the expression for the 9D KEO please see Appendix C. Notice that in the following numerical simulations we will use the new variables $u_i = \cos\theta_i (i = 1, 2)$ as in Chapter 3.

The full-dimensional potential energy surface can be constructed by cumulative expansion of different correlation orders according to Eq. (2.38). Following the strategy of Ref. [38] we will combine certain groups of coordinates to treat their correlations exactly. Specifically we have chosen the three groups $\boldsymbol{g}_1 = [R_1, R_2, R_4]$, $\boldsymbol{g}_2 = [u_1, u_2, \varphi]$, and $\boldsymbol{g}_3 = [x, y, z]$. The final expansion we used to generate the 9D PES reads

$$V(\boldsymbol{g}_1, \boldsymbol{g}_2, \boldsymbol{g}_3) = V_0 + \sum_i V^{(1)}(\boldsymbol{g}_i) + \sum_{i<j} V^{(2)}(\boldsymbol{g}_i, \boldsymbol{g}_j), \tag{4.1}$$

where $V^{(n)}$ gives the n-set correlation between sets of coordinates. Notice, however, that this PES contains up to 6-mode correlations between individual coordinates. In Eq. (4.1) $V_0 = V(\boldsymbol{g}^{(0)})$ is the energy of the reference geometry, $\boldsymbol{g}^{(0)}$.

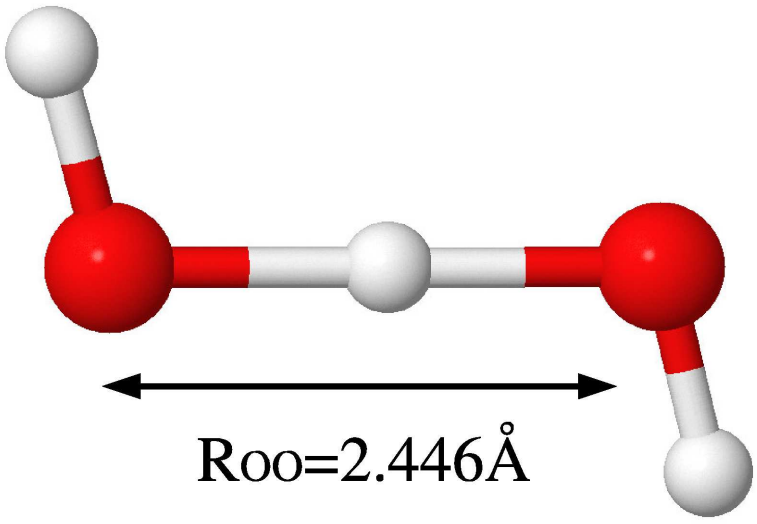

Figure 4.2: The C_{2h} transition state configuration with five atoms in the same plane.

According to the error of Taylor expansion we know that the expansion error of Eq. (4.1) increases if the geometry $\boldsymbol{g}$ we want to calculate significantly differs from the

reference geometry $\boldsymbol{g}^{(0)}$. Since we are mainly interested in the ground state properties the most natural thing will be to increase the accuracy of the PES expansion around the region where the quantum ground state wave function covers, i.e., $\boldsymbol{g}^{(0)}$ should correspond to the most probable geometry or average geometry of the quantum ground state. One should further be careful to chose the reference geometry $\boldsymbol{g}^{(0)}$ since inappropriate $\boldsymbol{g}^{(0)}$ will break the symmetry of the original PES. One can find out that the expansion of Eq. (4.1) conserves the symmetry if the symmetry of the reference geometry $\boldsymbol{g}^{(0)}$ is not lower than that of the PES. An obvious choice for this symmetry adapted reference is the classical transition state geometry. There are several transition state configurations even in the low energy region. When we say transition state we actually mean the trans- configuration as shown in Fig. 4.2 with C_{2h}, the highest symmetry among all the low energy equilibrium configurations [45].

We have performed a ground state calculation based on the classical transition state reference geometry and obtained an error of about 2-3 cm^{-1} per degree of freedom as compared to the Quantum Monte Carlo results for $H_3O_2^-$ reported in Ref. [45]. This is a rather small error with respect to the full ground state energy which is more than 6000 cm^{-1} yet the accuracy can be further improved by defining $\boldsymbol{g}^{(0)}$ according to the quantum ground state as mentioned above. And we get essentially a quantitative agreement when we take the symmetry of the classical transition state yet replace the corresponding bond lengths and angles by the expectation values of quantum mechanical ground state (as obtained from the calculation for $HOHOH^-$ based on classical transition state reference) to define the reference geometry $\boldsymbol{g}^{(0)}$. For simplicity as well as the consistence of PES expansion we have employed this reference for all isotopomers (see Table 4.1).

For generating the PES in the given coordinates we have used the fitted CCSD(T)/aug-cc-pVTZ potential of Bowman and coworkers [45]. Two representative cuts of the PES are shown in Fig. 4.3. In Fig. 4.3 (a) we show the PES along two most strongly coupled coordinates z and R_4 ($O\cdots O$ distance). The shape looks similar to Fig. 4.3(a) of the $N_2H_7^+$ investigated in Chapter 3 since they are both strong hydrogen bonded symmetric dimers. Apart from the two asymmetric minimum configurations there exists a transition state with compressed $O\cdots O$ distance in between with a rather shallow barrier around 70 cm^{-1} for fully relaxed proton transfer according to Ref. [42]. The barrier height can be read from the minimum of Fig. 4.3 (b) since the energy reference is energy of the minimum configuration. This number is larger than 70 cm^{-1} due to the freezing of the other coordinates at the transition state. The potential energy curve along the torsion coordinate φ is shown in Fig. 4.3 (b) with a double minimum shape. The barrier for the torsion motion is about 150 cm^{-1} which is large enough to cause tunneling splitting since

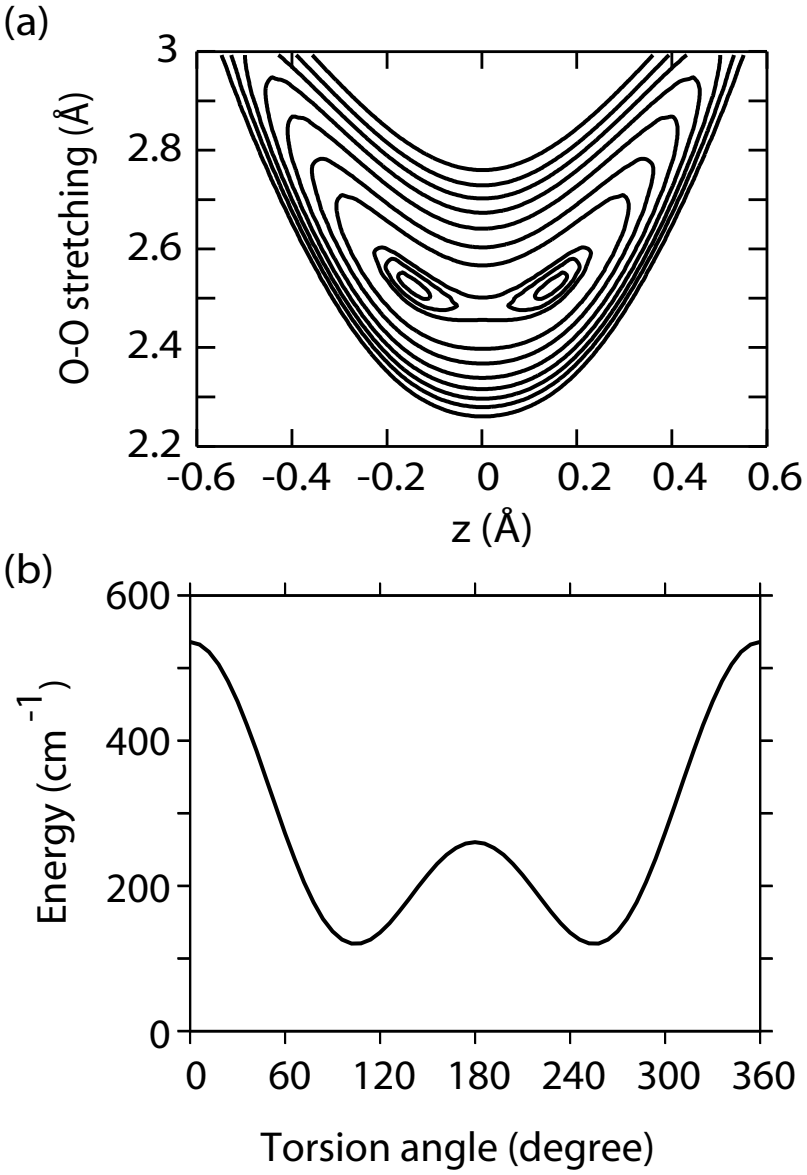

Figure 4.3: (a) PES along O$\cdots$O distance (R_4) and proton transfer coordinate z (contour lines at (in cm^{-1}): 230, 260, 300, 600, 900, 1300, 1700, 2100, 2500, 3000). (b) Potential energy curve along torsion coordinate φ. In both cases all other coordinates have been kept frozen at the transition state geometry.

the zero point energy related to the torsion mode is much less than the barrier height.

4.2.2 Numerical Implementation

The vibrational ground state of the different isotopomers has been obtained by the MCTDH method [90, 29] detailed in Chapter 2. Three needed 6D PESs which are $V^{(1)}(\boldsymbol{g}_1) + V^{(2)}(\boldsymbol{g}_1, \boldsymbol{g}_2)$, $V^{(2)}(\boldsymbol{g}_2) + V^{(2)}(\boldsymbol{g}_2, \boldsymbol{g}_3)$ and $V^{(1)}(\boldsymbol{g}_3) + V^{(2)}(\boldsymbol{g}_1, \boldsymbol{g}_3)$ have been

Table 4.1: MCTDH parameters for the imaginary time propagation (lengths in Å, N_{DVR}: number of DVR points; N_{SPF}: number of SPFs.) and reference geometry, $\boldsymbol{g}^{(0)}$, for the PES expansion in Eq. (4.1) (X=H or D). The last row is the transition state described with coordinates of $HOXOH^-$. For the details of the nine coordinates please see Fig. 4.1, here $u_i = \cos\theta_i$.

	R_1	R_2	R_4	u_1	u_2	φ	x	y	z
min. grid	0.740	0.740	2.275	-1.0	-0.7	0	-0.635	-0.635	-0.529
max. grid	1.322	1.322	3.069	0.7	1.0	2π	0.635	0.635	0.529
N_{DVR}	11	11	16	13	13	17	13	13	17
N_{SPF}		5			10			13	
$\boldsymbol{g}^{(0)}$: $HOXOH^-$	0.979	0.979	2.519	-0.25	0.25	π	0.0	0.0	0.0
$\boldsymbol{g}^{(0)}$: $DOXOD^-$	0.979	0.979	2.547	-0.288	0.288	π	0.0	0.0	0.0
$\boldsymbol{g}^{(0)}$: $DOXOH^-$	0.979	0.979	2.532	-0.269	0.269	π	-0.012	0.021	0.043
TS: $HOXOH^-$	0.962	0.962	2.477	-0.282	0.282	π	0.0	0.0	0.0

fitted to a sum of products using the POTFIT approach [29]. For the representation of the SPFs a discrete variable representation (DVR) has been utilized. For the torsional coordinate φ an exponential DVR representation with periodic basis functions (eigenfunctions of $\frac{d}{d\varphi}$) has been used. All other coordinates have been expressed via a harmonic oscillator DVR. The SPF basis functions cover the range energies below 10000 cm^{-1}; the smallest natural orbital population in the ground state is 0.0003. All parameters are compiled in Tab. 4.1.

The reference geometry, $\boldsymbol{g}^{(0)}$, for the PES expansion in Eq. (4.1) is also detailed in Tab. 4.1 in terms of our nine coordinates. Note that the coordinates of the reference geometry are based on expectation values for the $HOHOH^-$ case. The actual different values reported here for the different isotopomers are purely due to the fact that the Jacobi vectors defining the coordinate system are mass-dependent. The classical transition state (TS) reference is also given in terms of coordinates of $HOXOH^-$ for comparison.

4.3 Results

4.3.1 Vibrational Ground State Geometry

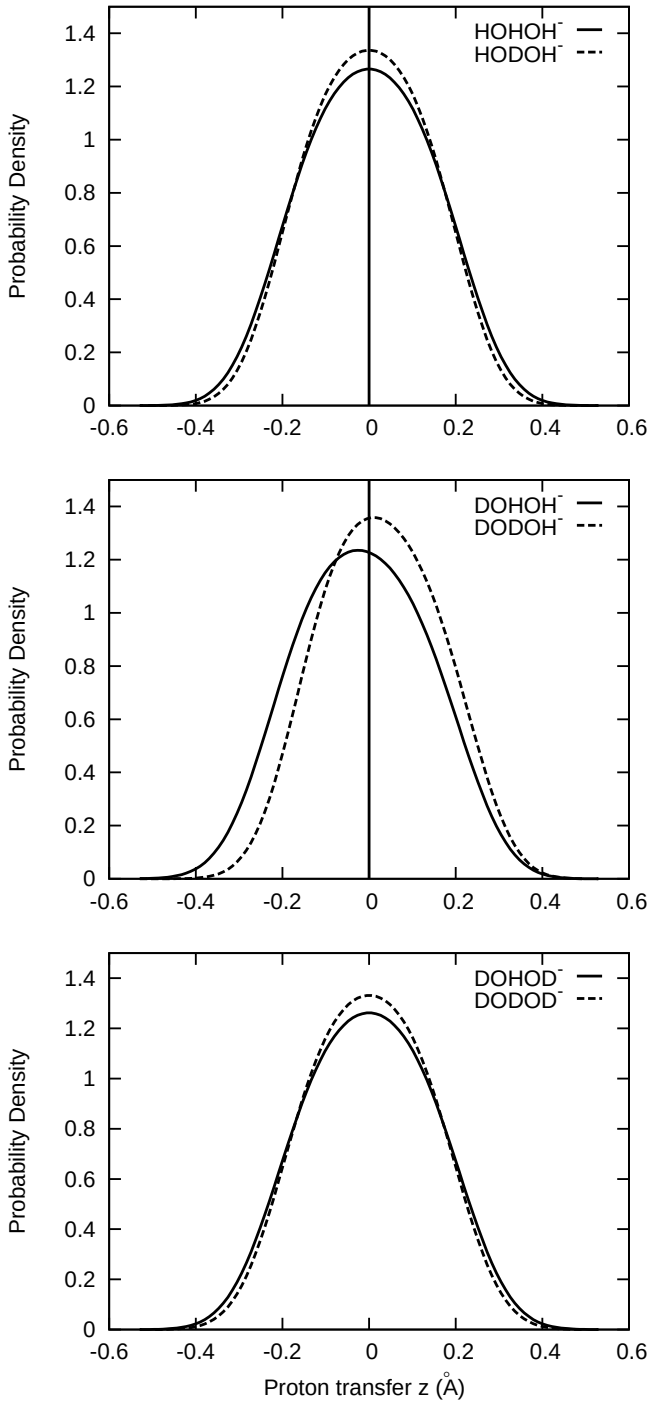

Figure 4.4: Reduced probability density for the vibrational ground states of the different isotopomers along the proton transfer coordinate z. See the text for more details.

Some general features are similar to the $N_2H_7^+$, which have been discussed in Chapter

Table 4.2: Coordinate expectation values and their variances (in Å) for the 9D ground states of the different isotopomers.

	$HOHOH^-$		$HODOH^-$		$DOHOH^-$	
coordinate	mean	variance	mean	variance	mean	variance
R_1	0.981	0.070	0.981	0.070	0.976	0.059
R_2	0.981	0.070	0.981	0.070	0.981	0.070
R_4	2.521	0.063	2.515	0.064	2.536	0.065
u_1	-0.259	0.173	-0.261	0.172	-0.267	0.149
u_2	0.259	0.173	0.261	0.172	0.269	0.174
φ	3.138	1.240	3.136	1.238	2.886	1.258
x	0.000	0.125	0.000	0.107	-0.022	0.126
y	0.000	0.120	0.000	0.104	0.029	0.123
z	0.000	0.150	0.000	0.140	0.029	0.152

2, e.g., the correlation of the ground state density along z and R_4. In this chapter we mainly focus on the isotope effects. Representative cuts of the full 9D ground state vibrational density are shown for the different isotopomers in Fig. 4.4 and Fig. 4.5. More specifically the coordinate expectation values and variances are compiled in Tab. 4.2 and Tab. 4.3.

Fig. 4.4 shows the reduced probability densities along the shared proton coordinate z for different isotopomers. For each symmetric case [X–O$\cdots$Y$\cdots$O–X]$^-$, where X,Y=H or D, the distribution has its single maximum at $z = 0$ as shown in the upper and bottom panels indicating the symmetrization due to zero point vibration with energy above the classical barrier in Fig. 4.3 (a). For each asymmetric case [D–O$\cdots$X$\cdots$O–H]$^-$ the distribution also has single maximum due to the same reason as shown in the middle panel yet it is slightly asymmetric. We have further studied the asymmetry by the geometry of [D–O$\cdots$X$\cdots$O–H]$^-$ and found the O$\cdots$X$\cdots$O angle is slightly different from 180° and the central X atom is closer to the side O–H group instead of O–D since O–D has a shorter

Table 4.3: Coordinate expectation values and their variances (in Å) for the 9D ground states of the different isotopomers.

	$DODOD^-$		$DOHOD^-$		$DODOH^-$	
coordinate	mean	variance	mean	variance	mean	variance
R_1	0.976	0.059	0.976	0.059	0.976	0.059
R_2	0.976	0.059	0.976	0.059	0.981	0.070
R_4	2.544	0.064	2.549	0.064	2.528	0.064
u_1	-0.281	0.148	-0.279	0.148	-0.270	0.146
u_2	-0.281	0.148	0.279	0.148	0.272	0.172
φ	3.139	1.290	3.135	1.293	2.889	1.254
x	0.000	0.120	0.000	0.135	-0.021	0.109
y	0.000	0.104	0.000	0.120	0.028	0.105
z	0.000	0.142	0.000	0.151	-0.027	0.140

bond length leading to a higher repulsion on the central atom.

As expected the width of the distribution narrows upon central H $\rightarrow$ D substitution irrespective whether the side OH groups are deuterated or not as can be seen from all the three panels of z distributions in Fig. 4.4. Inspecting Tab. 4.2 and Tab. 4.3 one finds, that this amounts to $\sim 6\%$ for the z coordinate, but to as much as 13 % for the bridging hydrogen's bending coordinates x and y. The distributions along the other coordinates are much less affected, e.g., the difference for the torsion coordinate φ is not noticeable on the scale of Fig. 4.5 hence only $[X–O\cdots H\cdots O–Y]^-$ cases have been plotted. Similarly the deuteration of the side O–H group also leads to negligible effects on the z distribution on the scale of Fig. 4.4.

The major effects of the side position deuteration are the O-D bond contraction as well as the distribution along the torsion coordinate φ. According to Tab. 4.2 and Tab. 4.3 the free covalent O–H bond length is 0.981 Å while the O–D one is 0.976 Å. The associated bond fluctuation width drops by 15% due to the wider delocalization area of

hydrogen. The reduced density along φ is shown in Fig. 4.5. The distribution has symmetric/asymmetric double peak for symmetric/asymmetric anion. Each side position H $\rightarrow$ D substitution leads to a narrowing of the distribution since the reduced moment of inertia is dominated by the two side O–H/O–D groups.

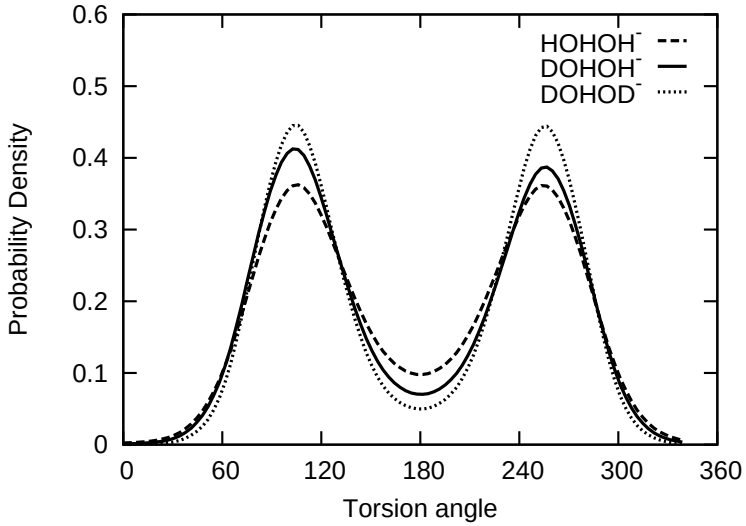

Figure 4.5: Reduced probability density for the vibrational ground states of the different isotopomers along the torsional coordinate φ. See the text for more details.

Apart from the major effects the side position deuteration also causes slight influence on the central H/D atom. As we have discussed above the side O–D group has a higher repulsion than the O–H group. Hence it will narrow the z distribution and expand the x, y distribution like a ball being squeezed into an ellipse. However this secondary effect is not as profound as the primary reduction effect and in some cases almost comparable with our estimated calculation error.

4.3.2 Vibrational Ground State Energy

Now we focus on the ZPEs of the different isotopomers which are analyzed in terms of the contributions of the different parts of the Hamiltonian. The details are compiled in Tab. 4.4. First we notice, that the ZPE of [H–O$\cdots$H$\cdots$O–H]$^-$ is calculated as 6606 cm^{-1}, which essentially reproduces the DMC result (6605$\pm$ 5 cm^{-1}) obtained on the *fully coupled* PES [45]. The set $\boldsymbol{g}_1$ gives the largest contribution to the ZPE as it contains the high frequency OH stretching vibrations. Further, the strongest correlations between different sets of coordinates are those involving the shared proton motion due to its wide delocalization. For the fully deuterated case we obtain 4481 cm^{-1} which is also in accord with the DMC result (4487$\pm$ 5 cm^{-1}).

Table 4.4: Energy expectation values (in cm^{-1}) of the different isotopomers in the vibrational ground state. The subscripts refer to single sets for one set operators or to pairs of sets for the two-set operators, e.g.. $V_{12} = \langle V^{(2)}(\boldsymbol{g}_1, \boldsymbol{g}_2)\rangle$. The three groups are $\boldsymbol{g}_1 = [R_1, R_2, R_4]$, $\boldsymbol{g}_2 = [u_1, u_2, \varphi]$, and $\boldsymbol{g}_3 = [x, y, z]$. Note that the V_0 in Eq. (4.1) is 462 cm^{-1}.

	kinetic energy			potential energy						total
species	T_1	T_2	T_3	V_1	V_2	V_3	V_{12}	V_{13}	V_{23}	T+V
$HOHOH^-$	1995	338	935	1976	425	944	-5	-80	-384	6606
$HODOH^-$	1998	349	647	1960	417	672	-5	-64	-347	6087
$DOHOH^-$	1741	299	940	1731	392	994	-4	-122	-428	6005
$DODOH^-$	1745	309	651	1698	374	685	-5	-68	-368	5483
$DOHOD^-$	1489	259	941	1459	385	1005	-6	-93	-496	5405
$DODOD^-$	1491	268	653	1445	378	740	-6	-83	-467	4881

Next we discuss the general trend in ZPE change upon H/D substitution. Inspecting Table 4.4 we observe that replacing H by D in one of the side O–H groups lowers the ZPE by about 600 cm^{-1} irrespective whether the other site is deuterated or not. Replacing H by D in the bridging site lowers the total ZPE by about 520 cm^{-1} only, again irrespective of the other site's deuteration. The difference is due to the existence of a HB and its bond strength changes when replaced by a deuterium bond. We can describe the effects more explicitly with different channels of the following reaction

$$\mathrm{DOH + OX^- \rightarrow [D\text{–}O\cdots H\cdots O\text{–}X]^- + E_{HB}}$$
$$\mathrm{HOD + OX^- \rightarrow [H\text{–}O\cdots D\cdots O\text{–}X]^- + E_{DB}}$$

where E_{HB} and E_{DB} are hydrogen bond and deuterium bond energies, respectively. Therefore we can conclude that the difference between E_{HB} and E_{DB} is just the ground state energy difference between $[H\text{–}O\cdots D\cdots O\text{–}X]^-$ and $[D\text{–}O\cdots H\cdots O\text{–}X]^-$, i.e., E_{HB}-E_{DB} = 600 cm^{-1} − 520 cm^{-1} = 80 cm^{-1}. In other words, in terms of the ZPE the H-bond is about 80 cm^{-1} stronger than the D-bond in this series of anions.

Let us have a more detailed look at the single substitutions of $[H\text{–}O\cdots H\cdots O\text{–}H]^-$. Here, we find that in terms of ZPE $[D\text{–}O\cdots H\cdots O\text{–}H]^-$ is more stable than [H–

$O\cdots D\cdots O\text{–}H]^-$ by 82 cm^{-1} . First of all, this confirms the qualitative result of Scheiner and coworker [111] who have obtained a value of 52 cm^{-1} based on the harmonic approximation of the PES around a nonsymmetric structure. Their normal mode treatment has led to the conclusion that it is the intramolecular water OH(D) stretching which is responsible for the increased stability of $[D\text{–}O\cdots H\cdots O\text{–}H]^-$. However, as discussed before the structure is symmetrized by ZPE and their analysis in terms of a water molecule hydrogen-bonded to a $OH(D)^-$ is not adequate. Instead, inspecting Tab. 4.4 we find the following behavior: First, ZPE changes in $[D\text{–}O\cdots H\cdots O\text{–}H]^-$ are mainly due to the set $\boldsymbol{g}_1$, i.e. mostly the OH-stretching at the deuteration site since the torsion frequency is so small that its contribution is ignorable, while in $[H\text{–}O\cdots D\cdots O\text{–}H]^-$ it is the set $\boldsymbol{g}_3$ involving the shared proton resulting ZPE changes. We can further notice that the net effect contributed by all the single mode potentials is 37 cm^{-1} by which the D-bond would be more stable whereas the correlation energy difference of -119 cm^{-1} finally leads to the preference for the H-bond.

Now we discuss the general reason for the relative stability of isomers. From the table we can see the dominate parts which leads to the ZPE changes of different isomers are the correlation potential energies. The strength of the correlations between sets of coordinates can be evaluated by the absolute value of corresponding mean correlation potential V_{ij}. The major correlations are those involve the central H/D motion $\boldsymbol{g}_3$ caused by the H/D bond. Tab. 4.4 shows the correlations related to H-bond are larger than the ones related to D-bond. This can be rationalized by the observation that the wave function for the bridging proton is more delocalized than for the deuteron (cf. also Tab. 4.2 and Tab. 4.3) and therefore facilitates stronger couplings to other coordinates by exploring an extended region of the anharmonic PES. This is the fundamental reason why H-bond is more stable than D-bond and can be generalized to other strong hydrogen bonded systems since correlations normally make negative contributions to the total ZPE, i.e., correlations tend to make the total system more stable.

The side position H/D substitution also has certain secondary effects on the correlation energies. Tab. 4.4 shows that the correlations increase upon each deuteration of the side O–H group. As has been discussed in Section 4.3.1, the side position deuteration makes the effective volume of the single anion more compressed therefore the coupling increases.

4.3.3 Secondary Geometric Isotope Effects

Having at hand the ground state wave functions we can calculate the secondary GIEs, i.e., the change of $O\cdots O$ distance upon isotopic substitution. Note that R_4 does not fully

correspond to the O$\cdots$O distance $R_{\mathrm{O-O}}$ (cf. Fig. 4.1). The corresponding operator for $R_{\mathrm{O-O}}$ can be expressed in terms of our model coordinates

$$\hat{R}_{\mathrm{O-O}} = \sqrt{(R_4 + \eta_1 R_1 u_1 - \eta_2 R_2 u_2)^2 + d^2(\eta_1 R_1\sqrt{1-u_1^2}, \eta_2 R_2\sqrt{1-u_2^2}, \varphi)}$$
$$d^2(x, y, \varphi) = x^2 + y^2 - 2xy\cos\varphi, \tag{4.2}$$

where $\eta_i = m_{\mathrm{D,H}}/(m_{\mathrm{D,H}} + m_{\mathrm{O}})$ depends on whether the corresponding side O–H group is deuterated or not. Since we have obtained the ground state wave function and the operator we can directly calculate the expectation value by integration $< R_{\mathrm{O-O}} >= \langle\Psi_0|\hat{R}_{\mathrm{O-O}}|\Psi_0\rangle$.

Table 4.5: Expectation values for the O$\cdots$O distance (in Å) and reductions for deuteration of bridging site for the different isotopomers. The classical value at the transition state is 2.446Å.

case	$\langle R_{\mathrm{O-O}}\rangle$	case	$\langle R_{\mathrm{O-O}}\rangle$	case	$\langle R_{\mathrm{O-O}}\rangle$
$HOHOH^-$	2.492	$DOHOH^-$	2.495	$DOHOD^-$	2.493
$HODOH^-$	2.487	$DODOH^-$	2.486	$DODOD^-$	2.488

The resulting expectation values for the different isotopomers are compiled in Tab. 4.5. The classical value for $R_{\mathrm{O-O}}$ in [H–O$\cdots$H$\cdots$O–H]$^-$ at the MP2/aug-cc-pVTZ transition state is 2.446 Å. In the quantum case this value increases to 2.492 Å as a consequence of zero-point vibration. This value is reduced to 2.487 Å for deuteration of the bridging site, i.e. in the [H–O$\cdots$D$\cdots$O–H]$^-$ case. In all cases the deuteration of the bridging site leads to a reduction of the O$\cdots$O distance. For the symmetric cases the reduction is about 0.005 Å while for the asymmetric case it is 0.009 Å. Such a bond compression due to reduced zero-point vibration, i.e., localization of the wave function, is typical for strong hydrogen bonds.

The trends of the reduction of $R_{\mathrm{O-O}}$ upon bridging site deuteration are in good agreement with the DMC calculations in Ref. [45] for $H_3O_2^-$ and $D_3O_2^-$, only the absolute values of the DMC $R_{\mathrm{O-O}}$ are larger by 0.005 Å. In passing we note that the fully deuterated case has also been investigated using the finite temperature path integral method at a lower level of quantum chemistry [113]. For this situation Tachikawa and coworker obtained 2.498 Å for $H_3O_2^-$ and 2.504 Å for $D_3O_2^-$, that is, the opposite trend which has been explained by the bimodal character of the calculated distribution for $D_3O_2^-$ caused by the influence of the environment at finite temperature.

4.3.4 Torsional Tunneling Splittings

As has been mentioned above there will be a tunneling splitting due to the side O–H group torsional motion via the transition state overcoming the appropriately high potential barrier along the torsion coordinate φ. That is to say the ground state wave function is symmetric while the upper splitting state wave function is antisymmetric with respect to the torsion coordinate φ. This wave function can be obtained by improved relaxation embedded in the MCTDH package. We first do this improved relaxation for [H–O$\cdots$H$\cdots$O–H]$^-$ with an initial wave function as a product of the ground state wave function and $\sin\varphi$. The converged result of upper splitting state is then taken as initial wave function for the improved relaxations of the other isotopomers. The final results of the tunneling splitting energy Δ of different isotopomers are compiled in Table 4.6. The non-deuterated and fully deuterated cases have been investigated by different methods [45, 46]. Our results agree reasonably with the existing investigations.

Table 4.6: Energy splitting Δ of the lowest pair of eigenstates (in cm^{-1}) for different isotopomers.

case	Δ	case	Δ	case	Δ
HOHOH$^-$	18.8	DOHOH$^-$	13.0	DOHOD$^-$	5.8
HODOH$^-$	18.7	DODOH$^-$	11.7	DODOD$^-$	4.2

As expected the side position deuteration increases the reduced inertia of moment consequently decreases the torsional frequency, which can be reflected from the energy splitting. Upon each side position deuteration the energy splitting decreases by 6-7 cm^{-1}. As has been discussed in Section 4.3.1, the bridging site H/D substitution almost has no effect on the torsion wave function. Therefore it should not affect the tunneling splitting, either. It should be mentioned that it is sometimes difficult for the the improved relaxation method to converge exactly to the desired wave functions and consequently larger errors may exist as compared with the ground state calculations. From this point, Table 4.6 can also be used to estimate the energetic error of our calculation. According to the differences, the total error is less than 2 cm^{-1} therefore the ground state energy error should be less than 1 cm^{-1}.

4.4 Summary

The mono-hydrated hydroxide anion is a prototype strongly hydrogen-bonded low-barrier system whose structure is symmetrized by zero-point vibration. An accurate theoretical prediction of the associated ground state wave function requires to treat the dynamical problem in full-dimensionality. Using the CCSD(T) potential energy surface of Bowman and coworkers [45] we have shown that the MCTDH approach for wave packet propagation [90] can meet this challenge. For the four partly deuterated isotopomers, this work is the first full dimensional quantum investigation.

Comparing the vibrational ground state wave functions and ZPEs for different isotopomers several important conclusions can be drawn. First, in accord with the general view for ions, bridging donor and acceptor by a hydrogen atom is more favorable than bridging by a deuterium. The general trend for the considered systems is that in terms of ZPE the H-bonds are about 80 cm^{-1} ($\sim$1 kJ/mol) more stable than the D-bonds, irrespective the deuteration state of the O–H groups. Specifically, we find [D–O$\cdots$H$\cdots$O–H]$^-$ is energetically more stable than [H–O$\cdots$D$\cdots$O–H]$^-$ by 82 cm^{-1}. Although this seems merely to confirm the results of the harmonic analysis reported in Ref. [111], the present full-dimensional treatment is providing a more realistic physical picture by accounting not only for the symmetrization of the structure due to zero point motion but also for the anharmonicity of the potential energy surface. It is not only the loss of an intra-molecular OH vibration of the water molecule which reduces the ZPE more than the loss of the intermolecular bridging hydrogen vibration as argued in Ref. [111] from the perspective of harmonic vibrations. In fact we find that correlations between the bridging H/D atom motion and the other coordinates predominate the change of ZPEs. The fundamental reason why the H-bond is about 80 cm^{-1} more stable than D-bond is that the proton distribution is more delocalized consequently leading to larger correlations.

The second result concerns the H/D isotope effect on the heavy atoms O$\cdots$O distance. Here, we find that as compared with the classical prediction, zero-point vibrational motion of the bridging nucleus increases $R_{\mathrm{O-O}}$ for all the isotopomers. Each H-bonded isotopomer has a slightly longer $R_{\mathrm{O-O}}$ distance than the D-bonded one due to the fact that proton distribution is more delocalized than the deuteron distribution. The corresponding $R_{\mathrm{O-O}}$ distance reduction due to bridging site deuteration is about 0.005 Å for the symmetric cases and 0.009 Å for the asymmetric cases. Apart from these we have further investigated the small tunneling splitting due to the torsional motion via the transition state. The energy splitting for [H–O$\cdots$H$\cdots$O–H]$^-$ is 18.8 cm^{-1} and decreases by 6-7 cm^{-1} upon each side position deuteration. The results for the O$\cdots$O distance and tor-

sional tunneling splitting agree with previous investigations for $H_3O_2^-$ and $D_3O_2^-$ [45, 46].

In this and previous chapters we have demonstrated the multidimensional quantum dynamics as an appropriate level of theory for strong hydrogen bonded systems. However quantum dynamics is only possible for gas phase study of small systems as far as present computing ability is concerned. Though gas phase investigations provide us clear pictures of even fundamental processes as well as key features of condensed phase phenomena, it is still quite necessary to accomplish condensed phase studies which directly relate to many experiments. In the next chapter we will provide a condensed phase study of the hydrogen transfer reaction rate constant.

Chapter 5

Hydrogen Transfer Kinetics in the Condensed Phase

5.1 Motivation and Introduction

Unlike the gas phase study which can provide quantitative analysis not only well interpreting the related experiments but also throwing light on the condensed phase phenomena, normally the condensed phase study can only provide qualitative explanations since only the key part of the Hamiltonian is treated at the $ab\,initio$ level. However, this kind of study is quite important as most experiments have to be accomplished in condensed phase. In addition a good simulation also enables the experimentalist to adjust certain parameters to the range where interesting effects are predicted. Essential progress has been made in condensed phase studies yet lots of challenges still remain including theoretical method development.

Condensed phase hydrogen transfer is the most common reaction even in our daily life. Since the proton is the lightest nucleus it has much in common with the electron concerning the transfer rate constant. However, we do not have a general theory to describe the proton transfer rate like the famous Marcus theory [114] in the electron transfer counterpart. Though intensive studies have been done both experimentally and theoretically [2, 8] there are still open questions concerning even the mechanism.

Fig. 5.1 shows a very recent NMR experiment by Limbach group concerning the KIEs of tautomerism of 6-Aminofulvene-1-aldimine molecule [115]. The KIEs at 298 K has been reported to be $k_{12}^H/k_{12}^D = 9$ for crystalline and 4 for amorphous environment. The temperature dependence of the rate constant shows the Arrhenius behavior in the high temperature region indicating the predominated mechanism for hydrogen/deuterium transfer is the thermal activation. The ratio of the thermal activation energies is about

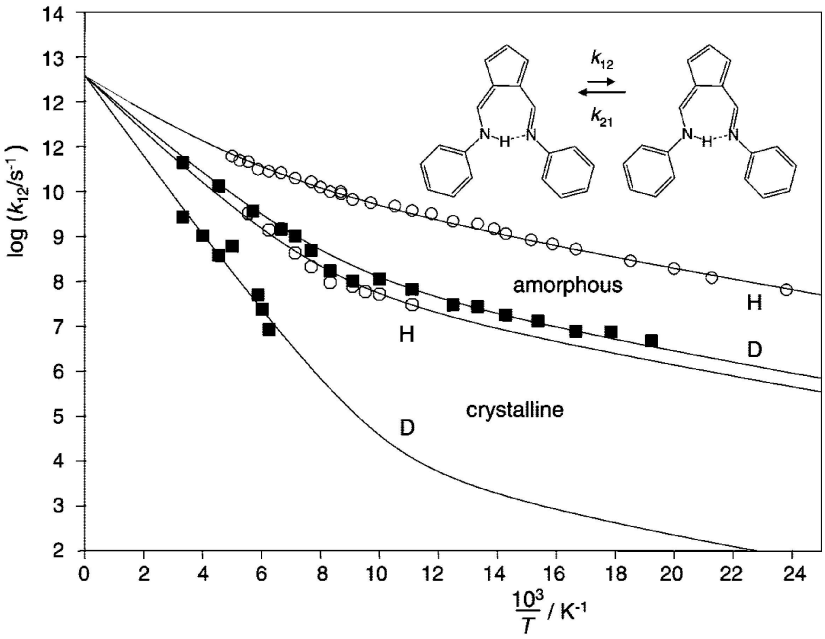

Figure 5.1: The KIEs for the tautomerism of 6-Aminofulvene-1-aldimine. The experimental curves are measured in both amorphous and crystalline environment, adapted from Ref. [115].

$E_a^H/E_a^D = 2/3$, almost irrespective of environment. In the low temperature region the temperature dependence is flattened due to increasing quantum tunneling effects. Two

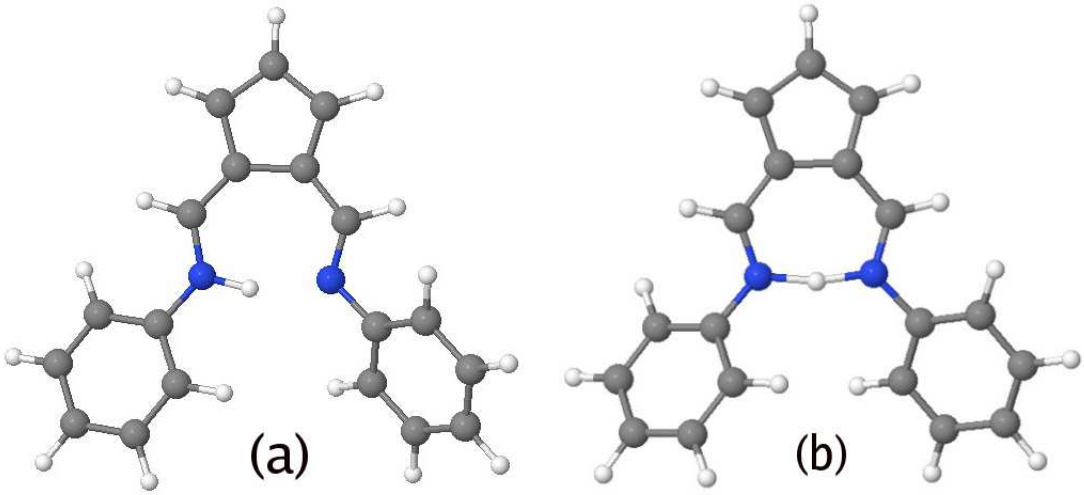

Figure 5.2: (a) Minimum configuration. (b) Transition state for the hydrogen atom transfer. The blue ones are nitrogen atoms.

equilibrium configurations obtained by B3LYP/6-31+G(d,p) optimization are shown in Fig. 5.2. The minimum configuration corresponds to the reactant or product. The hydrogen atom transfer process can take place from the reactant via the transition state to the

product or inversely. The reaction barrier height as calculated by the energy difference of the minimum and the transition state is 3.84 kcal/mol at the B3LYP/6-31+G(d,p) level of theory. In general the real activation energy will be decreased by the influence of the environment as compared to the gas phase reaction barrier.

In the case of high barrier reaction processes, the classical transition state theory [58] can make good predictions of the thermal activation energy. While a uniform quantum theory for the reaction rates [59, 116, 117] is expected to explain both high- and low-temperature behaviors. In this chapter we will develop a general theory of reaction surface Hamiltonian and reaction rate constant calculations based on it. Then we perform a preliminary study based on a model 1D reaction path Hamiltonian for 6-Aminofulvene-1-aldimine.

5.2 Theory

5.2.1 Reaction Surface Hamiltonian

The reaction surface Hamiltonian contains many small amplitude displacements $\{Q_k\}$ and several large amplitude coordinates $\{s_\alpha\}$ [63, 66, 67]. The latter ones form the so called reaction surface. To generate this Hamiltonian from the exact Cartesian coordinate Hamiltonian we can directly exploit the method developed in Chapter 2.

Suppose we have the Cartesian Hamiltonian

$$\begin{aligned} H\left(\boldsymbol{R}\right) &= T\left(\boldsymbol{R}\right)+V\left(\boldsymbol{R}\right) \\ T\left(\boldsymbol{R}\right) &= \frac{1}{2}\boldsymbol{P}^2=-\frac{\hbar^2}{2}\frac{\partial^2}{\partial\boldsymbol{R}^2}, \end{aligned} \tag{5.1}$$

where $\boldsymbol{R}$ is the $3N$ dimensional vector of mass weighted Cartesian coordinates for system with N atoms and $\boldsymbol{P}=-i\hbar\frac{\partial}{\partial\boldsymbol{R}}$ is the corresponding linear momentum vector. In this Chapter all the operators are quantum mechanical ones and the "hat" notations are omitted. Suppose it is feasible to find a reaction surface defined by a one-to-one mapping along the reaction coordinates $\boldsymbol{s}$

$$\boldsymbol{R}=\boldsymbol{R_0}\left(\boldsymbol{s}\right). \tag{5.2}$$

The potential energy function $V\left(\boldsymbol{R}\right)$ can be expanded around the reaction surface

$$V\left(\boldsymbol{R}\right)=V\left(\boldsymbol{R_0}\right)+\Delta\boldsymbol{R}(\boldsymbol{s})^T\frac{\partial V}{\partial\boldsymbol{R}}|_{\boldsymbol{R_0}}+\frac{1}{2}\Delta\boldsymbol{R}(\boldsymbol{s})^T\frac{\partial^2V}{\partial\boldsymbol{R}^2}|_{\boldsymbol{R_0}}\Delta\boldsymbol{R}(\boldsymbol{s})+\cdots, \tag{5.3}$$

where $\Delta\boldsymbol{R}\left(\boldsymbol{s}\right)=\boldsymbol{R}-\boldsymbol{R_0}\left(\boldsymbol{s}\right)$ and the superscript ^{T} means transpose. The reaction surface is defined in such a way that the potential energy $V\left(\boldsymbol{R}\right)$ can be approximated within low orders of orthogonal displacements, i.e., Eq. (5.3) can be truncated in the given form.

To obtain the reaction surface Hamiltonian we first need to define the new coordinates, i.e., the reaction coordinates $\{s_\alpha\}$ and the orthogonal displacements $\{Q_k\}$. The former are already defined by the reaction surface as well as the unit vectors $\{\boldsymbol{e}_\alpha(\boldsymbol{s})\}$ according to which we have the reaction coordinate vector

$$\boldsymbol{s} = \sum_{\alpha=1}^{D} s_\alpha \boldsymbol{e}_\alpha. \tag{5.4}$$

To get the latter we need a projection operator to project out the reaction coordinate $\boldsymbol{s}$

$$\mathbf{P}(\boldsymbol{s}) = 1 - \sum_\alpha \boldsymbol{e}_\alpha \boldsymbol{e}_\alpha^T. \tag{5.5}$$

Then we can diagonalize the projected Hessian matrix $\mathbf{K}(\boldsymbol{s})$ for each point of the reaction surface by an orthogonal transformation $\mathbf{U}_{RS}(\boldsymbol{s})$

$$\mathbf{U}_{RS}(\boldsymbol{s})^\dagger \mathbf{K}(\boldsymbol{s}) \mathbf{U}_{RS}(\boldsymbol{s}) = \mathrm{diag}\{\cdots \omega_\alpha^2(\boldsymbol{s}) \cdots \omega_g^2(\boldsymbol{s}) \cdots \omega_k^2(\boldsymbol{s}) \cdots\}, \tag{5.6}$$

where $\mathbf{K}(\boldsymbol{s}) = \mathbf{P}(\boldsymbol{s}) \frac{\partial^2 V}{\partial \boldsymbol{R}^2}|_{\boldsymbol{R_0}} \mathbf{P}(\boldsymbol{s})$ is real symmetric.

In total there are $D+6$ zero eigenvalues $\{\omega_\alpha^2\}$ and $\{\omega_g^2\}$ corresponding to the reaction coordinates and six dimensional global translation and rotation, respectively

$$\begin{aligned} \omega_\alpha^2 &= 0, \alpha = 1, \cdots, D \\ \omega_g^2 &= 0, g = 1, \cdots, 6 \end{aligned} \tag{5.7}$$

The orthogonal transformation matrix contains the corresponding eigenvectors of $\mathbf{K}(\boldsymbol{s})$

$$\mathbf{U}_{RS}(\boldsymbol{s}) = (\cdots \boldsymbol{e}_\alpha(\boldsymbol{s}) \cdots \boldsymbol{e}_g(\boldsymbol{s}) \cdots \boldsymbol{e}_k(\boldsymbol{s}) \cdots). \tag{5.8}$$

The six dimensional global translation and rotation as well as the $3N-6-D$ displacements orthogonal to the reaction surface are defined by

$$\begin{aligned} R_g &= \boldsymbol{e}_g^T \Delta \boldsymbol{R} \\ Q_k &= \boldsymbol{e}_k^T \Delta \boldsymbol{R}. \end{aligned} \tag{5.9}$$

The original $3N$ dimensional vector is now expressed with the new unit vectors

$$\boldsymbol{R} = \boldsymbol{R}_{ref} + \sum_\alpha s_\alpha \boldsymbol{e}_\alpha + \sum_g R_g \boldsymbol{e}_g + \sum_k Q_k \boldsymbol{e}_k, \tag{5.10}$$

where the reference geometry $\boldsymbol{R}_{ref} = \boldsymbol{R_0}(\boldsymbol{s}=0)$ is the origin of the new coordinates system.

Based on the knowledge of the new coordinates it is not difficult to find the potential energy

$$V(\boldsymbol{s}, \boldsymbol{Q}) = V[\boldsymbol{R_0}(\boldsymbol{s})] - \sum_k f_k(\boldsymbol{s}) Q_k + \frac{1}{2} \sum_k \omega_k(\boldsymbol{s})^2 Q_k^2, \tag{5.11}$$

where $f_k(\boldsymbol{s}) = -\boldsymbol{e}_k^T \frac{\partial V}{\partial \boldsymbol{R}} | \boldsymbol{R_0}$.

It is obvious that the potential energy does not depend on $\{\boldsymbol{R_g}\}$, however, the KEO does depend on $\{\boldsymbol{R_g}\}$ and normally it is not possible to exactly separate them. Using the method in Chapter 2 (See Eq. (2.6), note in this case the mass matrix is a unit matrix) the following formal KEO can be obtained

$$T = \frac{1}{2} \boldsymbol{P}^{\dagger}_{\tilde{\boldsymbol{R}}} \frac{\partial \tilde{\boldsymbol{R}}}{\partial \boldsymbol{R}} \left(\frac{\partial \tilde{\boldsymbol{R}}}{\partial \boldsymbol{R}} \right)^T \boldsymbol{P}_{\tilde{\boldsymbol{R}}}, \tag{5.12}$$

where $\tilde{\boldsymbol{R}}^T = \begin{pmatrix} \boldsymbol{s}^T & \boldsymbol{R_g}^T & \boldsymbol{Q}^T \end{pmatrix}$ is the full set of the new coordinates and $\boldsymbol{P}_{\tilde{\boldsymbol{R}}} = -i\hbar \frac{\partial}{\partial \tilde{\boldsymbol{R}}}$. According to Appendix A one can find out that all the other components of $\boldsymbol{P}_{\tilde{\boldsymbol{R}}}$ are Hermitian due to the orthogonality of transformation except $\boldsymbol{P_s}$. Eq. (5.12) has a fully coupled form in case the reaction surface is quite arbitrary. The only factor which makes the complexity is that all the unit vectors depend on $\boldsymbol{s}$, i.e., the orthogonal transformation matrix $\mathbf{U}(\boldsymbol{s})$ depends on $\boldsymbol{s}$ thus we have to calculate the derivatives with respect to $\boldsymbol{s}$.

5.2.2 Linear Reaction Surface Hamiltonian

As mentioned in the last section the reaction surface Hamiltonian has a diagonal potential energy function but a quite complicated KEO. The most natural thing will be to transform to another representation provided we do not want to treat such a complicated KEO directly. The linear reaction surface Hamiltonian exploit constant unit vectors to describe the reaction coordinates $\boldsymbol{s}$ thus greatly decrease the complexity of the KEO. With the help of certain predefined constant unit vectors $\{\boldsymbol{e}_\alpha\}$ we can easily obtain the equation for the linear reaction surface

$$\boldsymbol{R_0}(\boldsymbol{s}) = \boldsymbol{R}_{ref} + \sum_\alpha s_\alpha \boldsymbol{e}_\alpha. \tag{5.13}$$

The coordinates transform relations can be obtained by the same procedure mentioned in the last section

$$\begin{aligned} \boldsymbol{R} &= \boldsymbol{R_0}(\boldsymbol{s}) + \sum_k Q_k \boldsymbol{e}_k = \boldsymbol{R}_{ref} + \sum_\alpha s_\alpha \boldsymbol{e}_\alpha + \sum_k Q_k \boldsymbol{e}_k \\ s_\alpha &= \boldsymbol{e}_\alpha^T \Delta \boldsymbol{R}, \qquad Q_k = \boldsymbol{e}_k^T \Delta \boldsymbol{R}, \end{aligned} \tag{5.14}$$

where $\Delta \boldsymbol{R} = \boldsymbol{R} - \boldsymbol{R}_{ref}$ is different from $\Delta \boldsymbol{R}(\boldsymbol{s})$ in Eq. (5.3) while $\{Q_k\}$ and $\{\boldsymbol{e}_k(\boldsymbol{s})\}$ have the same definition as in the last section. Please note here we have combined the $\{R_g\}$ and $\{Q_k\}$ into the same set of indexes $\{Q_k\}$ to simplify the notation. With the help of Eq. (5.12) and Eq. (5.14) we can derive the much more simplified KEO for a linear reaction surface. We will do it in the following explicitly.

We first calculate the elements of the needed Jacobi matrices starting from Eq. (5.14). Remember that $\{\boldsymbol{e}_k(\boldsymbol{s})\}$ actually depends on $\boldsymbol{s}$. Using the normal chain rule to calculate the derevatives from Eq. (5.14) leads to the following results

$$\begin{aligned}\frac{\partial s_\alpha}{\partial \boldsymbol{R}} &= \boldsymbol{e}_\alpha^T \\ \frac{\partial Q_k}{\partial \boldsymbol{R}} &= \boldsymbol{e}_k^T + \sum_\alpha \boldsymbol{e}_\alpha^T \left(\Delta \boldsymbol{R}^T \frac{\partial \boldsymbol{e}_k}{\partial s_\alpha}\right).\end{aligned} \tag{5.15}$$

Thus the elements for the matrix product can be obtained

$$\begin{aligned}\left(\frac{\partial \boldsymbol{s}}{\partial \boldsymbol{R}}\left(\frac{\partial \boldsymbol{s}}{\partial \boldsymbol{R}}\right)^T\right)_{\alpha\beta} &= \boldsymbol{e}_\alpha^T \boldsymbol{e}_\beta = \delta_{\alpha\beta} \\ \left(\frac{\partial \boldsymbol{s}}{\partial \boldsymbol{R}}\left(\frac{\partial \boldsymbol{Q}}{\partial \boldsymbol{R}}\right)^T\right)_{\alpha k} &= \boldsymbol{e}_\alpha^T \left(\boldsymbol{e}_k + \sum_\beta \boldsymbol{e}_\beta \left(\Delta \boldsymbol{R}^T \frac{\partial \boldsymbol{e}_k}{\partial s_\beta}\right)\right) = \Delta \boldsymbol{R}^T \frac{\partial \boldsymbol{e}_k}{\partial s_\alpha} \\ \left(\frac{\partial \boldsymbol{Q}}{\partial \boldsymbol{R}}\left(\frac{\partial \boldsymbol{Q}}{\partial \boldsymbol{R}}\right)^T\right)_{kk'} &= \delta_{kk'} + \sum_\alpha \left(\Delta \boldsymbol{R}^T \frac{\partial \boldsymbol{e}_k}{\partial s_\alpha}\right)\left(\Delta \boldsymbol{R}^T \frac{\partial \boldsymbol{e}_{k'}}{\partial s_\alpha}\right).\end{aligned} \tag{5.16}$$

Based on above equations we can simplify the Eq. (5.12) as

$$\begin{aligned}T(\boldsymbol{s}, \boldsymbol{Q}) &= \frac{1}{2}\sum_\alpha P_\alpha^2 + \frac{1}{2}\sum_{kk'} P_k^\dagger \left(\delta_{kk'} + \sum_\alpha B_{\alpha k} B_{\alpha k'}\right) P_{k'} \\ &\quad + \left(\frac{1}{2} P_\alpha \sum_{\alpha k} B_{\alpha k} P_k + h.c.\right),\end{aligned} \tag{5.17}$$

where $B_{\alpha k} = \Delta \boldsymbol{R}^T \frac{\partial \boldsymbol{e}_k}{\partial s_\alpha}$ and $h.c.$ means Hermitian conjugate. Note here all the components of momentum are Hermitian according to Appendix A. The kinetic couplings are caused by the $\boldsymbol{s}$ dependence of $\{\boldsymbol{e}_k\}$ as can be seen from the expression of $B_{\alpha k}$. The potential energy has the same expansion as Eq. (5.11). This expression is essentially the same with the one in Ref. [116].

The KEO can be further simplified by using more constant unit vectors to expand the new coordinate space, i.e., we get rid of the $\boldsymbol{s}$ dependence of $\{\boldsymbol{e}_k\}$. The most simple case, in which the kinetic energy has a quite trivial form while the potential energy is no longer diagonal, is the space whose unit vectors are all constants. This can be achieved by diagonalizing the projected Hessian matrix on only one point $\boldsymbol{R}_{ref}$ instead of on each point on the reaction surface. The new representation is obtained by a pure $\boldsymbol{s}$ independent rotation and the new variables are defined by

$$\begin{aligned}s_\alpha &= \boldsymbol{e}_\alpha^T (\boldsymbol{R} - \boldsymbol{R}_{ref}) \\ Q_k &= \boldsymbol{e}_k^T (\boldsymbol{R} - \boldsymbol{R}_{ref}).\end{aligned} \tag{5.18}$$

Here $\{Q_k\}$ denote all the rest $3N-D$ variables which are the global translation, rotation and normal modes only at the reference point but have no meaning at the other points when $\boldsymbol{s} \neq 0$. Note the difference is that all the unit vectors are constant vectors defined by the reference geometry $\boldsymbol{R}_{ref}$. The Hamiltonian in terms of the new coordinates reads

$$\begin{aligned} T(\boldsymbol{s},\boldsymbol{Q}) &= \frac{1}{2}\sum_{\alpha} P_{\alpha}^2 + \frac{1}{2}\sum_{k} P_k^2 \\ &= -\frac{\hbar^2}{2}\sum_{\alpha}\frac{\partial^2}{\partial s_{\alpha}^2} - \frac{\hbar^2}{2}\sum_{k}\frac{\partial^2}{\partial Q_k^2} \\ V(\boldsymbol{s},\boldsymbol{Q}) &= V(\boldsymbol{R_0}) - \sum_{k} f_k(\boldsymbol{s})\, Q_k + \frac{1}{2}\sum_{k,k'} \Omega_{k,k'}(\boldsymbol{s})\, Q_k Q_{k'}, \end{aligned} \tag{5.19}$$

where f_k has the same definition as before and $\Omega_{k,k'}(\boldsymbol{s}) = \boldsymbol{e}_k^T \frac{\partial^2 V}{\partial \boldsymbol{R}^2}|_{\boldsymbol{R_0}} \boldsymbol{e}_{k'}$. In Ref. [116] a method to separate the translation and rotational DOFs is also introduced. For approximate separations one can also refer to the procedure how we get the KEO for $H_3O_2^-$ in Chapter 4. Our further investigations start from this Hamiltonian. It should be mentioned that start from Eq. (5.17) is also feasible, where the off-diagonal parts of the KEO can be treated analytically and the potential energy is diagonal which may be more convenient for numerical investigation.

5.2.3 Reaction Rate Constant Theory

The reaction rate constant k_{PR} can be obtained by integrating over the flux-flux autocorrelation function $C_f(t)$ according to previous studies [59, 60, 117, 118]. We will only give the main formulas in the following

$$\begin{aligned} k_{PR} &= \frac{1}{Z}\int_0^{\infty} C_f(t)dt \\ C_f(t) &= \mathrm{Tr}\left\{F e^{iHt_c^*/\hbar} F e^{-iHt_c/\hbar}\right\}, \end{aligned} \tag{5.20}$$

where $Z = \mathrm{Tr}\left(-\beta H_{reac}\right)$ is the canonical partition function of the reactant Hamiltonian and $F = \frac{1}{2m}\left(p_s\delta(s) + \delta(s)p_s\right)$ is the symmetrized 1D flux operator for the special case of 1D reaction path. The complex time $t_c = t - i\hbar\beta/2$ is due to the combination of the evolution operator and the Boltzmann operator with $\beta = \frac{1}{K_B T}$. Their key point is to define a 1D flux operator which can identify the direction of the momentum consequently whether the momentum contributes to the reactant or the product. The trace is over the full Hamiltonian but the flux-flux correlation operator will gets rid of the flux which reflect back to the reactant.

The flux correlation function can be calculated by second order finite difference of a

certain generating function [117, 118] $K(s_1, s_{N+1}, s_{N+2}, s_{2N+2})$

$$C_f(t_c) = \frac{\hbar^2}{2m^2\Delta s^2}\mathrm{Re}\left[K(\Delta s, \Delta s, 0, 0, t_c) - K(0, \Delta s, 0, \Delta s, t_c)\right], \tag{5.21}$$

where

$K(s_1, s_{N+1}, s_{N+2}, s_{2N+2}) = \int_{-\infty}^{\infty} d\boldsymbol{Q}\langle\boldsymbol{Q}|\langle s_{2N+2}|e^{iHt_c^*/\hbar}|s_{N+2}\rangle\langle s_{N+1}|e^{-iHt_c}/\hbar|s_1\rangle|\boldsymbol{Q}\rangle.$

The path integral technique which divides the complex time t_c into N slices is adopted to calculate this generating function [117, 118]

$$\begin{aligned}
& K(s_1, s_{N+1}, s_{N+2}, s_{2N+2}) \\
= & \int_{-\infty}^{\infty}\cdots\int_{-\infty}^{\infty} d\boldsymbol{Q}ds_2\cdots ds_N ds_{N+3}\cdots ds_{2N+1} \\
& \times\langle\boldsymbol{Q}|\prod_{n=2N+1}^{N+2}\langle s_{n+1}|e^{-iH(s)\delta_n}|s_n\rangle\prod_{n=N}^{1}\langle s_{n+1}|e^{-iH(s)\delta_n}|s_n\rangle|\boldsymbol{Q}\rangle \\
= & \int_{-\infty}^{\infty}\cdots\int_{-\infty}^{\infty} ds_2\cdots ds_N ds_{N+3}\cdots ds_{2N+1}F_t(s_1, s_2, \cdots, s_{2N+2}, t_c) \\
& \times\prod_{n=2N+1}^{N+2}\langle s_{n+1}|e^{-iH_0(s)\delta_n}|s_n\rangle\prod_{n=N}^{1}\langle s_{n+1}|e^{-iH_0(s)\delta_n}|s_n\rangle,
\end{aligned} \tag{5.22}$$

where the time steps $\{\delta_n\}$ are defined as follows:

$$\begin{aligned}
\delta_{2N+2} &= \delta_{N+2} = \frac{-t_c^*}{2N\hbar} \\
\delta_n &= \frac{-t_c^*}{N\hbar}, n = N+3, \cdots, 2N+1 \\
\delta_{N+1} &= \delta_1 = \frac{t_c}{2N\hbar} \\
\delta_n &= \frac{t_c}{N\hbar}, n = 2, \cdots, N.
\end{aligned} \tag{5.23}$$

The expression F_t is called influence functional which is defined as

$$F_t(s_1, s_2, \cdots, s_{2N+2}, t_c) = \int_{-\infty}^{\infty} d\boldsymbol{Q}\langle\boldsymbol{Q}|\prod_{n=2N+2}^{1} e^{-iH_1(s_n, \boldsymbol{Q})\delta_n}|\boldsymbol{Q}\rangle, \tag{5.24}$$

where $H_1 = H - H_0$ and $H_0 = -\frac{\hbar^2}{2}\frac{\partial^2}{\partial s^2} + V(\boldsymbol{R_0})$ is the zeroth order reaction path Hamiltonian. The partition function can be calculated following the same idea detailed above

$$\begin{aligned}
Z = & \int_{-\infty}^{\infty}\cdots\int_{-\infty}^{\infty} ds_1 ds_2\cdots ds_{N_\beta}F_\beta(s_1, s_2, \cdots, s_{N_\beta}) \\
& \times\langle s_1|e^{-iH_0(s)\delta_\beta}|s_{N_\beta}\rangle\prod_{n=N_\beta-1}^{1}\langle s_{n+1}|e^{-iH_0(s)\delta_\beta}|s_n\rangle
\end{aligned}$$

$$F_\beta(s_1, s_2, \cdots, s_{N_\beta}) = \int_{-\infty}^{\infty} d\boldsymbol{Q}\langle\boldsymbol{Q}|\prod_{n=N_\beta}^{1} e^{-iH_1(s_n, \boldsymbol{Q})\delta_\beta}|\boldsymbol{Q}\rangle, \tag{5.25}$$

where $\delta_\beta = -\frac{i\beta}{N_\beta}$ and N_β is the number of time slices for the imaginary time $-i\hbar\beta$.

In both cases we need to calculate the influence functionals which have the same form, namely

$$\begin{aligned} F_{infl}\left(\boldsymbol{s},\boldsymbol{\delta}\right) &= \int_{-\infty}^{\infty} d\boldsymbol{Q}\langle\boldsymbol{Q}|\prod_{n=N}^{1} e^{-iH_1\left(s_n,\boldsymbol{Q}\right)\delta_n}|\boldsymbol{Q}\rangle \\ &= \int_{-\infty}^{\infty}\cdots\int_{-\infty}^{\infty} d\boldsymbol{Q}_1 d\boldsymbol{Q}_2\cdots d\boldsymbol{Q}_N\langle\boldsymbol{Q}_1|e^{-iH_1(s_N,\boldsymbol{Q})\delta_N}|\boldsymbol{Q}_N\rangle \\ &\quad\times\prod_{n=N-1}^{1}\langle\boldsymbol{Q}_{n+1}|e^{-iH_1(s_n,\boldsymbol{Q})\delta_n}|\boldsymbol{Q}_n\rangle. \end{aligned} \tag{5.26}$$

The short time propagator of H_1 can be calculated by splitting H_1 into the harmonic part and perturbation part

$$\begin{aligned} H_1(s_n) &= \frac{1}{2}\sum_k\left(P_k^2+\omega_k Q_{nk}^2\right)+\Delta V_1(s_n,\boldsymbol{Q}_n) \\ \Delta V_1(s_n,\boldsymbol{Q}_n) &= V_1(s_n,\boldsymbol{Q}_n)-V_{har}(\boldsymbol{Q}_n)=V_1(s_n,\boldsymbol{Q}_n)-\frac{1}{2}\sum_k\omega_k Q_{nk}^2 \\ V_1(s_n,\boldsymbol{Q}_n) &= -\sum_k f_k\left(s_n\right)Q_{nk}+\frac{1}{2}\sum_{k,k'}\Omega_{k,k'}\left(s_n\right)Q_{nk}Q_{nk'}. \end{aligned} \tag{5.27}$$

With the help of the exact propagator for harmonic oscillators [119] one can obtain the following result

$$\begin{aligned} \langle\boldsymbol{Q}_{n+1}|e^{-iH_1(s_n)\delta_n}|\boldsymbol{Q}_n\rangle &= \exp\left\{-iV_1(s_n,\boldsymbol{Q}_n)\delta_n\right\}\prod_k\sqrt{\frac{\omega_k}{2\pi i\sin(\omega_k\delta_n)}} \\ &\quad\times\exp\left\{\sum_k i\omega_k\left[\left(\cot(\omega_k\delta_n)+\frac{(\omega_k\delta_n)}{2}\right)Q_{nk}^2-\frac{Q_{n+1,k}Q_{nk}}{\sin(\omega_k\delta_n)}\right]\right\}. \end{aligned} \tag{5.28}$$

One should properly choose ω_k to minimize the difference between $V_1(s_n,\boldsymbol{Q}_n)$ and harmonic potential $V_{har}(\boldsymbol{Q}_n)$, i.e., $\Delta V_1(s_n,\boldsymbol{Q}_n)$. However, it is not very strict to choose ω_k since we already assumed δ_n to be small enough. In the following we set $\omega_k=\Omega_{kk}(0)$ to be the same for different grid s_n on the reaction path. Based on Eq. (5.28) we can simplify the influence function by a Gaussian type integration

$$\begin{aligned} F_{infl}\left(\boldsymbol{s},\boldsymbol{\delta}\right) &= F_Q\int_{-\infty}^{\infty}\cdots\int_{-\infty}^{\infty}d\boldsymbol{Q}_1 d\boldsymbol{Q}_2\cdots d\boldsymbol{Q}_N \\ &\quad\exp\{g(\boldsymbol{s},\{\boldsymbol{Q}\})\} \\ g(\boldsymbol{s},\{\boldsymbol{Q}\}) &= \sum_{nk} i\omega_k\left[\left(\cot(\omega_k\delta_n)+\frac{(\omega_k\delta_n)}{2}\right)Q_{nk}^2-\frac{Q_{n+1,k}Q_{nk}}{\sin(\omega_k\delta_n)}\right] \\ &\quad+i\sum_{nk}\delta_n f_k(s_n)Q_{nk}-\frac{i}{2}\sum_{nkk'}Q_{nk}\Omega_{kk'}(s_n)Q_{nk'}, \end{aligned} \tag{5.29}$$

where $F_Q = \prod_{nk} \sqrt{\frac{\omega_k}{2\pi i \sin(\omega_k \delta_n)}}$ is path independent.

To get reasonable rate constant we consider a molecule coupled with the environment. To describe the environment effect we should include additional terms in the full Hamiltonian

$$H_2 = \sum_\alpha \left\{ -\frac{\hbar^2}{2}\frac{\partial^2}{\partial q_\alpha^2} + \frac{1}{2}\omega_\alpha^2 q_\alpha^2 \right\} + \sum_\alpha d_\alpha(s) q_\alpha + \sum_{\alpha,k} C_{\alpha,k}(s) Q_k q_\alpha, \tag{5.30}$$

where q_α is the bath oscillator coordinate and ω_α the corresponding frequency which can be continuous. Starting from the full Hamiltonian $H = H_0 + H_1 + H_2$ we follow the same procedure mentioned above except that H_1 should be replaced by $H_1 + H_2$. We can get the new influence functional

$$\begin{aligned}
F_{infl}(\boldsymbol{s}, \boldsymbol{\delta}) &= \int_{-\infty}^{\infty} d\boldsymbol{q} d\boldsymbol{Q} \langle \boldsymbol{q}| \langle \boldsymbol{Q}| \prod_{n=N}^{1} e^{-i\left[H_1\left(s_n, \boldsymbol{Q}\right) + H_2\left(s_n, \boldsymbol{Q}, \boldsymbol{q}\right)\right]\delta_n} |\boldsymbol{Q}\rangle |\boldsymbol{q}\rangle \\
&= F_q F_Q \int_{-\infty}^{\infty} \cdots \int_{-\infty}^{\infty} d\boldsymbol{Q}_1 d\boldsymbol{Q}_2 \cdots d\boldsymbol{Q}_N d\boldsymbol{q}_1 d\boldsymbol{q}_2 \cdots d\boldsymbol{q}_M \\
&\quad \exp\{g(\boldsymbol{s}, \{\boldsymbol{Q}\}, \{\boldsymbol{q}\})\} \\
g(\boldsymbol{s}, \{\boldsymbol{Q}\}, \{\boldsymbol{q}\}) &= \sum_{nk} i\omega_k \left[\left(\cot(\omega_k \delta_n) + \frac{(\omega_k \delta_n)}{2} \right) Q_{nk}^2 - \frac{Q_{n+1,k} Q_{nk}}{\sin(\omega_k \delta_n)} \right] \\
&\quad + i \sum_{nk} \delta_n f_k(s_n) Q_{nk} - \frac{i}{2} \sum_{nkk'} Q_{nk} \Omega_{kk'}(s_n) Q_{nk'} \\
&\quad + \sum_{n\alpha} \frac{i\omega_\alpha}{\sin(\omega_\alpha \delta_n)} \left[\cos(\omega_\alpha \delta_n) q_{n\alpha}^2 - q_{n+1,\alpha} q_{n\alpha} \right] \\
&\quad - i \sum_{n\alpha} \delta_n d_\alpha(s_n) q_{n\alpha} - i \sum_{nk\alpha} \delta_n C_{\alpha k}(s_n) Q_{nk} q_{n\alpha},
\end{aligned} \tag{5.31}$$

where $F_q = \prod_{n\alpha} \sqrt{\frac{\omega_\alpha}{2\pi i \sin(\omega_\alpha \delta_n)}}$.

Having the above result at hand what we need to do is just to calculate the complex-coefficient Gaussian type integrals

$$\int_{-\infty}^{\infty} \cdots \int_{-\infty}^{\infty} dx_1 dx_2 \cdots dx_N \exp\{-\sum_{mn} A_{mn} x_m x_n + i \sum_{mn} B_{mn} x_m x_n + \sum_n W_n x_n\}, \tag{5.32}$$

where both $\mathbf{A}$ and $\mathbf{B}$ are real symmetric matrices. For any physical case the integration converges, i.e., the matrix $\mathbf{A}$ is positive-definite. It is then easy to find one invertible real matrix $\mathbf{U}_c$ to congruently diagonalize both $\mathbf{A}$ and $\mathbf{B}$ simultaneously since $\mathbf{A}$ is positive-definite. The detailed procedure is shown in the following equations

$$\begin{aligned}
\mathbf{U_1}^T \mathbf{A} \mathbf{U_1} &= \mathbf{a} \equiv \mathrm{diag}\{a_1, a_2, \cdots, a_N\} \\
\mathbf{U_2}^T \mathbf{a}^{-\frac{1}{2}} \mathbf{U_1}^T \mathbf{B} \mathbf{U_1} \mathbf{a}^{-\frac{1}{2}} \mathbf{U_2} &= \mathbf{b} \equiv \mathrm{diag}\{b_1, b_2, \cdots, b_N\},
\end{aligned} \tag{5.33}$$

where both $\mathbf{U_1}$ and $\mathbf{U_2}$ are orthogonal matrices which diagonalize the corresponding real symmetric matrices, respectively. Since the matrix $\mathbf{A}$ is positive-definite all eigenvalues $\{a_n\}$ are positive. The final transformation matrix is defined as $\mathbf{U}_c = \mathbf{U_1 a}^{-\frac{1}{2}}\mathbf{U_2}$ which transforms $\mathbf{U}_c^T\mathbf{A}\mathbf{U}_c = \mathbf{1}$ and $\mathbf{U}_c^T\mathbf{B}\mathbf{U}_c = \mathbf{b}$. Using the new variables $\{y_n\}$ defined by $y_n = \sum_m (U_c^{-1})_{nm} x_m$ the integration in Eq. (5.32) can be solved analytically

$$\begin{aligned}
&\int_{-\infty}^{\infty}\cdots\int_{-\infty}^{\infty} dx_1 dx_2\cdots dx_N \exp\{-\sum_{mn} A_{mn}x_m x_n + i\sum_{mn} B_{mn}x_m x_n + \sum_n W_n x_n\} \\
= \;& |\mathrm{Det}(\mathbf{U}_c^{-1})| \int_{-\infty}^{\infty}\cdots\int_{-\infty}^{\infty} dy_1 dy_2\cdots dy_N \exp\{-\sum_n (1-ib_n)y_n^2 + \sum_n w_n y_n\} \\
= \;& \prod_n \left(\sqrt{\frac{\pi}{a_n}}\sqrt{\frac{1}{1-ib_n}}\exp\{\frac{w_n^2}{4(1-ib_n)}\}\right),
\end{aligned} \tag{5.34}$$

where $w_n = \sum_m (U_c)_{nm} W_m$. Here and in the following the square root of a complex number means its principal value, i.e., the one with non-negative real part.

In principle it is now possible to solve Eq. (5.31). However, it is numerically impossible to diagonalize a large matrix for *each* specified path. We can first solve the environment part since the quadratic coefficients of the bath oscillators are path independent and assumed to be uncorrelated between each other. Based on above mentioned procedure we can find a frequency dependent real invertible matrix $\mathbf{U}_q(\omega)$ to congruently diagonalize each bath mode

$$\begin{aligned}
&\tilde{q}_n = \sum_{n'} [\mathbf{U}_q^{-1}(\omega)]_{nn'} q_{n'} \\
&\sum_n \frac{i\omega}{\sin(\omega\delta_n)}\left[\cos(\omega\delta_n)q_n^2 - q_{n+1}q_n\right] = -\sum_n (1-ib_n^q(\omega))\tilde{q}_n^2,
\end{aligned} \tag{5.35}$$

where $\{a_n^q(\omega)\}$ (which will appear in the following) and $\{b_n^q(\omega)\}$ are the eigenvalues while diagonalizing the corresponding coefficients matrix according the procedure introduced in Eq. (5.33). Using the new variables $\tilde{q}_{n\alpha} = \sum_{n'} [\mathbf{U}_q^{-1}(\omega_\alpha)]_{nn'} q_{n'\alpha}$ the integration over $\{\tilde{q}_{n\alpha}\}$ can be calculated analytically. The final result for influence functional is simplified as

$$\begin{aligned}
F_{infl}(\boldsymbol{s},\boldsymbol{\delta}) &= F_q F_Q \tilde{F}_q \int_{-\infty}^{\infty}\cdots\int_{-\infty}^{\infty} d\boldsymbol{Q}_1 d\boldsymbol{Q}_2\cdots d\boldsymbol{Q}_N \exp\{g(\boldsymbol{s},\{\boldsymbol{Q}\})\} \\
g(\boldsymbol{s},\{\boldsymbol{Q}\}) &= \sum_{nk} i\omega_k \left[\left(\cot(\omega_k\delta_n) + \frac{(\omega_k\delta_n)}{2}\right)Q_{nk}^2 - \frac{Q_{n+1,k}Q_{nk}}{\sin(\omega_k\delta_n)}\right] \\
&\quad + i\sum_{nk}\delta_n f_k(s_n)Q_{nk} - \frac{i}{2}\sum_{nkk'} Q_{nk}\Omega_{kk'}(s_n)Q_{nk'} + \Delta(\boldsymbol{s}) \\
&\quad + i\sum_{nk}\delta_n \Delta f_k(s_n)Q_{nk} + \sum_{nkn'k'} g_{nk,n'k'}Q_{nk}Q_{n'k'},
\end{aligned} \tag{5.36}$$

where $\tilde{F}_q = \prod_{n\alpha} \sqrt{\frac{\pi}{a_n^q(\omega_\alpha)}} \sqrt{\frac{1}{1-ib_n^q(\omega_\alpha)}}$ and the additional terms caused by the environment are defined as follows:

$$\begin{aligned}
\Delta(\boldsymbol{s}) &= \sum_{n\alpha} \frac{w_{n\alpha}^2}{4[1-ib_n^q(\omega_\alpha)]} \\
w_{n\alpha} &= -i \sum_{n'} [U_q(\omega_\alpha)]_{n'n} \delta_{n'} d_\alpha(s_{n'}) \\
\Delta f_k(s_n) &= \sum_{n'\alpha} \frac{w_{n'\alpha} u_{n'\alpha,nk}}{2[1-ib_{n'}^q(\omega_\alpha)]} \\
u_{n'\alpha,nk}(s_n) &= -i[U_q(\omega_\alpha)]_{nn'} \delta_n C_{\alpha k}(s_n) \\
g_{nk,n'k'}(s_n, s_{n'}) &= \sum_{n''\alpha} \frac{u_{n''\alpha,nk} u_{n''\alpha,n'k'}}{4[1-ib_{n''}^q(\omega_\alpha)]}.
\end{aligned} \tag{5.37}$$

By now we have obtained the final expression for the influence functional shown in Eq. (5.36). Directly applying the procedure of Eq. (5.33) we can obtain the result for the integration in Eq. (5.36)

$$F_{infl}(\boldsymbol{s}, \boldsymbol{\delta}) = F_q F_Q \tilde{F}_q e^{\Delta(\boldsymbol{s})} \prod_{nk} \left(\sqrt{\frac{\pi}{a_{nk}}} \sqrt{\frac{1}{1-ib_{nk}}} \exp\{\frac{w_{nk}^2}{4(1-ib_{nk})}\} \right), \tag{5.38}$$

where $\{a_{nk}\}$, $\{b_{nk}\}$ and $\{w_{nk}\}$ should be determined by the diagonalization of the complex coefficient matrix as detailed in Eq. (5.33).

5.2.4 Application to Large Systems

In general we can assume the coupling strength between Q_k and q_α does not strongly depend on s. Thus we ignore the s-dependence of the coupling strength between Q_k and q_α, i.e, $\{C_{\alpha k}\}$ are simply constants and hence $\{g_{nk,n'k'}(s_n, s_{n'}) = g_{nk,n'k'}\}$ are also constants. Concerning large molecules, it may be still not feasible to diagonalize a large matrix for each specified path. However, not all the modes $\{Q_k\}$ strongly depend on the reaction path s, which makes it a reasonable approximation to replace the weak s-dependent modes by certain mean values. In the following we use $\{Q_k\}$ to denote the relatively more important DOFs, i.e., they significantly depend on s. And the rest DOFs are denoted by $\{Q_\nu\}$. In Eq. (5.36), the following quadratic coefficients will be replaced by their s-independent mean values along the reaction path

$$\Omega_{\nu\nu'}(s_n) \rightarrow < \Omega_{\nu\nu'} > \equiv \frac{1}{2L} \int_{-L}^{L} \Omega_{\nu\nu'}(s) ds, \tag{5.39}$$

where $2L$ is the length of the reaction path. Under this approximation, we need to diagonalize a large matrix just once while for each specified path we only need to diagonalize a much smaller matrix since only a few number of DOFs significantly depend on s.

Following the idea of Eq. (5.33) we can find a real invertible matrix $\mathbf{U^Q}$ which congruently diagonalizes the quadratic coefficient matrix related only to $\{Q_\nu\}$

$$\begin{aligned}
&\sum_{n\nu} i\omega_\nu \left[\left(\cot(\omega_\nu\delta_n) + \frac{(\omega_\nu\delta_n)}{2}\right) Q_{n\nu}^2 - \frac{Q_{n+1,\nu}Q_{n\nu}}{\sin(\omega_\nu\delta_n)}\right] \\
&-\frac{i}{2}\sum_{n\nu\nu'} \delta_n < \Omega_{\nu\nu'} > Q_{n\nu}Q_{n\nu'} + \sum_{n\nu,n'\nu'} g_{n\nu,n'\nu'}Q_{n\nu}Q_{n'\nu'} \\
= \; &-\sum_{n\nu}(1-ib_{n\nu})\tilde{Q}_{n\nu}^2,
\end{aligned} \tag{5.40}$$

where $\tilde{Q}_{n\nu} = \sum_{n'\nu'} \left(\mathbf{U^Q}\right)^{-1}_{n\nu,n'\nu'} Q_{n\nu'}$. With the help of this transformation we can analytically integrate over the $\{\tilde{Q}_{n\nu}\}$ part. This will further contribute a pre-factor $\tilde{F_Q}$ and some modifications to the exponential factor compared with Eq. (5.36)

$$\begin{aligned}
F_{infl}\left(\boldsymbol{s},\boldsymbol{\delta}\right) &= F_qF_Q\tilde{F}_q\tilde{F}_Q \int_{-\infty}^{\infty}\cdots\int_{-\infty}^{\infty} d\boldsymbol{Q}_1 d\boldsymbol{Q}_2\cdots d\boldsymbol{Q}_N \exp\{g(\boldsymbol{s},\{Q_{nk}\})\} \\
g(\boldsymbol{s},\{Q_{nk}\}) &= \sum_{nk} i\omega_k \left[\left(\cot(\omega_k\delta_n) + \frac{(\omega_k\delta_n)}{2}\right) Q_{nk}^2 - \frac{Q_{n+1,k}Q_{nk}}{\sin(\omega_k\delta_n)}\right] \\
&\quad + i\sum_{nk}\delta_n f_k(s_n)Q_{nk} - \frac{i}{2}\sum_{nkk'} Q_{nk}\Omega_{kk'}(s_n)Q_{nk'} + \Delta(\boldsymbol{s}) \\
&\quad + i\sum_{nk}\delta_n \Delta f_k(s_n)Q_{nk} + \sum_{nkn'k'} g_{nk,n'k'}Q_{nk}Q_{n'k'} + \tilde{\Delta}(\boldsymbol{s}) \\
&\quad + i\sum_{nk}\delta_n \tilde{\Delta f}_k(s_n)Q_{nk} + \sum_{nkn'k'} \tilde{g}_{nk,n'k'}Q_{nk}Q_{n'k'},
\end{aligned} \tag{5.41}$$

where $\tilde{F_Q} = \prod_{n\nu}\sqrt{\frac{\pi}{a_{n\nu}}}\sqrt{\frac{1}{1-ib_{n\nu}}}$ and the additional terms caused by the reduction of DOFs are defined as follows:

$$\begin{aligned}
\tilde{\Delta}(\boldsymbol{s}) &= \sum_{n\nu}\frac{w_{n\nu}^2}{4(1-ib_{n\nu})} \\
w_{n\nu} &= \sum_{n'\nu'}(\mathbf{U^Q})_{n'\nu',n\nu}\left[i\delta_{n'}f_{\nu'}(s_{n'}) + i\delta_{n'}\Delta f_{\nu'}(s_{n'})\right] \\
\tilde{\Delta f}_k(s_n) &= \sum_{n'\nu'}\frac{w_{n'\nu'}u_{nk,n'\nu'}}{2(1-ib_{n'\nu'})} \\
u_{nk,n'\nu'} &= 2\sum_{n''\nu}(\mathbf{U^Q})_{n''\nu,n'\nu'}g_{nk,n''\nu} - i\sum_{\nu}(\mathbf{U^Q})_{n\nu,n'\nu'}\delta_n\Omega_{k\nu}(s_n) \\
\tilde{g}_{nk,n'k'}(s_n,s_{n'}) &= \sum_{n''\nu}\frac{u_{nk,n''\nu}u_{n'k',n''\nu}}{4(1-ib_{n''\nu})}
\end{aligned} \tag{5.42}$$

The final numerical calculations can start from Eq. (5.41) which is feasible since only a very low dimensional matrix needs to be diagonalized for each specified path.

5.3 Results of a Preliminary Study

For a specific application, we have performed a preliminary simulation based on a model Hamiltonian of the 6-Aminofulvene-1-aldimine. For simplicity we did not start from Eq. (5.41). In stead, we start from Eq. (5.36) by selecting one intra-molecular mode Q_k which most strongly couples to the reaction path. The intra-molecular mode which we select is the one involving large amplitude stretching of nitrogen atoms. We have to mention that the present simulation is a very preliminary one since the other 104 intra-molecular modes together with the environment are simply treated as bath DOFs. The purpose is to show that this new method does work for the numerical calculation of reaction rate constants.

The unit vector which defines the linear reaction path is just the direction pointing from the reactant to the product, i.e., $\boldsymbol{e}_s = \frac{(\boldsymbol{R}_{prod}-\boldsymbol{R}_{reac})}{|\boldsymbol{R}_{prod}-\boldsymbol{R}_{reac}|}$. The reactant and the product are two equivalent minimum configurations as shown in Fig. 5.2. The required quantities for generating the reaction path Hamiltonian, namely $V(\boldsymbol{R}_0)$, $f_k(s)$, and $\Omega_{k,k'}(s)$ appearing in Eq. (5.19), are calculated according to Section 5.2.2 based on the Hessian matrix by the B3LYP/6-31+G(d,p) level of theory. The coupling between the environment and the molecular DOFs are defined as

$$\begin{aligned} d_\alpha(s) &= d_1 e^{-\omega_\alpha^2/d_2^2}(s+\eta s^2) \\ C_{\alpha,k}(s) &= C_{\alpha,k} = c_1 e^{-(\omega_k-\omega_\alpha)^2/c_2^2}, \end{aligned} \tag{5.43}$$

where d_1, d_2, ω_0, η, c_1, and c_2 are parameters. The s dependence has been expanded to the second order and the bath frequency dependence has been simply chosen to have the Gaussian form. The environment modes are assumed to have uniform density of states in the region of which we take into account the coupling with the molecular DOFs.

According to the present linear reaction path, the barrier is as high as 14.85 kcal/mol. The details of the potential curve along the reaction coordinate are shown in Fig. 5.3. As expected, the shapes of potential cures for hydrogen and deuterium transfers are the same. The only difference lies in the length of the step Δs which appears in Eq. (5.21). The ratio for the steps is only slightly different from one, $\Delta s(H)/\Delta s(D) = 0.9978$, due to the fact that the linear reaction path involves many modes' contributions which decrease the effective isotope mass ratio. The effective barrier will decrease to the appropriate value as compared to the barrier in Fig. 5.3 after taking into account of all the intra- and inter-molecular couplings.

The calculated KIEs are reasonable as shown in Fig. 5.4. At 298 K the calculated value is $k_{12}^H/k_{12}^D = 10$. The parameters we adopted are $c_1 = d_1 = 10^{-6}$, $c_2 = d_2 = 0.01$ Hartree $= 6.28$ kcal/mol, and $\eta = 0.2\Delta s^{-1}$. The involved bath frequency region starts

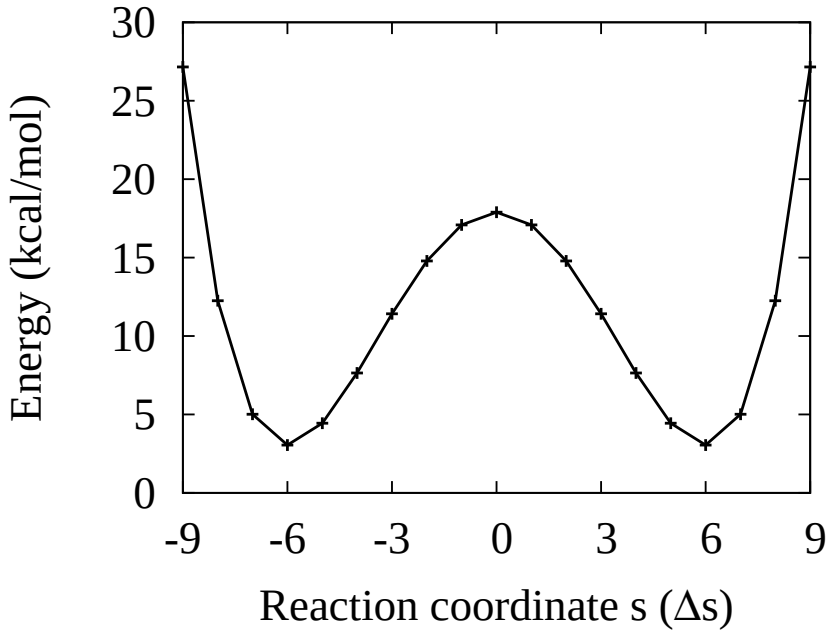

Figure 5.3: The zeroth order potential energy curve obtained by B3LYP/6-31+G(d,p) for the hydrogen/deuterium atom transfer reaction in 6-Aminofulvene-1-aldimine as shown in Fig. 5.1. The reference geometry is $s = 0$ and the reactant/product is $s = \pm 6$.

from 3 to 30 kcal/mol with 50 harmonic oscillators equally distributed. The major drawback of the present study is that the activation energies are too high (3-4 times of the experimental values) and the difference between the activation energies of different isotopomers are too small, the latter can be explained by the ratio $\Delta s(H)/\Delta s(D) = 0.9978$ which implies that the ratio of H/D transfer rates can be correctly described only after taking into account many intra-molecular modes. In general the effective reaction barrier will decrease if the number of coupled modes or the coupling strength increases. Therefore one can expect that the calculated results will be more reasonable if one includes all the 105 intra-molecular modes according to Section 5.2.4 and more bath modes.

We have to mention that in principle the curves in Fig. 5.4 can give the correct thermal activation energy in the high temperature region but wrong behavior in the low temperature region due to an approximation we have adopted to decrease the numerical efforts. As can be seen in Eq. (5.22), we have to do a multi-fold integration over the path variable s to calculate the rate constant. One can imagine that the thermal activation behavior can be correctly described by taking into account only a few configurations around the transition state, while the low temperature tunneling process can be correctly described once we include the configurations which locate near the tunneling energy. In Fig. 5.4 we have only considered three configurations near the reference geometry, namely, the integration over s has been substituted by a sum over $s = -1, 0, 1$. For the partition function the in-

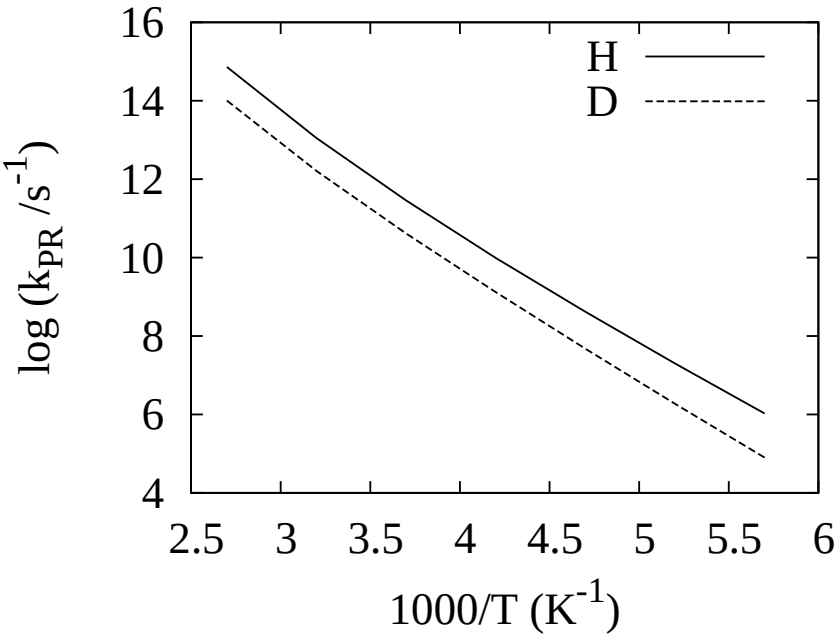

Figure 5.4: The calculated temperature dependence of H/D transfer rate constants in the thermal activation region based on a 1D linear reaction path coupled to one intramolecular modes and 50 bath modes.

tegration is replaced by a sum over $s = -7, -6, -5$. In this specific case, the calculation effort will be greatly decreased from 19^{2N} path integrals to 3^{2N} ones.

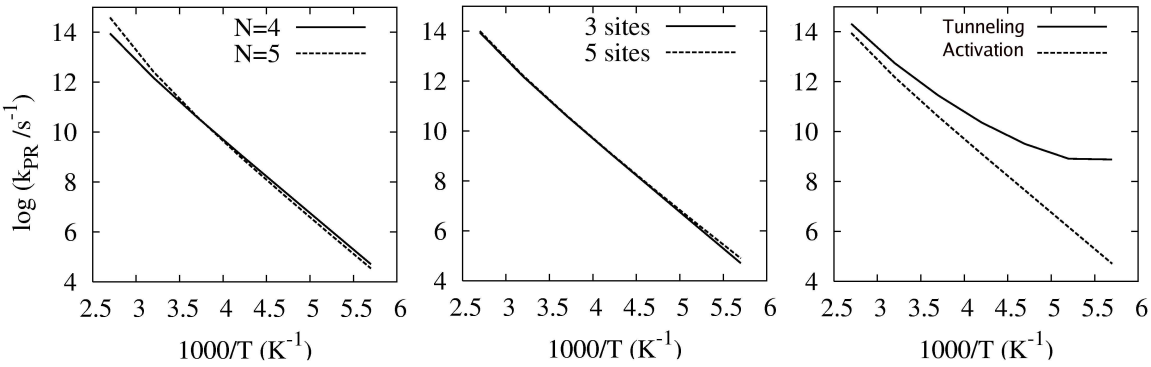

Figure 5.5: The left and middle panels show the convergence of the thermal activation energy (the slope) in the high temperature region by only considering configurations which are important for thermal activation, i.e., around $s = 0$. The right panel schematically shows the quantum tunneling effects (see e.g., Fig. 1.1) in the low temperature region by covering some configurations which are important for tunneling (specifically $s = \pm 5$ for the solid curve). See the text for more details.

To clearly show how this technique works, we have studied the parameter dependence of the results in Fig. 5.5. Let us first check the convergence of the results. The left panel

of Fig. 5.5 shows two different rate curves for different numbers of time slices, $N = 4$ and $N = 5$, respectively. From this figure we can say that the result is converged for N not less than 4. In all the other figures the time slices are set to be $N = 4$. The middle panel shows the path dependence of the results. One (3 sites) is obtained by only taking into account $s = -1, 0, 1$ while the other (5 sites) by taking into account $s = -2, -1, 0, 1, 2$. The ignorable difference shows the applicability of the simplification technique which we have adopted for the high temperature calculations. Finally the right panel shows how the H/D transfer mechanism changes from the high temperature thermal activation predominated process to the low temperature quantum tunneling predominated process. The dashed curve is obtained by covering $s = -2, -1, 0, 1, 2$ while the solid curve is obtained by covering $s = -5, -1, 0, 1, 5$. The change of mechanics is already reflected in the solid curve in the right panel of Fig. 5.5 by only covering two configurations for tunneling. The results will be better if we cover more related configurations or even all the 19 configurations from $s = -9$ to $s = 9$. Apart from the knowledge of the critical temperature, we can further find out which configurations contributes to the tunneling process most significantly if we cover more and more configurations along the reaction path step by step until convergence.

5.4 Summary of this Chapter

In this chapter we have studied condensed phase proton transfer rates. The reaction rate constants predicted by the classical transition state theory is not reliable especially for low barrier reactions. We have developed a new method to generate a reaction surface Hamiltonian and to calculate the reaction rate constant based on the work of Miller and Makri [59, 60, 117, 118]. A preliminary application is performed based on a 1D linear reaction path Hamiltonian and the calculated results show reasonable trends for the change of predominated proton transfer mechanics from high temperature thermal activation to low temperature tunneling. We have also discussed the parameter dependence of the results and introduced a practical technique to greatly reduce the numerical effort. The results become more reasonable when increasing calculation efforts, which consequently imply the applicability and predictability of the present theory.

Chapter 6

Summary and Outlook

Few problems in recent years have attracted as much attention as the hydrogen bonding and transfer in solution, biomolecular systems, and material sciences. However, a molecular level of description of HBs remains elusive since the proton behaves in a quantum mechanical way on the scale of typical HB lengths and couples to many degrees of freedom. Among the widely investigated phenomena of HBs the finite charged clusters are believed to play an essential role in many fundamental processes. The present theoretical work mainly focus on the charged clusters associated by HBs in the gas phase to grasp some essential features of HBs involving the geometry, IR spectrum and isotope effects.

The most important limiting structures in the aqueous solution are the Eigen cation $H_3O^+ \cdot (H_2O)_3$ and the Zundel cation $[H_2O \cdots H \cdots OH_2]^+$ which are responsible for the proton diffusion processes. And the anion counterpart is the $[HO \cdots H \cdots OH]^-$ structure which play the same role for hydroxide diffusion as the Zundel cation for proton diffusion. The understanding for Zundel cation is rather deep and extensive based on previous investigations in particular the breakthrough of recent full dimensional quantum study by MCTDH. However the investigations on the anion counterpart $[HO \cdots H \cdots OH]^-$ is less impressive therefore further investigations are required. For this kind of strong hydrogen bonded systems we need multidimensional quantum dynamics to appropriately describe them. A concise theory for generating the vibrational Hamiltonian and method on solving multidimensional Schrödinger equation has been introduced in Chapter 2 for this purpose.

As isoelectronic analogies of the protonated water clusters, the protonated ammonia clusters are also very important in our daily life such as nitrogen metabolism. For the protonated ammonia dimer $N_2H_7^+$, a quantum simulation based on a reduced 6D model has been performed. The six coordinates mainly focus on the HB including the shared proton stretching and bending, the $NH_3 \cdots NH_3$ stretching and the umbrella like motions of the terminal ammonia molecules. We first scan the required PESs at MP2/aug-cc-

pVTZ level of theory and generate a 6D PES by correlation expansion containing all (6) 1D PESs, all (15) 2D PESs and some most important (7) 3D PESs. The 6D kinetic energy operator for the case of total angular momentum equal to zero is derived analytically exploiting the theory developed in Chapter 2. After generating the Hamiltonian operator the Schrödinger equation is solved by MCTDH.

The ground state of $N_2H_7^+$ has D_{3d} symmetry with the proton locating in the center which agrees well with previous investigations. This kind of symmetrization by zero point vibration is typical for strong HBs. The calculated IR spectrum shows that the first and also the most intense band is the central proton stretching fundamental transition at 409 cm^{-1}. Then comes the fundamental transition of asymmetric umbrella type motion of the terminal ammonias at 1336 cm^{-1}. In between we have the combination bands of the proton stretching and $NH_3 \cdots NH_3$ stretching modes which also significantly contribute to the rich IR bands. The last one is the fundamental transition of the two fold degenerate bending mode at 1542 cm^{-1}. The calculated IR spectrum agrees well with the recent experiment by Asmis group [96, 97].

For large $NH_4^+(NH_3)_n$ (n=2-4) clusters we first investigate the potential energy curve along the proton transfer coordinate. All of them are found to be much less anharmonic due to weakening of HB. Therefore we study the large clusters with harmonic analysis at the MP2/6-311+G(d,p) level of theory. Each large cluster has the solvated ammonium structure with a stable central NH_4^+ fragment different from $N_2H_7^+$. The calculated IR spectra agree qualitatively with the experiment by Asmis group [97]. The most intense IR absorption band between 1100 and 1200 cm^{-1} for each cluster is caused by the collective ν_2 bending mode (which corresponds to the asymmetric umbrella motion in the $N_2H_7^+$ case) of side NH_3. There is a systematic red shift of this band when the cluster size increases. The reason is the weakening of HB leads to a larger $N \cdots N$ distance consequently soften the potential curve for this mode.

Still there is something more to be done in the future as has been mentioned in Chapter 3. The 6D model for $N_2H_7^+$ should be enlarged to a 9D model to include three wags of the two terminal NH_3 fragments. Meanwhile a sufficiently accurate PES is also a severe challenge to quantum chemistry. A full dimensional investigation will be definitely impressive yet it seems to be hardly feasible concerning present computer abilities. For large clusters there are also lots of phenomena which go out of the range of harmonic predictability. An appropriate reduced model involving the relative motions of the central NH_4^+ and the terminal NH_3 fragments might be capable of interpreting the anharmonic effects which already appear in the low frequency region IR spectra of a recent experiment by the Asmis group.

Concerning the fundamental water clusters we have investigated the deprotonated water dimer $[HO\cdots H\cdots OH]^-$ in full dimensionality. The kinetic energy operator for the case of total angular momentum equal to zero is derived analytically exploiting the theory developed in Chapter 2 for each isotopomer (cf. Appendix C). Concerning the 9D PES construction, we use the PES subroutine by Bowman group which is based on fitting of a sufficient number of CCSD(T)/aug-cc-pVTZ data points. The nine coordinates have been divided into three groups and the 9D PES is expanded with all the two-group correlations. This means the expansion actually incorporate six-mode correlations among nine individual coordinates. Then each ground state is obtained by wave function relaxation and the torsional splitting state is also calculated by improved relaxation with MCTDH.

The first conclusion is that the general trend of the primary energetic isotope effects in this series of isotopomers. Each side O–H group deuteration lowers the ZPE by about 600 cm^{-1} and each central position deuteration lowers the ZPE by about 520 cm^{-1}, both irrespective of whether the rest positions are deuterated or not. The difference between the side and central position deuteration is that the central position deuteration includes the H-bond to D-bond substitution at the same time. Their difference is nothing but the difference between the bond energy of H-bond and D-bond, namely the H-bond is more stable than D-bond by about 80 cm^{-1} (cf. Section 4.3.2) for this series of isotopomers. The reason is that the proton distribution is more delocalized consequently the couplings between the central proton motion and the rest coordinates, which make the system more stable, are larger than the deuteron case. Since the reason is general we can draw the conclusion that H-bond is in general more stable than D-bond for strong HBs yet the bond energy difference may differ for different cases.

The secondary geometry isotope effects as well as the tunneling splitting effects associated with the torsion are also investigated. For each isotopomer the quantum mean value of $O\cdots O$ distance increases compared with the classical transition state due to the zero point vibration. Upon deuteration of the central proton the $O\cdots O$ distance slightly decreases due to the more localized distribution of deuteron. One should realize that in general a shorter HB length corresponds to a stronger bonding. However, it is not true for slight differences such as this series of isotopomers. The reduction of $O\cdots O$ distance due to central deuteration is about 0.005 Å for symmetric cases and 0.009 Å for asymmetric cases. The tunneling splitting is related to the torsion frequency determined by the side O–H group deuteration status. Each side position deuteration increases the reduced moment of inertia therefore the energy splitting is decreased by 6-7 cm^{-1}.

We have to mention that the investigations of $[HO\cdots H\cdots OH]^-$ anion are far from a final conclusion despite the existing extensive investigations. Concerning MCTDH which

requires sum of products form of PES we have to fit the PES. Limited by the computer ability and algorithms a fitting of 9D PES with high accuracy is extremely difficult. It would be quite interesting to use the original 9D PES instead of correlation expansion to see further refinements.

In addition the present work also covers condensed phase proton transfer process. A general theory for reaction surface Hamiltonian and reaction rate constant calculations has been developed. A preliminary simulation for a model Hamiltonian based on 6-Aminofulvene-1-aldimine has been performed. The calculated reaction rate constant versus temperature shows Arrhenius rate behavior at high temperature region and the activation energy for deuterium atom is larger than hydrogen atom due to its heavier mass. The calculated results show reasonable trends for the change of predominated proton transfer mechanics from high temperature thermal activation to low temperature tunneling. The results become more reasonable when increasing calculation efforts, which consequently imply the applicability and predictability of the present theory. Our further investigation will be picking out suitable parameters, covering more grid points along the reaction path, and including more intra- and inter- molecular modes for specified problems.

To elucidate the complexity of hydrogen bonding and transfer in real solution or bio-environment is the ultimate goal. Successful theoretical description of condensed phase phenomena is a long time pursuing for numerous theoreticians. However, there is no generally accepted method which in most cases gives convincing results. We still strongly rely on the gas phase features and make some reasonable arguments about environmental influence on the deviation of condensed phase from gas phase. Up to now most of the interesting gas phase systems have been investigated at certain level and the future work will mainly focus on condensed phase.

Appendix A

Hermitian Conjugates of Momentum Operators

To derive the expressions for the HCMOs in LRF is the most tedious part as mentioned in Chapter 2. The things become much more complicated when we exploit coordinates defined in MRF. Consider the LRF defined by three orthogonal unit vectors $\{\boldsymbol{e}_x, \boldsymbol{e}_y, \boldsymbol{e}_z\}$ and a MRF defined by three orthogonal unit vectors $\{\boldsymbol{e}_{x'}, \boldsymbol{e}_{y'}, \boldsymbol{e}_{z'}\}$. The orientation angles of $\boldsymbol{e}_{z'}$ in the LRF are (ϑ, ϕ). To obtain the connection between the LRF and the MRF we first apply two excessive rotations $\mathbf{U}_y(\vartheta)$ and $\mathbf{U}_z(\phi)$ to the LRF, where $\mathbf{U}_y(\vartheta)$ means rotating ϑ around $\boldsymbol{e}_y$ and $\mathbf{U}_z(\phi)$ means rotating ϕ around $\boldsymbol{e}_z$. The matrix representation of them are

$$\begin{aligned} \mathbf{U}_y(\vartheta) &= \begin{pmatrix} \cos\vartheta & 0 & \sin\vartheta \\ 0 & 1 & 0 \\ -\sin\vartheta & 0 & \cos\vartheta \end{pmatrix} \\ \mathbf{U}_z(\phi) &= \begin{pmatrix} \cos\phi & -\sin\phi & 0 \\ \sin\phi & \cos\phi & 0 \\ 0 & 0 & 1 \end{pmatrix}. \end{aligned} \tag{A.1}$$

The new reference frame generated by applying $\mathbf{U}_y(\vartheta)$ and $\mathbf{U}_z(\phi)$ to the LRF has the same z axis as the MRF, i.e., the only difference between the two reference frames is just a rotation of angle χ around $\boldsymbol{e}_{z'}$. Therefore the MRF can be obtained by applying three excessive rotations $\mathbf{U}_y(\vartheta)$, $\mathbf{U}_z(\phi)$ and $\mathbf{U}_{z'}(\chi)$ to the LRF, namely

$$\boldsymbol{e}_{\alpha'} = \mathbf{U}_{z'}(\chi)\mathbf{U}_z(\phi)\mathbf{U}_y(\vartheta)\boldsymbol{e}_\alpha, \quad \alpha = x, y, z, \tag{A.2}$$

where $\mathbf{U}_{z'}(\chi)$ means rotating χ around $\boldsymbol{e}_{z'}$. The matrix representation for $\mathbf{U}_{z'}(\chi)$ in the MRF is the same with $\mathbf{U}_z(\chi)$ in the LRF. Since the third rotation $\mathbf{U}_{z'}(\chi)$ in Eq. (A.2) has no effects on $\boldsymbol{e}_{z'}$ we actually have $\boldsymbol{e}_{z'} = \mathbf{U}_z(\phi)\mathbf{U}_y(\vartheta)\boldsymbol{e}_z$. Exploiting the rules between vector and operator transformations we can obtain the expression for $\mathbf{U}_{z'}(\chi)$ in the LRF

$$\mathbf{U}_{z'}(\chi) = \left[\mathbf{U}_z(\phi)\mathbf{U}_y(\vartheta)\right]\mathbf{U}_z(\chi)\left[\mathbf{U}_z(\phi)\mathbf{U}_y(\vartheta)\right]^{-1}. \tag{A.3}$$

Consequently Eq. (A.2) can be rewritten as

$$\boldsymbol{e}_{\alpha'} = \mathbf{U}_z(\phi)\mathbf{U}_y(\vartheta)\mathbf{U}_z(\chi)\boldsymbol{e}_\alpha \quad \alpha = x, y, z. \tag{A.4}$$

Eq. (A.4) tells us that an equivalent way to obtain the MRF is to apply three excessive rotations $\mathbf{U}_z(\chi)$, $\mathbf{U}_y(\vartheta)$ and $\mathbf{U}_z(\phi)$ to the LRF. The three angles $\{\vartheta, \phi, \chi\}$ which connect the LRF and the MRF are called Euler angles [73].

Now let us consider vectors $\boldsymbol{R}_j$ characterized by spherical coordinates $(R_j, \theta_j, \varphi_j)$ in the MRF ($j = 1 - N$). With Eq. (A.4) and the rule between basis vectors and components transformations we can obtain the Cartesian components of these vectors in LRF

$$\begin{pmatrix} R_{jx} \\ R_{jy} \\ R_{jz} \end{pmatrix} = \mathbf{U}_z(\phi)\mathbf{U}_y(\vartheta)\mathbf{U}_z(\chi) \begin{pmatrix} R_{jx'} \\ R_{jy'} \\ R_{jz'} \end{pmatrix}, \tag{A.5}$$

where $R_{j\alpha}$ and $R_{j\alpha'}$ are Cartesian components of $\boldsymbol{R}_j$ in the LRF and the MRF, respectively. We can rewrite Eq. (A.5) in a more formal way for some other applications.

$$\boldsymbol{R}_j = R_j\mathbf{U}_z(\phi)\mathbf{U}_y(\vartheta)\mathbf{U}_z(\chi)\mathbf{U}_z(\varphi_j)\mathbf{U}_y(\theta_j)\boldsymbol{e}_z, \tag{A.6}$$

Eq. (A.6) is a vector equation, therefore, it is also valid for arbitrary reference frame.

Now we turn to the main task of deriving the Hermitian conjugate of momentum operators. This can be done step by step according to Eq. (2.8) with the help of the coordinates transformation Eq. (A.5). From Eq. (A.5) we can see that (θ_j, φ_j) only appear in the Cartesian components of $\boldsymbol{R}_j$. This greatly simplifies the expression for the Hermitian conjugates of momentum operators as follows

$$\begin{aligned}
\hat{P}^\dagger_{R_j} &= \hat{P}_{R_j} - i\hbar \sum_{\alpha=x,y,z} \left(\frac{\partial}{\partial R_{j\alpha}}\frac{\partial R_{j\alpha}}{\partial R_j}\right)^\circ \\
\hat{P}^\dagger_{\theta_j} &= \hat{P}_{\theta_j} - i\hbar \sum_{\alpha=x,y,z} \left(\frac{\partial}{\partial R_{j\alpha}}\frac{\partial R_{j\alpha}}{\partial \theta_j}\right)^\circ \\
\hat{P}^\dagger_{\varphi_j} &= \hat{P}_{\varphi_j} - i\hbar \sum_{\alpha=x,y,z} \left(\frac{\partial}{\partial R_{j\alpha}}\frac{\partial R_{j\alpha}}{\partial \varphi_j}\right)^\circ .
\end{aligned} \tag{A.7}$$

To calculate the derivatives in Eq. (A.7) the three Euler angles in Eq. (A.5) are purely parameters. We first write out some useful relations according the orthogonality of the transformation Eq. (A.5)

$$
\begin{aligned}
&R_{j\alpha} = \sum_{\beta'} \frac{\partial R_{j\alpha}}{\partial R_{j\beta'}} R_{j\beta'}, \qquad R_{j\beta'} = \sum_{\alpha} \frac{\partial R_{j\beta'}}{\partial R_{j\alpha}} R_{j\alpha} \\
&\sum_{\beta'} \left(\frac{\partial R_{j\alpha}}{\partial R_{j\beta'}} \right)^2 = \sum_{\alpha} \left(\frac{\partial R_{j\alpha}}{\partial R_{j\beta'}} \right)^2 = 1 \\
&\frac{\partial R_{j\alpha}}{\partial R_{j\beta'}} = \frac{\partial R_{j\beta'}}{\partial R_{j\alpha}}
\end{aligned}
\tag{A.8}
$$

where $\alpha = x, y, z$ and $\beta' = x', y', z'$. The last equation is just the property that $\mathbf{U}^{-1}$ is equal to $\mathbf{U}^T$ for an orthogonal matrix $\mathbf{U}$. Note that for the derivation purpose in this appendix all the derivatives $\{\frac{\partial R_{j\beta'}}{\partial R_{j\alpha}}\}$ are parameters only depends on the three Euler angles since we do not need to calculate derivatives with respect to the Euler angles.

Let us first derive the expression for $\hat{P}^{\dagger}_{R_j}$. It is straightforward to get the following derivatives of MRF Cartesian coordinates

$$
\begin{aligned}
\frac{\partial R_{jx'}}{\partial R_j} &= \sin\theta_j \cos\varphi_j = \frac{R_{jx'}}{R_j} \\
\frac{\partial R_{jy'}}{\partial R_j} &= \sin\theta_j \sin\varphi_j = \frac{R_{jy'}}{R_j} \\
\frac{\partial R_{jz'}}{\partial R_j} &= \cos\theta_j = \frac{R_{jz'}}{R_j}
\end{aligned}
\tag{A.9}
$$

where $R_j^2 = R_{jx}^2 + R_{jy}^2 + R_{jz}^2 = R_{jx'}^2 + R_{jy'}^2 + R_{jz'}^2$. Based on Eq. (A.9) we can obtain the derivatives of Cartesian coordinates in LRF with respect to R_j

$$
\frac{\partial R_{j\alpha}}{\partial R_j} = \sum_{\beta'} \frac{\partial R_{j\alpha}}{\partial R_{j\beta'}} \frac{\partial R_{j\beta'}}{\partial R_j} = \sum_{\beta'} \frac{R_{j\beta'}}{R_j} \frac{\partial R_{j\alpha}}{\partial R_{j\beta'}}. \tag{A.10}
$$

Then we can calculate $\left(\frac{\partial}{\partial R_{j\alpha}} \frac{\partial R_{j\alpha}}{\partial R_j} \right)^{\circ}$ based on Eq. (A.10)

$$
\begin{aligned}
\left(\frac{\partial}{\partial R_{j\alpha}} \frac{\partial R_{j\alpha}}{\partial R_j} \right)^{\circ} &= \sum_{\beta'} \left(\frac{1}{R_j} \frac{\partial R_{j\beta'}}{\partial R_{j\alpha}} + R_{j\beta'} \frac{\partial \left(R_{jx}^2 + R_{jy}^2 + R_{jz}^2 \right)^{-\frac{1}{2}}}{\partial R_{j\alpha}} \right) \frac{\partial R_{j\alpha}}{\partial R_{j\beta'}} \\
&= \sum_{\beta'} \left(\frac{1}{R_j} \frac{\partial R_{j\beta'}}{\partial R_{j\alpha}} - \frac{R_{j\beta'} R_{j\alpha}}{R_j^3} \right) \frac{\partial R_{j\alpha}}{\partial R_{j\beta'}}.
\end{aligned}
\tag{A.11}
$$

Making the summation we obtain the needed quantity for Eq. (A.7)

$$\begin{aligned}\sum_{\alpha}\left(\frac{\partial}{\partial R_{j\alpha}}\frac{\partial R_{j\alpha}}{\partial R_j}\right)^{\circ} &= \sum_{\alpha,\beta'}\left(\frac{1}{R_j}\frac{\partial R_{j\beta'}}{\partial R_{j\alpha}}-\frac{R_{j\beta'}R_{j\alpha}}{R_j^3}\right)\frac{\partial R_{j\alpha}}{\partial R_{j\beta'}}\\ &= \sum_{\alpha}\left(\frac{1}{R_j}-\frac{R_{j\alpha}^2}{R_j^3}\right)\\ &= \frac{3}{R_j}-\frac{1}{R_j}=\frac{2}{R_j},\end{aligned} \tag{A.12}$$

where Eq. (A.8) has been used at the first step. Finally we can get the HCMO associated with R_j

$$\hat{P}_{R_j}^{\dagger}=\hat{P}_{R_j}-\frac{2i\hbar}{R_j}=-i\hbar\frac{1}{R_j^2}\frac{\partial}{\partial R_j}R_j^2. \tag{A.13}$$

Next we will derive the expression for $\hat{P}_{\theta_j}^{\dagger}$ following the same procedure. The derivatives of MRF Cartesian coordinates read

$$\begin{aligned}\frac{\partial R_{jx'}}{\partial\theta_j} &= R_j\cos\theta_j\cos\varphi_j=R_{jx'}\cot\theta_j\\ \frac{\partial R_{jy'}}{\partial\theta_j} &= R_j\cos\theta_j\sin\varphi_j=R_{jy'}\cot\theta_j\\ \frac{\partial R_{jz'}}{\partial\theta_j} &= -R_j\sin\theta_j=-\frac{R_{jz'}}{\cot\theta_j}.\end{aligned} \tag{A.14}$$

Based on Eq. (A.14) we can obtain the derivatives of Cartesian coordinates in LRF with respect to θ_j

$$\frac{\partial R_{j\alpha}}{\partial\theta_j}=R_{jx'}\cot\theta_j\frac{\partial R_{j\alpha}}{\partial R_{jx'}}+R_{jy'}\cot\theta_j\frac{\partial R_{j\alpha}}{\partial R_{jy'}}-\frac{R_{jz'}}{\cot\theta_j}\frac{\partial R_{j\alpha}}{\partial R_{jz'}} \tag{A.15}$$

The next step is to calculate $\left(\frac{\partial}{\partial R_{j\alpha}}\frac{\partial R_{j\alpha}}{\partial\theta_j}\right)^{\circ}$. We will do it step by step in the following.

$$\begin{aligned}\left(\frac{\partial}{\partial R_{j\alpha}}\frac{\partial R_{j\alpha}}{\partial\theta_j}\right)^{\circ} &= \cot\theta_j\frac{\partial R_{j\alpha}}{\partial R_{jx'}}\frac{\partial R_{jx'}}{\partial R_{j\alpha}}+\cot\theta_j\frac{\partial R_{j\alpha}}{\partial R_{jy'}}\frac{\partial R_{jy'}}{\partial R_{j\alpha}}-\frac{1}{\cot\theta_j}\frac{\partial R_{j\alpha}}{\partial R_{jz'}}\frac{\partial R_{jz'}}{\partial R_{j\alpha}}\\ &\quad+\left(R_{jx'}\frac{\partial R_{j\alpha}}{\partial R_{jx'}}+R_{jy'}\frac{\partial R_{j\alpha}}{\partial R_{jy'}}+\frac{R_{jz'}}{\cot^2\theta_j}\frac{\partial R_{j\alpha}}{\partial R_{jz'}}\right)\frac{\partial\cot\theta_j}{\partial R_{j\alpha}}\\ &= \cot\theta_j-\frac{1}{\sin\theta_j\cos\theta_j}\frac{\partial R_{j\alpha}}{\partial R_{jz'}}\frac{\partial R_{jz'}}{\partial R_{j\alpha}}\\ &\quad+\left(R_{j\alpha}+(\tan^2\theta_j-1)R_{jz'}\frac{\partial R_{j\alpha}}{\partial R_{jz'}}\right)\frac{\partial\cot\theta_j}{\partial R_{j\alpha}}.\end{aligned} \tag{A.16}$$

Since $\cot\theta_j = \frac{R_{jz'}}{\sqrt{R_{jx'}^2+R_{jy'}^2}}$ we can get the following derivatives

$$\begin{aligned}
\frac{\partial \cot\theta_j}{\partial R_{jx'}} &= -\frac{R_{jx'}R_{jz'}}{\sqrt{R_{jx'}^2+R_{jy'}^2}^3} \\
\frac{\partial \cot\theta_j}{\partial R_{jy'}} &= -\frac{R_{jy'}R_{jz'}}{\sqrt{R_{jx'}^2+R_{jy'}^2}^3} \\
\frac{\partial \cot\theta_j}{\partial R_{jz'}} &= \frac{1}{\sqrt{R_{jx'}^2+R_{jy'}^2}}
\end{aligned} \tag{A.17}$$

Based on Eq. (A.17) we have

$$\begin{aligned}
\frac{\partial \cot\theta_j}{\partial R_{j\alpha}} &= \frac{1}{\sqrt{R_{jx'}^2+R_{jy'}^2}^3}\left(-R_{jx'}R_{jz'}\frac{\partial R_{jx'}}{\partial R_{j\alpha}} - R_{jy'}R_{jz'}\frac{\partial R_{jy'}}{\partial R_{j\alpha}} + (R_{jx'}^2+R_{jy'}^2)\frac{\partial R_{jz'}}{\partial R_{j\alpha}}\right) \\
&= \frac{1}{\sqrt{R_{jx'}^2+R_{jy'}^2}^3}\left(-R_{jz'}R_{j\alpha} + R_j^2\frac{\partial R_{jz'}}{\partial R_{j\alpha}}\right)
\end{aligned} \tag{A.18}$$

Combining Eq. (A.16) and Eq. (A.18) we can finally derive

$$\begin{aligned}
&\sum_\alpha \left(\frac{\partial}{\partial R_{j\alpha}}\frac{\partial R_{j\alpha}}{\partial \theta_j}\right)^\circ \\
=\ &\sum_\alpha \left(\cot\theta_j - \frac{1}{\sin\theta_j\cos\theta_j}\frac{\partial R_{j\alpha}}{\partial R_{jz'}}\frac{\partial R_{jz'}}{\partial R_{j\alpha}}\right) \\
+\ &\sum_\alpha \frac{1}{\sqrt{R_{jx'}^2+R_{jy'}^2}^3}\left(R_{j\alpha} + (\tan^2\theta_j - 1)R_{jz'}\frac{\partial R_{j\alpha}}{\partial R_{jz'}}\right)\left(-R_{jz'}R_{j\alpha} + R_j^2\frac{\partial R_{jz'}}{\partial R_{j\alpha}}\right) \\
=\ &3\cot\theta_j - \frac{1}{\sin\theta_j\cos\theta_j} \\
+\ &\frac{1}{\sqrt{R_{jx'}^2+R_{jy'}^2}^3}\left(-R_{jz'}R_j^2 + R_j^2R_{jz'} + (\tan^2\theta_j - 1)(-R_{jz'}^2R_{jz'} + R_j^2R_{jz'})\right) \\
=\ &3\cot\theta_j - \frac{1}{\sin\theta_j\cos\theta_j} + (\tan^2\theta_j - 1)\cot\theta_j \\
=\ &\cot\theta_j
\end{aligned} \tag{A.19}$$

The Hermitian conjugate of each $\hat{P}_{\theta_j}$ associated with the corresponding MRF polar angle θ_j can be finally expressed as

$$\hat{P}_{\theta_j}^\dagger = \hat{P}_{\theta_j} - i\hbar\cot\theta_j = -\frac{i\hbar}{\sin\theta_j}\frac{\partial}{\partial\theta_j}\sin\theta_j. \tag{A.20}$$

Finally we come to $\hat{P}^{\dagger}_{\varphi_j}$. The procedure is the same however it is much more simple compared to $\hat{P}^{\dagger}_{\theta_j}$. First the derivatives of MRF Cartesian coordinates read

$$\begin{aligned}
\frac{\partial R_{jx'}}{\partial \varphi_j} &= -R_j \sin\theta_j \sin\varphi_j = -R_{jy'} \\
\frac{\partial R_{jy'}}{\partial \varphi_j} &= R_j \sin\theta_j \cos\varphi_j = R_{jx'} \\
\frac{\partial R_{jz'}}{\partial \varphi_j} &= 0.
\end{aligned} \tag{A.21}$$

Then the derivatives of LRF Cartesian coordinates read

$$\frac{\partial R_{j\alpha}}{\partial \varphi_j} = R_{jx'} \frac{\partial R_{j\alpha}}{\partial R_{jy'}} - R_{jy'} \frac{\partial R_{j\alpha}}{\partial R_{jx'}}. \tag{A.22}$$

The final summation of needed derivatives is

$$\left(\sum_{\alpha} \frac{\partial}{\partial R_{j\alpha}} \frac{\partial R_{j\alpha}}{\partial \varphi_j} \right)^{\circ} = \sum_{\alpha} \left(\frac{\partial R_{jx'}}{\partial R_{j\alpha}} \frac{\partial R_{j\alpha}}{\partial R_{jy'}} - \frac{\partial R_{jy'}}{\partial R_{j\alpha}} \frac{\partial R_{j\alpha}}{\partial R_{jx'}} \right) = 0 \tag{A.23}$$

The momentum operator associated with each orientation angle φ_j is Hermitian according to Eq. (A.23), namely

$$\hat{P}^{\dagger}_{\varphi_j} = \hat{P}_{\varphi_j} = -i\hbar \frac{\partial}{\partial \varphi_j}. \tag{A.24}$$

Now let us recall the above detailed procedure. The only condition we need is that the transformation matrix between Cartesian coordinates in the LRF and those in a MRF is orthogonal. First, if we set all the three Euler angles equal to zero we can obtain the HCMOs associated with spherical coordinates in the LRF. The final results are the same with Eq. (A.13), Eq. (A.20) and Eq. (A.24) since a unit matrix is also an orthogonal matrix. Second, we can use more rotations to define more MRFs and the HCOMs associated with the spherical coordinates in each different MRF obey Eq. (A.13), Eq. (A.20) and Eq. (A.24). As an important consequence the Hermitian conjugates of all the momentum operators associated with *real* bond lengths, bond angles and dihedral angles obey Eq. (A.13), Eq. (A.20) and Eq. (A.24) respectively irrespective of how complicated the molecule might be. Similarly, the result holds for any reference frame provided there exists an orthogonal transformation to transform it to the LRF. Base on above mentioned conclusions we can see the HCMOs associated with the three Euler angles obey the same relations

$$\begin{aligned}
\hat{P}^{\dagger}_{\vartheta} &= \hat{P}_{\vartheta} - i\hbar \cot\vartheta = -\frac{i\hbar}{\sin\vartheta} \frac{\partial}{\partial \vartheta} \sin\vartheta \\
\hat{P}^{\dagger}_{\phi} &= \hat{P}_{\phi} = -i\hbar \frac{\partial}{\partial \phi} \\
\hat{P}^{\dagger}_{\chi} &= \hat{P}_{\chi} = -i\hbar \frac{\partial}{\partial \chi}.
\end{aligned} \tag{A.25}$$

We can obtain the HCMOs $\hat{P}^{\dagger}_{j\beta'}$ associated with MRF Cartesian coordinates following the same procedure. Since $\frac{\partial R_{j\alpha}}{\partial R_{j\beta'}}$ is just a parameter which does not explicitly depends on R_{jx}, R_{jy} or R_{jz} according to Eq. (A.5), we can easily obtain the HCMOs associated with MRF Cartesian coordinates

$$\begin{aligned} \hat{P}^{\dagger}_{j\beta'} &= \hat{P}_{j\beta'} - i\hbar \sum_{\alpha} \left(\frac{\partial}{\partial R_{j\alpha}} \frac{\partial R_{j\alpha}}{\partial R_{j\beta'}} \right)^{\circ} \\ &= \hat{P}_{j\beta'}, \end{aligned} \tag{A.26}$$

where $\beta' = x', y', z'$. We can see the momenta associated with MRF Cartesian coordinates are Hermitian.

In general we have great freedom to define spherical coordinates, Cartesian coordinates or combination of both with one or several MRFs. The corresponding HCMOs are just the same as HCMOs associated with the LRF coordinates if the only difference between the LRF and the corresponding MRF is an orthogonal transformation. Typically an orthogonal transformation may be a rotation or product of many excessive rotations since product of many orthogonal matrices is still an orthogonal matrix. This will cover most of the cases we may encounter therefore our kinetic energy quantization procedure can be easily applied to them.

Appendix B

KEO in Terms of Polyspherical Coordinates

As an example we will consider the KEO in terms of so called polyspherical coordinates [78] defined in the LRF and a MRF. The LRF and the MRF are connected by three Euler angles (ϑ, ϕ, χ) as detailed in Appendix A

$$\boldsymbol{e}_{\alpha'} = \mathbf{U}_z(\phi)\mathbf{U}_y(\vartheta)\mathbf{U}_z(\chi)\boldsymbol{e}_\alpha, \quad \alpha = x, y, z. \tag{B.1}$$

Consider a molecular system composed of $N+1$ atoms. After separating the total center of mass motion we can describe it with N Jacobi vectors $\boldsymbol{R}_1$, $\boldsymbol{R}_2$, $\cdots$, $\boldsymbol{R}_N$. The three Euler angles (ϑ, ϕ, χ) are chosen in such a way that the spherical coordinates of $\boldsymbol{R}_N$ in the LRF are (R_N, ϑ, ϕ) and the spherical coordinates of $\boldsymbol{R}_1$ in the MRF are $(R_1, \theta_1, \varphi_1 = 0)$. That is to say the $\boldsymbol{e}_{z'}$ axis of the MRF is defined to be along the direction of $\boldsymbol{R}_N$. The remaining $N-2$ vectors are characterized by spherical coordinates $\{R_j, \theta_j, \varphi_j\}$ in the MRF $(j = 2, \cdots, N-1)$. In the following we will establish the KEO in terms of the $3N$ coordinates mentioned above.

According to Appendix A we can express the N vectors as

$$\boldsymbol{R}_j = R_j\mathbf{U}_z(\phi)\mathbf{U}_y(\vartheta)\mathbf{U}_z(\chi)\mathbf{U}_z(\varphi_j)\mathbf{U}_y(\theta_j)\boldsymbol{e}_z, \tag{B.2}$$

where $j = 1, \cdots, N$ and $\theta_N = \varphi_N = \varphi_1 = 0$. With the help of Eq. (B.2) we can derive

the LRF components of the N velocity vectors

$$\begin{aligned}
\dot{\boldsymbol{R}}_j &= R_j\dot{\vartheta}\mathbf{U}_z(\phi)\mathbf{U}'_y(\vartheta)\mathbf{U}_z(\chi)\mathbf{U}_z(\varphi_j)\mathbf{U}_y(\theta_j)\boldsymbol{e}_z \\
&+ R_j\dot{\phi}\mathbf{U}'_z(\phi)\mathbf{U}_y(\vartheta)\mathbf{U}_z(\chi)\mathbf{U}_z(\varphi_j)\mathbf{U}_y(\theta_j)\boldsymbol{e}_z \\
&+ R_j\dot{\chi}\mathbf{U}_z(\phi)\mathbf{U}_y(\vartheta)\mathbf{U}'_z(\chi)\mathbf{U}_z(\varphi_j)\mathbf{U}_y(\theta_j)\boldsymbol{e}_z \\
&+ \dot{R}_j\mathbf{U}_z(\phi)\mathbf{U}_y(\vartheta)\mathbf{U}_z(\chi)\mathbf{U}_z(\varphi_j)\mathbf{U}_y(\theta_j)\boldsymbol{e}_z \\
&+ R_j\dot{\theta}_j\mathbf{U}_z(\phi)\mathbf{U}_y(\vartheta)\mathbf{U}_z(\chi)\mathbf{U}_z(\varphi_j)\mathbf{U}'_y(\theta_j)\boldsymbol{e}_z \\
&+ R_j\dot{\varphi}_j\mathbf{U}_z(\phi)\mathbf{U}_y(\vartheta)\mathbf{U}_z(\chi)\mathbf{U}'_z(\varphi_j)\mathbf{U}_y(\theta_j)\boldsymbol{e}_z, \qquad \text{(B.3)}
\end{aligned}$$

where $\mathbf{U}'$ is the first order derivative of the corresponding rotational transformation matrix. The above equations are still vector equations however they are only valid in the LRF since we have used the relation $\dot{\boldsymbol{e}}_z = 0$. To make them valid in arbitrary reference frame we only need to add the corresponding terms consisting $\dot{\boldsymbol{e}}_z$ to the right side. However, it is not needed for our purpose.

It is better to discuss the orthogonality of the terms appeared in Eq. (B.3) before further derivation. The last three terms in Eq. (B.3) are just the spherical velocity components measured in the MRF while the first three terms are components of the velocity caused by the non-inertial MRF. Each term in Eq. (B.3) can be expressed in a formally simple way in terms of angular velocity vectors

$$\begin{aligned}
\dot{\boldsymbol{R}}_j &= \dot{\vartheta}\boldsymbol{e}_{\dot{\vartheta}} \times \boldsymbol{R}_j + \dot{\phi}\boldsymbol{e}_{\dot{\phi}} \times \boldsymbol{R}_j + \dot{\chi}\boldsymbol{e}_{\dot{\chi}} \times \boldsymbol{R}_j \\
&+ \dot{R}_j\boldsymbol{R}_j/R_j + \dot{\theta}_j\boldsymbol{e}_{\dot{\theta}_j} \times \boldsymbol{R}_j + \dot{\varphi}_j\boldsymbol{e}_{\dot{\varphi}_j} \times \boldsymbol{R}_j, \qquad \text{(B.4)}
\end{aligned}$$

where $\boldsymbol{e}_{\dot{\vartheta}}$ is the direction of the angular velocity $\dot{\vartheta}$, and similar for $\boldsymbol{e}_{\dot{\phi}}$, $\boldsymbol{e}_{\dot{\chi}}$, $\boldsymbol{e}_{\dot{\theta}_j}$ and $\boldsymbol{e}_{\dot{\varphi}_j}$. According to Eq. (B.4) one can immediately see that the fourth term is parallel to $\boldsymbol{R}_j$ while the other terms are perpendicular to $\boldsymbol{R}_j$. Recalling the velocity in spherical coordinates we know that the last three terms are orthogonal to each other. Therefore, in Eq. (B.3) (or Eq. (B.4)), the fourth term (namely the $\dot{R}_j$ term) is orthogonal to the other terms and the last three terms are orthogonal to each other.

Having at hand all the velocities it is quite straightforward to write the classical kinetic energy according to

$$T = \frac{1}{2}\sum_{j=1}^{N}\mu_j\dot{\boldsymbol{R}}_j^{\dagger}\dot{\boldsymbol{R}}_j. \qquad \text{(B.5)}$$

If non-Jacobi vectors are used the kinetic energy obeys a more general form $T = \frac{1}{2}\sum_{j,k=1}^{N}\mu_{jk}\dot{\boldsymbol{R}}_j^{\dagger}\dot{\boldsymbol{R}}_k$ with a matrix $\{\mu_{jk}\}$ combines the reduced masses and the transformation matrix between adopted vectors and Jacobi vectors [121]. The final results in LRF

can be easily written as a symmetric form

$$T = \frac{1}{2}\dot{\boldsymbol{Q}}^{\dagger}\mathbf{M}\dot{\boldsymbol{Q}}, \qquad \boldsymbol{Q} = \begin{pmatrix} \boldsymbol{Q}_{rot} \\ \boldsymbol{Q}_{vib} \end{pmatrix}, \tag{B.6}$$

where the coordinates are separated as rotational and vibrational DOFs

$$\begin{aligned} \boldsymbol{Q}_{rot}^{\dagger} &= \begin{pmatrix} \vartheta & \phi & \chi \end{pmatrix}, \\ \boldsymbol{Q}_{vib}^{\dagger} &= \begin{pmatrix} R_1 & \cdots & R_N & \theta_1 & \cdots & \theta_{N-1} & \varphi_2 & \cdots & \varphi_{N-1} \end{pmatrix}. \end{aligned}$$

The only difference between Jacobi- and non-Jacobi- vectors is that in the latter case the generalized mass matrix **M** has more non-zero matrix elements. For Jacobi vectors there is no vibrational couplings, and no Coriolis couplings involving $\dot{R}_j$ according to the discussions of orthogonality about Eq. (B.3). In this case it is also quite transparent to get each non-zero matrix element of **M** according to Eq. (B.3), e.g.,

$$\begin{aligned} &\mathrm{M}_{\vartheta\varphi_{\mathrm{j}}} = \mathrm{M}_{\varphi_{\mathrm{j}}\vartheta} \\ &= \mu_j R_j R_N \boldsymbol{e}_z^{\dagger}\mathbf{U}_y(\theta_j)^{\dagger}\mathbf{U}_z(\varphi_j)^{\dagger}\mathbf{U}_z(\chi)^{\dagger}\mathbf{U}_y'(\vartheta)^{\dagger}\mathbf{U}_z(\phi)^{\dagger}\mathbf{U}_z(\phi)\mathbf{U}_y(\vartheta)\mathbf{U}_z(\chi)\mathbf{U}_z'(\varphi_j)\mathbf{U}_y(\theta_j)\boldsymbol{e}_z \\ &= \mu_j R_j R_N \boldsymbol{e}_z^{\dagger}\mathbf{U}_y(-\theta_j)\mathbf{U}_z(-\varphi_j)\mathbf{U}_z(-\chi)\mathbf{U}_y'(\vartheta)^{\dagger}\mathbf{U}_y(\vartheta)\mathbf{U}_z(\chi)\mathbf{U}_z'(\varphi_j)\mathbf{U}_y(\theta_j)\boldsymbol{e}_z. \end{aligned}$$

Next step is to calculate the inverse matrix of **M** to generate the quantum KEO. Aiming at the separation of the rotational and vibrational DOFs, we divide the matrix **M** into the following four blocks

$$\mathbf{M} = \begin{pmatrix} \mathbf{M}_{rot} & \mathbf{M}_{Cor} \\ \mathbf{M}_{Cor}^{\dagger} & \mathbf{M}_{vib} \end{pmatrix}, \tag{B.7}$$

where the subscripts $_{rot}$, $_{Cor}$ and $_{vib}$ correspond to rotational, Coriolis and vibrational terms, respectively. That is to say $\mathbf{M}_{rot}$, $\mathbf{M}_{Cor}$ and $\mathbf{M}_{vib}$ are 3×3, $3 \times (3N-3)$ and $(3N-3) \times (3N-3)$ dimensional matrices, respectively. Suppose the inverse matrix of **M** is divided in the same spirit as

$$\mathbf{M}^{-1} = \begin{pmatrix} \mathbf{G}_{rot} & \mathbf{G}_{Cor} \\ \mathbf{G}_{Cor}^{\dagger} & \mathbf{G}_{vib} \end{pmatrix}, \tag{B.8}$$

we can express the quantum KEO as a sum of rotational, vibrational and Coriolis terms

$$\begin{aligned} \hat{T} &= \hat{T}_{rot} + \hat{T}_{vib} + \hat{T}_{Cor} \\ &= \frac{1}{2}\hat{\boldsymbol{P}}_{rot}^{\dagger}\mathbf{G}_{rot}\hat{\boldsymbol{P}}_{rot} + \frac{1}{2}\hat{\boldsymbol{P}}_{vib}^{\dagger}\mathbf{G}_{vib}\hat{\boldsymbol{P}}_{vib} + \frac{1}{2}\left(\hat{\boldsymbol{P}}_{rot}^{\dagger}\mathbf{G}_{Cor}\hat{\boldsymbol{P}}_{vib} + h.c.\right). \end{aligned} \tag{B.9}$$

According to Section 2.2.5, the generalized momentum vector $\hat{\boldsymbol{P}}_{rot}$ associated with the rotational DOFs is just the total angular momentum vector $\boldsymbol{J}$. If we are interested in the rotational DOFs we can exploit the rotational Hamiltonian at the vibrational ground state. The corresponding KEO reads

$$\hat{T}_{rot} = \frac{1}{2}\hat{\boldsymbol{P}}^{\dagger}_{rot}\mathbf{G}_{rot}\hat{\boldsymbol{P}}_{rot} = \frac{1}{2}\hat{\boldsymbol{J}}^{\dagger}\mathbf{G}_{rot}\hat{\boldsymbol{J}}, \tag{B.10}$$

where the components of $\boldsymbol{J}$ should be along the directions of $\boldsymbol{e}_{\vartheta}$, $\boldsymbol{e}_{\dot{\phi}}$ and $\boldsymbol{e}_{\dot{\chi}}$ according to Eq. (2.32). One can also transform the components to Cartesian ones according to Eq. (2.33). On the other hand, if we are interested in the vibrational DOFs, the KEO for the total angular momentum $\boldsymbol{J} = 0$ reads

$$\hat{T}_{vib} = \frac{1}{2}\hat{\boldsymbol{P}}^{\dagger}_{vib}\mathbf{G}_{vib}\hat{\boldsymbol{P}}_{vib}. \tag{B.11}$$

Now we will give details on how to calculate the different blocks of the inverse matrix of $\mathbf{M}$. One can see that the matrix $\mathbf{M}$ can be congruently block-diagonalized in the following way

$$\begin{aligned}
&\begin{pmatrix} \mathbf{1} & -\mathbf{M}_{Cor}\mathbf{M}_{vib}^{-1} \\ \mathbf{0} & \mathbf{1} \end{pmatrix}
\begin{pmatrix} \mathbf{M}_{rot} & \mathbf{M}_{Cor} \\ \mathbf{M}_{Cor}^{\dagger} & \mathbf{M}_{vib} \end{pmatrix}
\begin{pmatrix} \mathbf{1} & \mathbf{0} \\ -\mathbf{M}_{vib}^{-1}\mathbf{M}_{Cor}^{\dagger} & \mathbf{1} \end{pmatrix} \\
&= \begin{pmatrix} \mathbf{M}_{rot} - \mathbf{M}_{Cor}\mathbf{M}_{vib}^{-1}\mathbf{M}_{Cor}^{\dagger} & \mathbf{0} \\ \mathbf{0} & \mathbf{M}_{vib} \end{pmatrix}.
\end{aligned} \tag{B.12}$$

Calculating the inverse of both side of Eq. (B.12) leads to

$$\begin{aligned}
\mathbf{M}^{-1} &= \begin{pmatrix} \mathbf{G}_{rot} & \mathbf{G}_{Cor} \\ \mathbf{G}_{Cor}^{\dagger} & \mathbf{G}_{vib} \end{pmatrix} = \begin{pmatrix} \mathbf{M}_{rot} & \mathbf{M}_{Cor} \\ \mathbf{M}_{Cor}^{\dagger} & \mathbf{M}_{vib} \end{pmatrix}^{-1} \\
&= \begin{pmatrix} \mathbf{1} & \mathbf{0} \\ -\mathbf{M}_{vib}^{-1}\mathbf{M}_{Cor}^{\dagger} & \mathbf{1} \end{pmatrix}
\begin{pmatrix} \mathbf{M}_{rot} - \mathbf{M}_{Cor}\mathbf{M}_{vib}^{-1}\mathbf{M}_{Cor}^{\dagger} & \mathbf{0} \\ \mathbf{0} & \mathbf{M}_{vib} \end{pmatrix}^{-1}
\begin{pmatrix} \mathbf{1} & -\mathbf{M}_{Cor}\mathbf{M}_{vib}^{-1} \\ \mathbf{0} & \mathbf{1} \end{pmatrix}.
\end{aligned} \tag{B.13}$$

Calculating the matrix product in above equation leads to the final results

$$\begin{aligned}
\mathbf{G}_{rot} &= \left(\mathbf{M}_{rot} - \mathbf{M}_{Cor}\mathbf{M}_{vib}^{-1}\mathbf{M}_{Cor}^{\dagger}\right)^{-1} \\
\mathbf{G}_{Cor} &= -\mathbf{G}_{rot}\mathbf{M}_{Cor}\mathbf{M}_{vib}^{-1} \\
\mathbf{G}_{vib} &= \mathbf{M}_{vib}^{-1} + \mathbf{M}_{vib}^{-1}\mathbf{M}_{Cor}^{\dagger}\mathbf{G}_{Cor}.
\end{aligned} \tag{B.14}$$

For the special case of Jacobi vectors, $\mathbf{M}_{vib}$ is diagonal which will greatly simplify the calculation of Eq. (B.14). It is straightforward to obtain the diagonal elements according to Eq. (B.3)

$$\begin{aligned}
(\mathbf{M}_{vib})_{R_jR_j} &= \mu_j \\
(\mathbf{M}_{vib})_{\theta_j\theta_j} &= \mu_j R_j^2 \\
(\mathbf{M}_{vib})_{\varphi_j\varphi_j} &= \mu_j R_j^2 \sin^2\theta_j.
\end{aligned} \tag{B.15}$$

The inverse matrix of $\mathbf{M}_{vib}$ is quite trivial. We only need to calculate the inverse matrix of 3×3 dimension as well as some matrix products to get the final results. The results are essentially the same with what have been reported in Ref. [78]. In the following we give the matrix elements for $\mathbf{G}_{vib}$ (Hermitian) which are required in Appendix C.

$$\begin{aligned}
G_{R_iR_j} &= \frac{\delta_{ij}}{\mu_j}, \qquad G_{R_i\theta_j} = 0, \qquad G_{R_i\varphi_j} = 0, \\
G_{\theta_i\theta_j} &= \frac{\delta_{ij}}{\mu_j R_j^2} + \frac{\cos(\varphi_i-\varphi_j)}{\mu_N R_N^2}, \\
G_{\theta_i\varphi_j} &= \frac{\cot\theta_j \sin(\varphi_i-\varphi_j) - \cot\theta_1 \sin\varphi_i}{\mu_N R_N^2}, \\
G_{\varphi_i\varphi_j} &= \frac{\delta_{ij}}{\mu_j R_j^2 \sin^2\theta_j} + \frac{1}{\mu_1 R_1^2 \sin^2\theta_1} \\
&+ \frac{\cot\theta_i \cot\theta_j \cos(\varphi_i-\varphi_j) + \cot^2\theta_1 - \cot\theta_1(\cos\varphi_i \cot\theta_i + \cos\varphi_j \cot\theta_j)}{\mu_N R_N^2}
\end{aligned}$$

Appendix C

9D KEO for $H_3O_2^-$ and its Isotopomers

In this chapter we derive the 9D vibrational KEO for $H_3O_2^-$. The coordinates are defined in the MRF characterized by three Euler angles (ϑ, ϕ, χ) as detailed in Appendix A. The four Jacobi vectors shown in Fig. 4.1 are adopted. The three Euler angles are chosen in the same way as introduced in Appendix B, i.e., the MRF spherical coordinates $\boldsymbol{R}_4$ and $\boldsymbol{R}_1$ are $(R_4, 0, 0)$ and $(R_1, \theta_1, 0)$, respectively. The other two vectors can be characterized by their spherical coordinates in the MRF $(R_j, \theta_j, \varphi_j)$ ($j = 2, 3$). According to the conclusion of Appendix B we can write out the exact 9D KEO for the total angular momentum $\boldsymbol{J} = 0$ directly. However, to make things less intricate, we assume some approximations. The basic idea is to introduce a new MRF with ignorable angular velocities and express $\boldsymbol{R}_3$ with Cartesian coordinates (x, y, z). The remaining six coordinates are spherical coordinates in the old MRF $(R_1, R_2, \theta_1, \theta_2, R_4, \varphi = \varphi_2 - \varphi_1 = \varphi_2)$.

The new MRF is associated with the old MRF by a rotation of angle $\eta\varphi$ around the $\boldsymbol{R}_4$ (the z-axis). The spherical coordinates for $\boldsymbol{R}_3$ in the new MRF are $(R_3, \theta_3, \tilde{\varphi_3})$ with

$$\tilde{\varphi_3} = \varphi_3 - \eta\varphi, \tag{C.1}$$

where $\eta = \mu_1/(\mu_1 + \mu_2)$ is defined to minimize the Coriolis type couplings involving the central hydrogen so that we can ignore them. And μ_1 (μ_2) is the reduced mass associated with the Jacobi vector $\boldsymbol{R}_1$ ($\boldsymbol{R}_2$). The Cartesian coordinates for the central proton read

$$\begin{aligned} x &= R_3 \sin\theta_3 \cos\tilde{\varphi_3} \\ y &= R_3 \sin\theta_3 \sin\tilde{\varphi_3} \\ z &= R_3 \cos\theta_3 \end{aligned} \tag{C.2}$$

and the KEO for it is simply

$$T_3 = -\frac{\hbar^2}{2\mu_3}\left(\frac{\partial^2}{\partial x^2} + \frac{\partial^2}{\partial y^2} + \frac{\partial^2}{\partial z^2}\right), \tag{C.3}$$

where μ_3 is the reduced mass associated with the Jacobi vector $\boldsymbol{R}_3$ and Coriolis terms are ignored. Since the direction $\boldsymbol{e}'_z$ is defined along the direction of $\boldsymbol{R}_4$, the z coordinate corresponds to the central hydrogen stretching mode.

For the rest 6 DOFs concerning the $(OH)_2$ fragment, the 6D KEO is written out according to Appendix B. Similar to the idea adopted in Chapter 2, we take the angular momentum of the $(OH)_2$ fragment as total angular momentum. Combining the central proton part and the $(OH)_2$ fragment we finally obtain the 9D KEO. The new coordinates $u_i = \cos\theta_i$ ($i = 1, 2$) have been used. For the simulation an additional normalization transform as detailed in Chapter 3 was performed to reduce the numerical effort. This gives the following 9D KEO:

$$T = T_1 + T_2 + T_3$$

with

$$T_1 = -\frac{\hbar^2}{2\mu_1}\frac{\partial^2}{\partial R_1^2} - \frac{\hbar^2}{2\mu_2}\frac{\partial^2}{\partial R_2^2} - \frac{\hbar^2}{2\mu_4}\frac{\partial^2}{\partial R_4^2}$$

$$\begin{aligned}
T_2 = & -\left(\frac{1}{2\mu_1 R_1^2} + \frac{1}{2\mu_4 R_4^2}\right)\frac{\partial}{\partial u_1}(1-u_1^2)\frac{\partial}{\partial u_1} - \left(\frac{1}{2\mu_2 R_2^2} + \frac{1}{2\mu_4 R_4^2}\right)\frac{\partial}{\partial u_2}(1-u_2^2)\frac{\partial}{\partial u_2} \\
& -\frac{1}{2\mu_4 R_4^2}\left(\sqrt{1-u_1^2}\frac{\partial}{\partial u_1}\frac{\partial}{\partial u_2}\sqrt{1-u_2^2} + \frac{\partial}{\partial u_1}\sqrt{1-u_1^2}\sqrt{1-u_2^2}\frac{\partial}{\partial u_2}\right) \\
& -\sum_{i=1,2}\left(\frac{1}{2\mu_i R_i^2}\frac{1}{1-u_i^2} + \frac{1}{2\mu_4 R_4^2}\frac{u_i^2}{1-u_i^2}\right)\frac{\partial^2}{\partial\varphi^2} \\
& +\frac{1}{\mu_4 R_4^2}\frac{u_1}{\sqrt{1-u_1^2}}\frac{u_2}{\sqrt{1-u_2^2}}\frac{\partial}{\partial\varphi}\cos\varphi\frac{\partial}{\partial\varphi} \\
& -\frac{1}{2\mu_4 R_4^2}\frac{u_2}{\sqrt{1-u_2^2}}\left(\frac{\partial}{\partial\varphi}\sin\varphi\sqrt{1-u_1^2}\frac{\partial}{\partial u_1} + \frac{\partial}{\partial u_1}\sqrt{1-u_1^2}\sin\varphi\frac{\partial}{\partial\varphi}\right) \\
& -\frac{1}{2\mu_4 R_4^2}\frac{u_1}{\sqrt{1-u_1^2}}\left(\frac{\partial}{\partial\varphi}\sin\varphi\sqrt{1-u_2^2}\frac{\partial}{\partial u_2} + \frac{\partial}{\partial u_2}\sqrt{1-u_2^2}\sin\varphi\frac{\partial}{\partial\varphi}\right).
\end{aligned}$$

The non-Euclidean normalization according to the volume element is $d_\tau = dR_1 dR_2 dR_4 dx dy dz du_1 du_2 d\varphi$. The reduced masses are defined as follows: $HOHOH^-$ – $\mu_1 = \mu_2 = m_H m_O/(m_H + m_O)$, $\mu_3 = 2m_H(m_H + m_O)/(3m_H + 2m_O)$, $\mu_4 = (m_H + m_O)/2$; $HODOH^-$ – $\mu_3 = 2m_D(m_H + m_O)/(m_D + 2m_H + 2m_O)$; $HOHOD^-$ – $\mu_1 = m_D m_O/(m_H + m_O)$ and μ_3 and μ_4 change correspondingly. For $DODOD^-$ the corresponding masses of $HOHOH^-$ are modified by replacing m_H by m_D. In the same way we get the masses for $DOHOD^-$ by exchanging m_H and m_D in $HODOH^-$, and similarly one can obtain $DODOH^-$ from $DOHOH^-$.

Appendix D

Infrared Absorption Spectrum Theory

We want to investigate the infrared absorption spectra of molecules in the gas phase. First we would like to recall certain general theory for light induced excitations. The following theory in this appendix is adapted from Ref. [120]. The total Hamiltonian in the interaction picture includes three parts

$$H = H_s + H_{sf} + H_f \tag{D.1}$$

where H_s and H_f describe the system we are interested in and the external electric field, respectively. The interaction between the two subsystems is described by H_{sf}. The external field will be treated classically and we mainly focus on the molecule-light interaction induced state transfer in the molecular system. Let us start from the golden rule which characterizes this kind of transfer rate

$$k(\omega) = \frac{2\pi}{\hbar} \sum_{fi} P(E_i) |\langle f|H_{sf}|i\rangle|^2 \delta(\hbar\omega - E_{fi}) \tag{D.2}$$

where ω is the frequency of the external electrical field and $P(E_i) = \frac{\exp(-E_i/K_BT)}{\mathrm{Tr}(e^{-H_s/K_BT})}$ is the thermal weight of the ith initial state. The linear absorption coefficient which characterizes the exponential decay of the filed intensity along the propagation direction can be obtained as

$$\begin{aligned} \alpha(\omega) &= \frac{n\hbar\omega}{I_0} k(\omega) \\ &= \frac{2\pi n\omega}{I_0} \sum_{fi} P(E_i) |\langle f|H_{sf}|i\rangle|^2 \delta(\hbar\omega - E_{fi}) \\ &= \frac{n\omega}{\hbar I_0} \int_{-\infty}^{\infty} \mathrm{Tr}[W_{eq} H_{sf}(t) H_{sf}] dt \end{aligned} \tag{D.3}$$

where n is the density of molecules and I_0 is the field intensity in free space. In the last equation the Fourier transform of delta function $\delta(\omega) = \frac{1}{2\pi}\int_{-\infty}^{\infty} e^{i\omega t} dt$ was applied

and we replace one summation by the equilibrium molecular density operator $W_{eq} = \sum_i P(E_i)|i\rangle\langle i|$. The time dependent operators are defined in the Heisenberg picture with respect to H_s, i.e., $H_{sf}(t) = e^{iH_s t/\hbar} H_{sf} e^{-iH_s t/\hbar}$.

In the weak field limit it is reasonable to use the dipole interaction. The electrical field change due to the molecular response is neglected, and in the small range of the molecular volume the electric field can be regarded as a constant. Thus the interaction Hamiltonian reads

$$\begin{aligned} H_{sf} &= -\frac{1}{2}\left(\boldsymbol{\mu}^\dagger \boldsymbol{E} + \boldsymbol{E}^\dagger \boldsymbol{\mu}\right) \\ &= -\sum_{\gamma=x,y,z} \mu_\gamma E_\gamma, \end{aligned} \tag{D.4}$$

where $\boldsymbol{\mu}$ and $\boldsymbol{E}$ are molecular dipole moment operator and amplitude of electric field, respectively. In general it is more convenient to describe dipole moment in MRF. Considering the MRF described by three Euler angles $\{\theta, \phi, \chi\}$ and LRF with $\boldsymbol{e}_z$ in the same direction as $\boldsymbol{E}$ we can rewrite the interaction Hamiltonian as

$$\begin{aligned} H_{sf} &= -\sum_{\gamma'=x',y',z'} \mu_{\gamma'} E_{\gamma'} \\ &= -\begin{pmatrix} \mu_{x'} & \mu_{y'} & \mu_{z'} \end{pmatrix} [\mathbf{U}_z(\phi)\mathbf{U}_y(\theta)\mathbf{U}_z(\chi)]^{-1} \begin{pmatrix} 0 \\ 0 \\ E \end{pmatrix} \\ &= \mu_{x'} E \sin\theta\cos\chi - \mu_{y'} E \sin\theta\sin\chi - \mu_{z'} E\cos\theta. \end{aligned} \tag{D.5}$$

Introduce the above interaction Hamiltonian to Eq. (D.3) and after average over all orientations (which are assumed to be randomly orientated) we have

$$\alpha(\omega) = \frac{2n\omega}{3c\varepsilon_0\hbar} \int_{-\infty}^{\infty} \sum_{m\gamma} P(E_m) e^{iE_m t/\hbar} \langle m|\mu_\gamma e^{-iH_s t}\mu_\gamma|m\rangle dt \tag{D.6}$$

where c is the light velocity in the molecular medium and $I_0 = c\varepsilon_0 E^2/2 = c\varepsilon_0 \sum_\gamma E_\gamma^2/2$ has been used. The average values of related quantities are

$$\begin{aligned} \langle(\sin\theta\cos\chi)^2\rangle_\Omega &= \frac{\int_0^\pi\int_0^{2\pi}\int_0^{2\pi}(\sin\theta\cos\chi)^2\sin\theta d\theta d\phi d\chi}{\int_0^\pi\int_0^{2\pi}\int_0^{2\pi}\sin\theta d\theta d\phi d\chi} = \frac{1}{3} \\ \langle(\sin\theta\sin\chi)^2\rangle_\Omega &= \frac{\int_0^\pi\int_0^{2\pi}\int_0^{2\pi}(\sin\theta\sin\chi)^2\sin\theta d\theta d\phi d\chi}{\int_0^\pi\int_0^{2\pi}\int_0^{2\pi}\sin\theta d\theta d\phi d\chi} = \frac{1}{3} \\ \langle(\cos\theta)^2\rangle_\Omega &= \frac{\int_0^\pi\int_0^{2\pi}\int_0^{2\pi}(\cos\theta)^2\sin\theta d\theta d\phi d\chi}{\int_0^\pi\int_0^{2\pi}\int_0^{2\pi}\sin\theta d\theta d\phi d\chi} = \frac{1}{3}. \end{aligned} \tag{D.7}$$

From Eq. (D.6) we can see the absorption coefficient is given by the auto-correlation function of molecular dipole moment. Eq. (D.6) can be easily solved by wave packet propagation. On the other hand Eq. (D.6) can also be written as a time independent form according to Eq. (D.3)

$$\alpha(\omega) = \frac{4\pi n\omega}{3c\varepsilon_0} \sum_{fi\gamma'} P(E_i)|\langle f|\mu_{\gamma'}|i\rangle|^2 \delta(\hbar\omega - E_{fi}). \tag{D.8}$$

The spectrum of an ideal noninteracting molecular system is just a sum of a series of delta functions. For zero temperature only the ground state has probability one and all the other states are unpopulated which will greatly reduce the calculation efforts.

Concerning the real experiment the resolution is not high enough to distinguish the nearly continuous rotational excitations. Therefore around each vibrational absorption bands there will be many symmetry allowed rotational excitations which simply broaden this vibrational band. From the numerical calculation point of view, it is also not possible to directly calculate the Fourier transformation of the dipole-dipole autocorrelation function since it is non-decaying. Therefore we artificially add certain lifetime Γ to each eigenenergy to make the dipole-dipole autocorrelation function decay exponentially. The numerical equation for the IR absorption spectrum is

$$\alpha(\omega) = \frac{2n\omega}{3c\varepsilon_0\hbar} \int_{-\infty}^{\infty} \sum_{m\gamma} P(E_m) e^{iE_m t/\hbar - \Gamma t} \langle m|\mu_\gamma e^{-iH_s t} \mu_\gamma |m\rangle dt. \tag{D.9}$$

The difference between Eq. (D.6) and the above equation is that the spectrum calculated by the latter is broadened as a sum of a series of Lorentz type peaks. However, they do give the same result for the position of each excitation which is the most important quantity for the spectrum.

List of Figures

List of Tables

Bibliography

[1] P. Schuster, G. Zundel, and C. Sandorfy (eds.). *The Hydrogen Bond* (Elsevier, Amsterdam, 1976).

[2] T. Bountis (ed.). *Proton Transfer in Hydrogen-Bonded Systems*, New York (1992). Plenum Press.

[3] D. A. Smith (ed.). *Modeling the Hydrogen Bond*. ACS Symposium Series (ACS, Washigton, 1994).

[4] G. A. Jeffrey. *An Introduction to Hydrogen Bonding* (Oxford University Press, New York, 1997).

[5] S. Scheiner. *Hydrogen Bonding* (Oxford University Press, New York, 1997).

[6] H.-H. Limbach and J. Manz (eds.). Ber. Bunsenges. Phys. Chem. **102**, 289 (1998).

[7] A. Kohen and H.-H. Limbach (eds.). *Isotope Effects in Chemistry and Biology* (Taylor and Francis, Boca Raton, 2005).

[8] J. T. Hynes, J. P. Klinman, H.-H. Limbach, and R. L. Schowen (eds.). *Hydrogen-Transfer Reactions* (Wiley-VCH, Weinheim, 2007).

[9] W. M. Latimer and W. H. Rodebush. J. Am. Chem. Soc. **42**, 1419 (1920).

[10] M. L. Huggins. Angew. Chem. Int. Ed. **10**, 147 (1971).

[11] L. Pauling. J. Am. Chem. Soc. **53**, 1367 (1931).

[12] L. Pauling. *The Nature of the Chemical Bond* (Cornell University Press, Ithaka, 1939).

[13] R. M. Badger and S. H. Bauer. J. Chem. Phys. **5**, 839 (1936).

[14] M. Shibl. *Mechanisms of Double Proton Tautomerization & Quantum Control of Tautomerism in Enantiomers by Light* (PhD thesis Freie Universität Berlin, 2006).

[15] R. Rousseau, V. Kleinschmidt, U. Schmitt, D. Marx Phys. Chem. Chem. Phys. **6**, 1848 (2004).

[16] K. R. Asmis, D. M. Neumark, and J. M. Bowman. In *Hydrogen-Transfer Reactions* (edited by J. T. Hynes, J. P. Klinman, H.-H. Limbach, and R. L. Schowen) (Wiley-VCH, Weinheim, 2007), vol. 1, p. 53.

[17] J. R. Roscioli, L. R. McCunn, and M. A. Johnson. Science **316**, 249 (2007).

[18] A. Chandra, M. E. Tuckerman, and D. Marx. Phys. Rev. Lett. **99**, 145901 (2007).

[19] M. E. Tuckerman, A. Chandra, and D. Marx. Acc. Chem. Res. **39**, 151 (2006).

[20] M. E. Tuckerman, D. Marx, and M. Parinello. Nature **417**, 925 (2002).

[21] S. Mukamel. *Principles of Nonlinear Optical Spectroscopy* (Oxford, New York, 1995).

[22] M. D. Fayer (ed.). *Ultrafast Infrared and Raman Spectroscopy* (Marcel Dekker, New York, 2001).

[23] T. Elsaesser. In *Femtosecond Chemistry* (edited by J. Manz and L. Wöste) (Verlag Chemie, Weinheim, 1994), vol. 2, p. 563.

[24] A. Douhal, F. Lahmani, and A. H. Zewail. Chem. Phys. **207**, 477 (1996).

[25] E. T. J. Nibbering and T. Elsaesser. Chem. Rev. **104**, 1887 (2004).

[26] N. Došlić, Y. Fujimura, L. González, K. Hoki, D. Kröner, O. Kühn, J. Manz, and Y. Ohtsuki. In *Femtochemistry* (edited by G. S. F. C. DeSchryver, S. DeFeyter) (VCH-Wiley, Berlin, 2001), p. 189.

[27] M. L. Huggins. J. Phys. Chem. **40**, 723 (1936).

[28] K. R. Asmis, N. L. Pivonka, G. Santambrogio, M. Brümmer, C. Kaposta, D. M. Neumark, and L. Wöste. Science **299**, 1375 (2003).

[29] H. Meyer and G. A. Worth. Theor. Chem. Acc. **109**, 251 (2003).

[30] G. Voth. Acc. Chem. Res. **39**, 143 (2006).

[31] D. Marx. ChemPhysChem **7**, 1848 (2006).

[32] M. Tuckerman, K. Laasonen, M. Sprik, and M. Parrinello. J. Chem. Phys. **103**, 150 (1995).

[33] N. I. Hammer, E. G. Diken, J. R. Roscioli, M. A. Johnson, E. M. Myshakin, K. D. Jordan, A. B. McCoy, X. Huang, J. M. Bowman, and S. Carter. J. Chem. Phys. **122**, 244301 (2005).

[34] K. Giese, M. Petković, H. Naundorf, and O. Kühn. Phys. Rep. **430**, 211 (2006).

[35] M. V. Vener, O. Kühn, and J. Sauer. J. Chem. Phys. **114**, 240 (2001).

[36] J. Sauer and J. Döbler. ChemPhysChem **6**, 1706 (2005).

[37] O. Vendrell, F. Gatti, and H.-D. Meyer. Angew. Chem. Int. Ed. **46**, 6918 (2007).

[38] O. Vendrell, F. Gatti, D. Lauvergnat, and H.-D. Meyer. J. Chem. Phys. **127**, 184302 (2007).

[39] O. Vendrell, F. Gatti, and H.-D. Meyer. J. Chem. Phys. **127**, 184303 (2007).

[40] E. A. Price, W. H. Robertson, E. G. Diken, G. H. Weddle, and M. A. Johnson. Chem. Phys. Lett. **366**, 412 (2002).

[41] E. A. Price, W. H. Robertson, E. G. Diken, G. H. Weddle, and M. A. Johnson. Chem. Phys. Lett. **299**, 1367 (2003).

[42] X. Huang, B. J. Braams, S. Carter, and J. M. Bowman. J. Am. Chem. Soc. **126**, 5042 (2004).

[43] E. Diken, J. Headrick, J. Roscioli, J. Bopp, M. Johnson, A. McCoy, X. Huang, S. Carter, and J. M. Bowman. J. Phys. Chem. A **109**, 571 (2005).

[44] E. Diken, J. Headrick, J. Roscioli, J. Bopp, M. Johnson, and A. McCoy. J. Phys. Chem. A **109**, 1487 (2005).

[45] A. B. McCoy, X. Huang, S. Carter, and J. M. Bowman. J. Chem. Phys. **123**, 064317 (2005).

[46] H.-G. Yu. J. Chem. Phys. **125**, 204306 (2006).

[47] S. Khademi, J. O. III, J. Remis, Y. Robles-Colmenars, L. J. W. Miercke, and R. M. Stroud. Science **305**, 1587 (2004).

[48] C. Tanner, C. Manca, and S. Leutwyler. Science **302**, 1736 (2003).

[49] J. M. Price, M. W. Crofton, and Y. T. Lee. J. Phys. Chem. **95**, 2182 (1991).

[50] M. Ichihashi, J. Yamabe, K. Murai, S. Nonose, K. Hirao, and T. Kondow. J. Phys. Chem. **100**, 10050 (1996).

[51] K. Tono, K. Bito, H. Kondoh, T. Ohta, and K. Tsukiyama. J. Chem. Phys. **125**, 224305 (2006).

[52] K. Tono, K. Fukazawa, M. Tada, N. Fukushima, and K. Tsukiyama. Chem. Phys. Lett. **442**, 206 (2007).

[53] M. Meuwly and M. Karplus. J. Chem. Phys. **116**, 2572 (2002).

[54] V. Zoete and M. Meuwly. J. Chem. Phys. **120**, 7085 (2004).

[55] A. Fouqueau and M. Meuwly. J. Chem. Phys. **123**, 244308 (2005).

[56] H.-H. Limbach, G. S. Denisov, and N. S. Golubev. In *Isotope Effects in Chemistry and Biology* (edited by A. Kohen and H.-H. Limbach) (Taylor and Francis, Boca Raton, 2005).

[57] H.-H. Limbach. In *Hydrogen-Transfer Reactions* (edited by J. T. Hynes, J. P. Klinman, H.-H. Limbach, and R. L. Schowen) (Wiley-VCH, Weinheim, 2007), vol. 1, p. 135.

[58] S. Glasstone, K. J. Laidler, and H. Eyring (eds.). *Theory of Rate Processes* (McGraw-Hill, New York, 1941).

[59] W. Miller. J. Chem. Phys. **61**, 1823 (1974).

[60] W. Miller and S. D. S. abd J. W. Tromp. J. Chem. Phys. **79**, 4889 (1983).

[61] M. Born and R. Oppenheimer. Ann. Phys. **84**, 457 (1927).

[62] M. J. Frisch, G. W. Trucks, H. B. Schlegel, G. E. Scuseria, M. A. Robb, J. R. Cheeseman, J. A. Montgomery, Jr., T. Vreven, K. N. Kudin, J. C. Burant, J. M. Millam, S. S. Iyengar, J. Tomasi, V. Barone, B. Mennucci, M. Cossi, G. Scalmani, N. Rega, G. A. Petersson, H. Nakatsuji, M. Hada, M. Ehara, K. Toyota, R. Fukuda, J. Hasegawa, M. Ishida, T. Nakajima, Y. Honda, O. Kitao, H. Nakai, M. Klene, X. Li, J. E. Knox, H. P. Hratchian, J. B. Cross, V. Bakken, C. Adamo, J. Jaramillo, R. Gomperts, R. E. Stratmann, O. Yazyev, A. J. Austin, R. Cammi, C. Pomelli, J. W. Ochterski, P. Y. Ayala, K. Morokuma, G. A. Voth, P. Salvador, J. J. Dannenberg, V. G. Zakrzewski, S. Dapprich, A. D. Daniels, M. C. Strain, O. Farkas, D. K. Malick, A. D. Rabuck, K. Raghavachari, J. B. Foresman, J. V. Ortiz, Q. Cui,

A. G. Baboul, S. Clifford, J. Cioslowski, B. B. Stefanov, G. Liu, A. Liashenko, P. Piskorz, I. Komaromi, R. L. Martin, D. J. Fox, T. Keith, M. A. Al-Laham, C. Y. Peng, A. Nanayakkara, M. Challacombe, P. M. W. Gill, B. Johnson, W. Chen, M. W. Wong, C. Gonzalez, and J. A. Pople. *Gaussian 03, Revision B.04*. Gaussian Inc., Wallingford, CT (2004).

[63] W. H. Miller, N. C. Handy, and J. E. Adams. J. Chem. Phys. **72**, 99 (1980).

[64] T. Carrington and W. H. Miller. J. Chem. Phys. **81**, 3942 (1984).

[65] N. Shida, P. F. Barbara, and J. E. Almlöf. J. Chem. Phys. **91**, 4061 (1989).

[66] D. P. Tew, N. C. Handy, and S. Carter. Phys. Chem. Chem. Phys. **3**, 1958 (2001).

[67] K. Giese and O. Kühn. J. Chem. Phys. **123**, 54315 (2005).

[68] B. Podolsky. Phys. Rev. **32**, 812 (1928).

[69] R. Mecke. Z. Phys. **101**, 405 (1936).

[70] P. R. Bunker. *Molecular Symmetry and Spectroscopy* (Academic, New York, 1979).

[71] J. H. Frederick and C. Woywod. J. Chem. Phys. **111**, 7255 (1999).

[72] C. Eckart. Phys. Rev. **47**, 552 (1935).

[73] E. B. Wilson, J. C. Decius, and P. C. Cross. *Molecular Vibrations* (Dover, New York, 1955).

[74] J. K. G. Watson. Mol. Phys. **15**, 479 (1968).

[75] J. K. G. Watson. Mol. Phys. **29**, 465 (1970).

[76] J. M. Bowman, S. Carter, and X.-C. Huang. Int. Rev. Phys. Chem. **22**, 533 (2003).

[77] M. J. Bramley, W. H. Green, Jr., and N. C. Handy. Mol. Phys. **73**, 1183 (1991).

[78] F. Gatti, C. Munoz, and C. Iung. J. Chem. Phys. **114**, 8275 (2001).

[79] F. Gatti and C. Iung. J. Theo. Comp. Chem. **2**, 507 (2003).

[80] C. Iung and F. Gatti. Int. J. Quan. Chem. **106**, 130 (2006).

[81] O. Vendrell, F. Gatti, and H. D. Meyer. Angew. Chem. Int. Ed. **46**, 6918 (2007).

[82] A. Nauts and X. Chapuisat. Chem. Phys. Lett. **136**, 164 (1987).

[83] F. Gatti, Y. Justum, M. Menou, A. Nauts, and X. Chapusiat. J. Mol. Spectr. **181**, 403 (1997).

[84] D. Luckhaus. J. Chem. Phys. **113**, 1329 (2000).

[85] D. Lauvergnat and A. Nauts. J. Chem. Phys. **116**, 8560 (2002).

[86] Y. Yang and O. Kühn. Mol. Phys. **106**, 2445 (2008).

[87] W. S. l'Yi. Phys. Rev. A **53**, 1251 (1996).

[88] Paul A. Tipler and Gene Mosca. *Physics For Scientists And Engineers: Extended Version* (W.h. Freeman & Company, 2003).

[89] S. Carter, S. J. Culik, and J. M. Bowman. J. Chem. Phys. **107**, 10458 (1997).

[90] M. H. Beck, A. Jäckle, G. A. Worth, and H.-D. Meyer. Phys. Rep. **324**, 1 (2000).

[91] G. Worth, M. Beck, A. Jäckle, and H.-D. Meyer. The mctdh package, version 8.4. University of Heidelberg, Heidelberg (2007).

[92] X. Huang, B. J. Braams, and J. M. Bowman. J. Chem. Phys. **122**, 044308 (2005).

[93] A. Jäckle and H.-D. Meyer. J. Chem. Phys. **104**, 7974 (1996).

[94] R. Kosloff and H. Tal-Ezer. Chem. Phys Lett. **127**, 223 (1986).

[95] H.-D. Meyer, F. L. Quere, C. Leonard, and F. Gatti. Chem. Phys. **329**, 179 (2006).

[96] K. R. Asmis, Y. Yang, G. Santambrogio, M. Brümmer, J. R. Roscioli, L. R. McCunn, M. A. Johnson, and O. Kühn. Angew. Chem. Int. Ed. **46**, 8691 (2007).

[97] Y. Yang, O. Kühn, G. Santambrogio, D. Goebbert, and K. R. Asmis. J. Chem. Phys. **129**, 224302 (2008).

[98] T. Asada, H. Haraguchi, and K. Kitaura. J. Phys. Chem. A **105**, 7423 (2001).

[99] H. Ishibashi, A. Hayashi, M. Shiga, and M. Tachikawa. ChemPhysChem **9(3)**, 383 (2008).

[100] Y. Yang and O. Kühn. Z. Phys. Chem. **222**, 1375 (2008).

[101] T. Steiner and W. Saenger. J. Am. Chem. Soc. **114**, 7123 (1992).

[102] H.-H. Limbach, M. Pietrzak, H. Benedict, P. M. Tolstoy, N. S. Golubev, and G. S. Denisov. J. Mol. Struct. **706**, 115 (2004).

[103] H.-H. Limbach, M. Pietrzak, S. Sharif, P. M. Tolstoy, I. G. Shenderovich, S. N. Smirnov, N. S. Golubev, and G. S. Denisov. Chem. Eur. J. **10**, 5195 (2004).

[104] C. D. Carver (ed.). *The Coblentz Society Desk Book of Infrared Spectra, Second Edition* (The Coblenz Society, Kirkwood, MO, 1982).

[105] D. A. Weil and D. A. Dixon. J. Am. Chem. Soc. **107**, 6859 (1985).

[106] J. W. Larson and T. B. McMahon. J. Am. Chem. Soc. **110**, 1087 (1988).

[107] R. A. More O'Ferral and A. J. Kresge. J. Chem. Soc. Perkin Trans. 2 **2**, 1840 (1980).

[108] Y. Chiang, A. J. Kresge, and R. A. More O'Ferral. J. Chem. Soc. Perkin Trans. 2 p. 1832 (1980).

[109] M. M. Kreevoy, T. Liang, and K. Chong. J. Am. Chem. Soc. **99**, 5207 (1977).

[110] M. M. Kreevoy and T. Liang. J. Am. Chem. Soc. **102**, 3315 (1980).

[111] S. Scheiner and M. Cuma. J. Am. Chem. Soc. **118**, 1511 (1996).

[112] M. F. Shibl, M. Pietrzak, H.-H. Limbach, and O. Kühn. ChemPhysChem **8**, 315 (2007).

[113] M. Tachikawa and M. Shiga. J. Am. Chem. Soc. **127**, 11908 (2005).

[114] R.A. Marcus and N. Sutin. Biochim. Biophys. Acta. **811**, 265 (1985).

[115] J. M. L. del Amo, U. Langer, V. Torres, G. Buntkowsky, H.-M. Vieth, M. Pérez-Torralba, D. Sanz, R. M. Claramunt, J. Elguero, and H.-H. Limbach. J. Am. Chem. Soc. **130**, 8620 (2008).

[116] W. H. Miller, B. A. Ruf, and Y.-T. Chang. J. Chem. Phys. **89**, 6298 (1988).

[117] M. Topaler and N. Makri. Chem. Phys. Lett. **210**, 285 (1993).

[118] K. M. Forsythe and N. Makri. J. Chem. Phys. **108**, 6819 (1998).

[119] R. Feynman and A. Hibbs. *Quantum Mechanics and Path Integrals* (McGrawHill, New York, 1965).

[120] V. May and O. Kühn. *Charge and Energy Transfer Dynamics in Molecular Systems, 2nd Revised and Enlarged Edition* (Wiley–VCH, Weinheim, 2004).

[121] C. Iung, F. Gatti, A. Viel, and X. Chapusiat. Phys. Chem. Chem. Phys. **1**, 3377 (1999).

Acknowledgment

First of all, I would like to thank Prof. Dr. Oliver Kühn for introducing this interesting topic to me. During the last three years he has provided me numerous instructions, inspiring discussions, and continuous support without which this work would not have been possible. It is beyond language's capability to express my appreciation.

I am very grateful to Prof. Dr. Jörn Manz for giving me the opportunity to work in his group, for his continuous support and interest in my work, as well as for his kind care in my life. Moreover I am grateful for the friendly working atmosphere with AG Manz. And I would like to extend special thanks to Alexander Borowski, Gireesh Krishnan, Mohamed Shibl, Verónica Leyva Novoa, and Abdel-Latif Mahmoud, for being such kind office mates.

I am also grateful to our experimental partners, Dr. Knut Asmis and Gabriele Santambrogio, who were always helpful and willing to answer questions regarding the laser experiments. I am also grateful to Prof. Dr. Hans-Heinrich Limbach for many stimulating discussions.

Without a working computer system this work would not have been possible. I thank Dr. Holger Naundorf for immediate solutions of computer problems. I also thank the Deutsche Forschungsgemeinschaft, Graduiertenkolleg 788, "Hydrogen bonding and hydrogen transfer", and Dr. Werner Gans, for the financial support.

Finally, this thesis is dedicated to my dear parents and at this very moment I just want to tell them how much they have meant to me.

Publications (PhD work)

(I) **Gas-Phase Infrared Spectroscopy and Multidimensional Quantum Calculations of the Protonated Ammonia Dimer $N_2H_7^+$**
K. R. Asmis, Y. Yang, G. Santambrogio, M. Brümmer, J. R. Roscioli, L. R. McCunn, M. A. Johnson, O. Kühn
Angew. Chem. Int. Ed. 46, pp. 8691-8694 (2007)

(II) **A Full-Dimensional Quantum Dynamical Study of the Vibrational Ground State of $H_3O_2^-$ and its Isotopomers**
Y. Yang and O. Kühn
Z. Phys. Chem. 222, pp. 1375-1387 (2008)
(Festschrift for Prof. H.-H. Limbach)

(III) **A Concise Method for Kinetic Energy Quantization**
Y. Yang and O. Kühn
Mol. Phys., 106, pp. 2445-2457 (2008)

(IV) **Vibrational Signatures of Hydrogen Bonding in the Protonated Ammonia Clusters $NH_4^+(NH_3)_{1-4}$**
Y. Yang, O. Kühn, G. Santambrogio, D.J. Goebbert, K. R. Asmis
J. Chem. Phys., 129, pp. 224302 (2008)

(*) **A New Method for Rate Constant Calculations and Application to Condensed Phase Hydrogen Transfer in 6-Aminofulvene-1-aldimine**
Y. Yang, O. Kühn
(in preparation)

(*) **Isotope Effects of Protonated Ammonia Dimer $N_2H_7^+$: Geometry and Infrared Spectroscopy**
Y. Yang and O. Kühn
(in preparation)

Erklärung

Hiermit versichere ich, dass ich die vorliegende Arbeit mit den angegebenen Hilfsmitteln selbständig angefertigt habe.

Berlin, 2008